Inorganic porous hollow fiber membranes

with tunable small radial dimensions

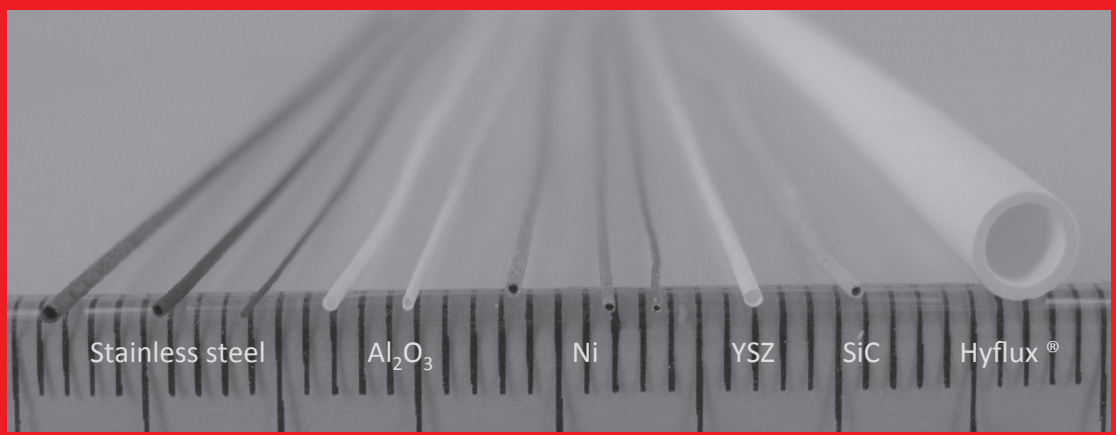

M.W.J. Luiten-Olieman

Inorganic porous hollow fiber membranes

with tunable small radial dimensions

The research presented in this thesis was financially supported by Stichting voor de Technische Wetenschappen (STW, Project 07349).

Promotion committee

Prof. Dr. Ir. A. Nijmeijer (promotor)	University of Twente
Dr. Ir. N.E. Benes (assistant promotor)	University of Twente
Prof. Dr.-Ing. M. Wessling	University of Twente
Prof. Dr. Ir. R.G.H. Lammertink	University of Twente
Prof. I. Vankelecom	Katholieke Universiteit Leuven
Ir. P.T. Alderliesten	Energieonderzoek Centrum Nederland
Prof. Dr. G. Mul	University of Twente
Prof. Dr. Ing. D.H.A. Blank	University of Twente

Inorganic porous hollow fiber membranes with tunable small radial dimensions

ISBN: 978-90-365-3327-0
DOI: 10.3990/1.9789036533270
URL: http://dx.doi.org/10.3990/1.9789036533270

Pictures cover: S.M. Dutczak.

Printed by: Gildeprint Drukkerijen, The Netherlands.

INORGANIC POROUS HOLLOW FIBER MEMBRANES

WITH TUNABLE SMALL RADIAL DIMENSIONS

DISSERTATION

to obtain
the degree of doctor at the University of Twente,
on the authority of the rector magnificus,
Prof. Dr. H. Brinksma,
on account of the decision of the graduation committee,
to be publicly defended
on Friday the 9th of March 2012, at 16:45

by

Maria Wilhelmina Johanna Luiten-Olieman

born on September 10th , 1970
in Hagestein.

This dissertation has been approved by:

Prof. Dr. Ir. A. Nijmeijer (promotor)

Dr. Ir. N.E. Benes (assistant promotor)

Contents

Chapter 1:
General introduction

1.1 Introduction

A membrane is a permselective barrier between two phases. It facilitates faster transport of specific species as compared to other species [1, 2]. A schematic presentation is depicted in Figure 1.1. Molecular transport through a membrane can occur via various mechanisms, such as surface diffusion, Knudsen diffusion, and capillary condensation.

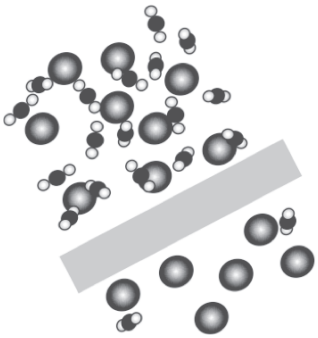

Figure 1.1: Schematic representation of a membrane

As compared to organic membranes, inorganic membranes have many unique advantages. In particular, their excellent chemical and thermal stability enables an extremely long life under harsh conditions, and allows more rigorous chemical and thermal cleaning to remove irreversible fouling. Inorganic membranes are widely used in various industrial fields, including water treatment, food and beverage, bio- and pharmaceutical industry, and chemical industry. A few examples of applications are the recovery and concentration of catalysts, amino acid production, concentration of polymer suspensions and metal hydroxide solutions, and oily emulsion water treatment in the automobile/steel/machinery industry.

The geometry of inorganic membranes is generally flat or tubular. These geometries have a moderate surface-to-volume ratio, when compared to hollow fiber membranes (Figure 1.2). Polymeric hollow fibers are made in large quantities via the dry-wet spinning process [1, 3-5] and are extensively used in various industrial, medical, and biomedical applications [2, 6].

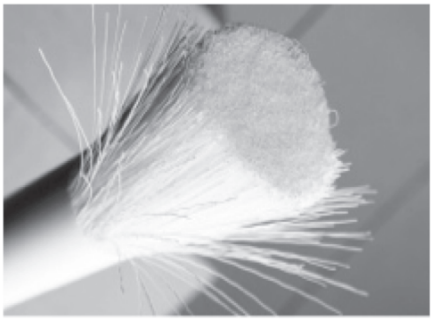

Figure 1.2: Example of commercial polymeric hollow fibers

Annually millions of membrane modules are produced for hemodialysis, each module containing approximately one kilometer length of hollow fiber that has a distinct separation performance and no defects [6]. These high-end modules typically cost $10-20 each, illustrating how well established the dry-wet spinning fabrication method is.

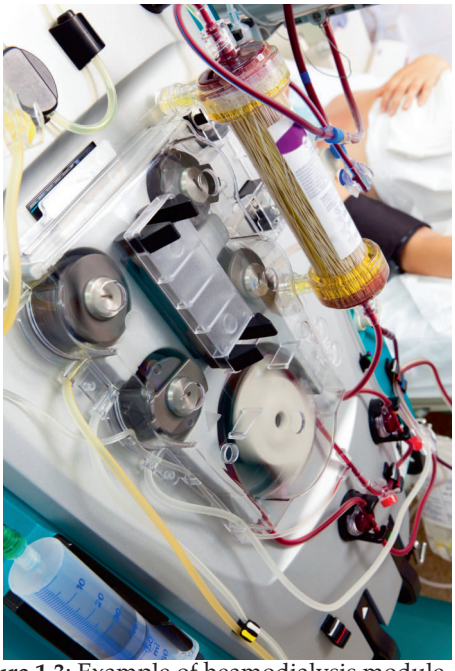

Figure 1.3: Example of heamodialysis module

Figure 1.4 displays a schematic representation of a dry-wet spinning set-up. The procedure is as follows. A mixture of a solvent and a polymer is extruded through an annular opening in a spinneret. Inside the annular opening a bore liquid (non-solvent) is introduced. After passing through an air gap, the extruded liquids are immersed in a coagulation bath.

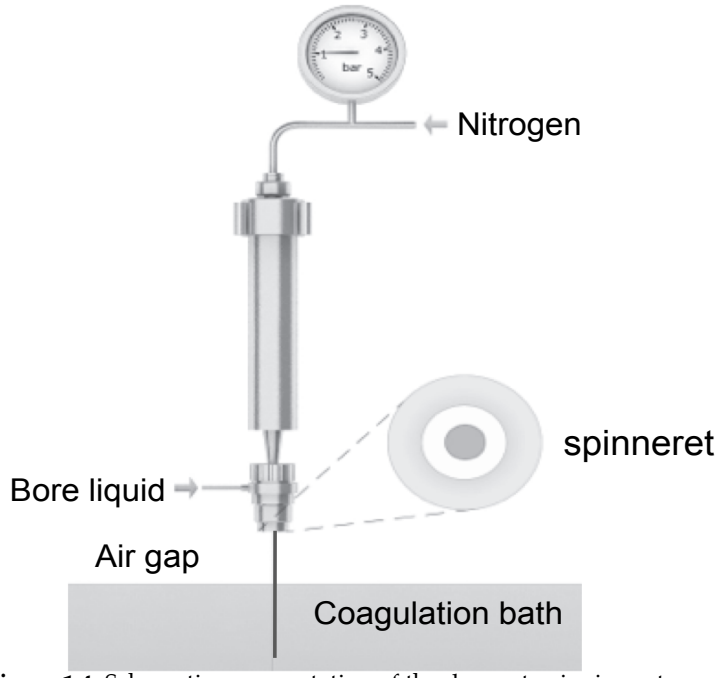

Figure 1.4: Schematic representation of the dry-wet spinning set-up

Evaporation of solvent, or exchange of solvent with a non-solvent, results in separation of the spinning mixture into a polymer lean phase and a solidified polymer rich phase: the hollow fiber membrane. The phase separation process can be rationalized using a simplified phase diagram (Figure 1.5). Initially, the spinning mixture has composition A. During the spinning process the composition changes to composition B, which corresponds to two separated phases. The precipitation path is in reality much more complicated, due to slow kinetic related to the viscosity of the polymer solutions, and the existence of thermodynamically metastable compositions [1, 2].

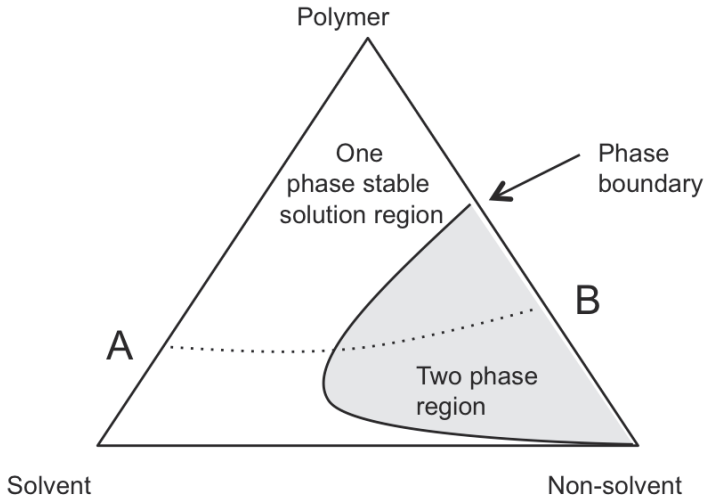

Figure 1.5: schematic representation of a phase diagram for ternary system: polymer/solvent/non-solvent

The morphology of a hollow fiber is strongly influenced by the spinning process and can exhibit macrovoids, finger-like voids, and sponge like structures. Figure 1.6 shows two examples of such structures.

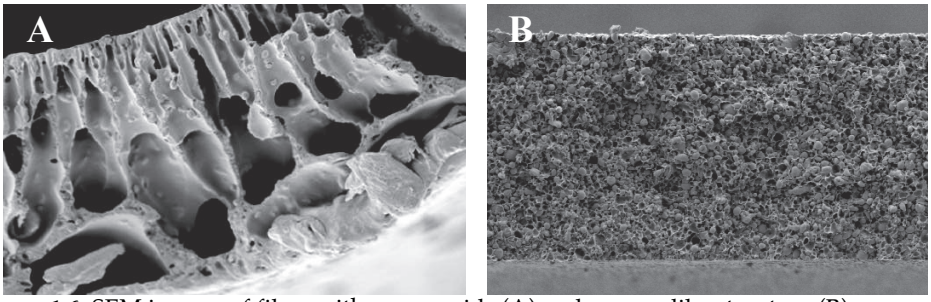

Figure 1.6: SEM images of films with macrovoids (A) and sponge like structure (B)

1.2 Inorganic hollow fibers

Inorganic hollow fiber membranes are also prepared via dry wet-spinning process. For this, inorganic particles are added to the spinning mixture. During phase separation the inorganic particles are entrapped in the solidified polymer rich phase. After the dry-wet spinning the fibers are given a thermal treatment to remove the polymer and to sinter the inorganic particles together. Currently, no commercial inorganic hollow fiber membranes are available.

In the scientific literature, many reports can be found of porous inorganic capillaries (> 0.5 mm outer diameter) prepared via dry-wet spinning with inorganic particle loaded polymers, followed by heat treatment. A selection of relevant publications is given in Table 1.1. Most commonly used materials for inorganic fibers include alumina, nickel, and yttrium stabilized zirconia. The table shows that most of the fibers are made of ceramics, rather than metals, and that the diameter of the fibers typically exceeds 1 mm. Only three publications present fibers with smaller diameters. To the best of our knowledge, preparation of porous inorganic hollow fibers with an outer diameter ≤ 0.5 mm has not been reported.

1.3 Scope of the thesis

The objectives of this thesis are twofold:

The first aim is the development of a *robust coating procedure* for thin supported films onto porous ceramic supports. This involves identification of, and dealing with, critical factors in the coating of porous ceramic supports. The aspiration is to develop methods for producing large surface area, high-quality supported thin films in a potentially commercially viable manner.

Second aim is the development of *preparation methodology for high quality inorganic porous membranes*, with large membrane surface area; inorganic counterparts of polymeric hollow fiber membranes. The methodology should allow tuning of the inorganic membrane properties, for instance to make them suitable as supporting structure for coating of highly selective (in)organic top layers.

Fiber material	Diameter [μm}	Main topic	Year	Reference
Al_2O_3	~1600	Effect particle size, spinning conditions and the sintering temperature on structure	1991	[9]
Al_2O_3	~850	Effect of PESf/Al_2O_3 ratio on pore size and porosity	2001	[10]
Al_2O_3	~1300	Effect particles size and size distribution on pore size and porosity	2003	[11]
Al_2O_3	~1400	Multilayer in single production step	2004	[12]
Al_2O_3	~1650	Morphology study	2009	[13]
Al_2O_3-Pd	~1700	A multifunctional Pd/alumina hollow fiber for propane dehydrogenation	2010	[14]
Al_2O_3 Al_2O_3-SiO_2 Al_2O_3-kaolin	> 1000	Comparison characteristics of the different materials	2011	[15]
Ni	~2500	Preparation and characterization of nickel hollow fiber	2008	[16]
Ni	~900	Characterization of porous and dense hollow fibers	2009	[17]
NiO-YSZ	~1500	Fabrication of Ni/YSZ hollow fibers as anode support	2008	[18]
LSCF	~1300	Permeation improvement by surface modification	2011	[19]
LSCF	> 1000	Honey-comb-structured perovskite hollow fiber membranes for oxygen gas permeation	2011	[20]
LFSC6428	> 1000	Morphology control by using different bore fluids	2011	[21]
BSCF	3500	Performance of sulfur-free, macrovoid-free BSCF capillaries	2011	[22]
YSZ	~1100	Characterization of asymmetric yttria stabilized zirconia hollow fiber membranes	2009	[23]
YSZ-Ni	> 1000	Ni layer on YZS hollow fiber for hollow fiber solid oxide fuel cells	2009	[24]
-	-	A short review of recent developments of inorganic hollow fiber membranes		[25]

Table 1.1: Overview of relevant publications related to the hollow fiber preparation of inorganic hollow fiber membranes

Thesis outline

In **Chapter 2** a robust method is presented for coating of a highly selective silica top layer on a tubular support. It combines reduced roughness of the membrane support surface with a straight forward coating procedure.

In **Chapter 3** the advantages of a ceramic support, high chemical stability and no swelling, are combined with the excellent separation properties of poly(dimethylsiloxane) coating. Membranes have been prepared via dip coating and characterized with liquid permeation and molecular weight cut-off measurements.

In **Chapter 4** porous stainless steel hollow fibers have been prepared via dry wet-spinning of a particle loaded spinning mixture. Stainless steel hollow fibers offer an improved mechanical strength combined with an optimised surface-to-volume ratio.

In **Chapter 5** porous stainless steel hollow fibers with small radial dimensions have been developed, down to an outer diameter of ~ 250 μm. Viscous deformation of the fibers occurs at temperatures around the glass transition temperature of the polymer resulting in substantial decrease in dimensions of the hollow fiber and in improved fiber morphology.

In **Chapter 6** a generic and versatile method is developed for the preparation of inorganic hollow fibers with small outer diameters. For four different materials a particle specific range is identified in which viscous flow is possible; below a minimal particle concentration it is not possible to sinter particles together and above a critical particle volume fraction viscous flow is hindered by a sharp increase in viscosity.

Chapter 7 summarizes the main conclusions of this thesis and reflects on future perspectives.

References

[1] M. Mulder, Basic Principles of Membrane Technology, first ed., Kluwer Academic Publishers, Dordrecht, 2000.

[2] R.W. Baker, Membrane technology and applications, second ed., McGraw-Hill, Chichester, 2004.

[3] S. McKelvey, A, D. Clausi, T., W.J. Koros, A guide to establishing hollow fiber macroscopic properties for membrane applications, Journal of Membrane Science, 124 (1997) 223-232.

[4] W.W.Y. Lau, M.D. Guiver, T. Matsuura, Phase separation in polysulfone/solvent/water and polyethersulfone/solvent/water systems, Journal of Membrane Science, 59 (1991) 219-227.

[5] H. Strathmann, The formation mechanism of phase inversion membranes, Desalination, 21 (1977) 14.

[6] I. Moch, Hollow-Fiber Membranes, Kirk-Othmer Encyclopedia of Chemical Technology, in: Kirk-Othmer Encyclopedia of Chemical Technology, Wiley, 2005.

[7] M.D. Jonas, B. Wayne, Hemodialysis, in: Mosby's Dictionary of Complementary and Alternative Medicine, Elsevier, 2005.

[8] B. Tay, L. Liu, N. Loh, S. Tor, Y. Murakoshi, R. Maeda, Surface roughness of microstructured component fabricated by μMIM, Materials Science and Engineering A, 396 (2005) 311-319.

[9] K.H. Lee, Y.M. Kim, Asymmetric hollow inorganic membranes, Key Eng. Mater., 61-62 (1991) 17-22.

[10] X. Tan, S. Liu, K. Li, Preparation and characterization of inorganic hollow fiber membranes, Journal of Membrane Science, 188 (2001) 87-95.

[11] S. Liu, K. Li, R. Hughes, Preparation of porous aluminium oxide (Al_2O_3) hollow fibre membranes by a combined phase-inversion and sintering method, Ceramics International, 29 (2003) 875-881.

[12] J. De Jong, N. Benes, G. Koops, M. Wessling, Towards single step production of multi-layer inorganic hollow fibers, Journal of Membrane Science, 239 (2004) 265-269.

[13] B. Kingsbury, K. Li, A morphological study of ceramic hollow fibre membranes, Journal of Membrane Science, 328 (2009) 134-140.

[14] E. Gbenedio, Z. Wu, I. Hatim, B.F.K. Kingsbury, K. Li, A multifunctional Pd/alumina hollow fibre membrane reactor for propane dehydrogenation, Catalysis Today, 156 (2010) 93-98.

[15] L.-F. Han, Z.-l. Xu, Y. Cao, Y.-M. Wei, H.-T. Xu, Preparation,

characterisation and permeation property of Al_2O_3, Al_2O_3-SiO_2 and Al_2O_3-kaloin hollow fiber membranes, Journal of Membranes Science, 372 (2011) 154-164.

[16] D.-W. Lee, S.-J. Park, C.-Y. Yu, S.-K. Ihm, K.-H. Lee, Novel synthesis of a porous stainless steel-supported Knudsen membrane with remarkably high permeability, Journal of Membrane Science, 302 (2007) 265-270.

[17] B. Meng, X. Tan, X. Meng, S. Qiao, S. Liu, Porous and dense Ni hollow fibre membranes, Journal of Alloys and Compounds, 470 (2009) 461-464.

[18] N. Yang, X. Tan, Z. Ma, A phase inversion/sintering process to fabricate nickel/yttria-stabilized zirconia hollow fibers as the anode support for micro-tubular solid oxide fuel cells, Journal of Power Sources, 183 (2008) 14-19.

[19] Z. Wang, H. Liu, X. Tan, Y. Jin, S. Liu, Improvement of the oxygen permeation through perovskite hollow fibre membranes by surface acid-modification, Journal of Membrane Science, 345 (2009) 65-73.

[20] N. Liu, X. Tan, B. Meng, S. Liu, Honeycomb-structured perovskite hollow fiber membranes with ultra-thin densified layer for oxygen separation, Separation and Purification Technology, 80 (2011) 396-401.

[21] X. Tan, N. Liu, B. Meng, S. Liu, Morphology control f the perovskite hollow fiber membrane for oxygen seperation using different bore fluids, Journal of Membrane Science, 378 (2011) 308-318.

[22] C. Buysse, A. Kovalevsky, F. Snijkers, A. Beukenhoudt, S. Mullens, J. Luyten, J. Kretzschmar, S. Lenaerts, Development, performance and stability of sulfur-free, macrovoid-free BSCF capillaries for high temperature oxygen separation from air, Journal of Membrane Science, 372 (2011) 239-248.

[23] W. Yin, B. Meng, X. Meng, X. Tan, Highly asymmetric yttria stabilized zirconia hollow fibre membranes, Journal of Alloys and Compounds, 476 (2009) 566-570.

[24] F. Dal Grande, A. Thursfield, K. Kanawka, N. Droushiotis, U. Doraswami, Microstructure and performance of novel Ni anode for hollow fibre solid oxide fuel cells, Solid State Ionics, 180 (2009) 800-804.

[25] X. Tan, K. Li, Inorganic hollow fibre membranes in catalytic processing, Current Opinion in Chemical Engineering, 1 (2011) 69–76.

Chapter 2:

Robust method for micro-porous silica membrane fabrication

THIS CHAPTER HAS BEEN PUBLISHED:

M.W.J.Luiten, Nieck E. Benes, Cindy Huiskes, Henk Kruidhof, Arian Nijmeijer, Robust method for micro-porous silica membrane fabrication, Journal of Membrane Science, 348 (2010) 1-5.

Abstract

High performance large surface area micro-porous silica membranes have been prepared using a robust method that combines reduced roughness of the membrane support surface with a straightforward coating procedure. The method allows for reproducible production of membranes with a flat plate or tubular geometry. Tubular membranes with a length suitable for commercial application (55 cm) show performance comparable, in terms of flux and permselectivity, to that of low surface area flat plate membranes and shorter tubes (10 cm). At 250 °C and pressure difference of 2 bar the hydrogen permeance of the 55 cm membranes is in the range $0.5 – 1 \times 10^{-6}$ mol $m^{-2}s^{-1}Pa^{-1}$, and the permselectivity of hydrogen with respect to methane is in the range 350 - 400. Permeation measurements below 400 °C over a period of more than 2100 h showed no significant changes in permeance or permselectivity.

2.1 Introduction

Micro-porous silica membranes have been studied for decennia. These membranes can be highly selective for small gases at higher temperatures and are potentially interesting for applications involving selective removal of hydrogen. Applications with commercial prospective include the water-gas shift reaction and equilibrium-restricted processes such as dehydrogenation [1]. For commercial application silica membranes with tubular or hollow fiber geometry seem most promising. An overview of relevant publications related to silica membranes with such geometries is listed in Table 2.1. The table shows that chemical vapor deposition (CVD) and sol-gel chemistry combined with a coating technique prevail for silica membrane fabrication. Membranes prepared via CVD display high permselectivity for hydrogen over nitrogen or methane, combined with low hydrogen permeance (1 - 10 × 10^{-8} mol m^{-2} s^{-2} Pa^{-1}). The CVD method has only been reported for limited membrane surface area, i.e., tubes with maximum length of 3 - 10 cm. In contrast, sol-gel derived membranes with larger surface area have been reported, i.e., tubes with a length up to 100 cm. Sol-gel chemistry is also an inherently versatile method for the production of metal oxide materials containing pores of molecular dimensions, via hydrolysis and subsequent polycondensation of precursor molecules. The interested reader is referred to for instance the book of Brinker [1, 2]. As compared to the CVD method the hydrogen permeance of sol-gel derived membranes is higher (1 - 10 × 10^{-7} mol m^{-2} s^{-1} Pa^{-1}), but the permselectivity for hydrogen over gases with higher kinetic diameter generally lower. The superior hydrogen flux of sol-gel derived silica membranes results from the presence of a very thin (generally <100 nm) distinct selective silica layer produced during the coating step. Although this thin layer allows for a low resistance to mass transport, the selectivity it provides is very susceptible to defects introduced during fabrication, for instance via contaminants such as dust particles. Clean-room facilities can be used to minimize contamination, however, the high costs involved form a major hurdle for economically viable fabrication of large membrane surface area.

Fabrication method	Times	Membrane Length (cm)	Gas components (A/B)	Permeance P_A (mol m^{-2} s^{-1} Pa^{-1})	Permselectivity	Measurement Temperature (°C)	Institute
CVD	1	10	H_2/N_2	$3{,}0 \times 10^{-7}$	1000	600	Kyushu University [3]
CVD	1	3	H_2/N_2	$9{,}0 \times 10^{-7}$	50	600	Korea Inst. of Energy Research [4]
CVD	1	5	H_2/N_2	$4{,}9 \times 10^{-8}$	2900	600	University of Tokyo [5]
CVD	1	4	H_2/CH_4	$5{,}0 \times 10^{-7}$	5900	600	Virginia University [6]
Wet cloth	Several	9	H_2/N_2		25-500	500	Hiroshima University [7]
Wet cloth	Several	25	H_2/CH_4	$1{,}3 \times 10^{-6}$	150	300	Hiroshima University [8]
Dip coating	Several	1,5	H_2/N_2	$2{,}1 \times 10^{-7}$	100	400	Kyushu University [9]
Dip coating	4	17	He/N_2	$2{,}2 \times 10^{-6}$	100-1000	200	Eindhoven University of Technology [10]
Dip coating	?	40-50	H_2/N_2	$2{,}0 \times 10^{-5}$	102	600	Noritake Company [11]
Dip coating	?	100	H_2/CH_4	$1{,}6 \times 10^{-6}$	28	<600	Nat.Tech. University of Athens [12]
Dip coating	2	5,5	H_2/N_2		320	80	University of new México [13]
Dip coating	Several	9	H_2/N_2	9.1×10^{-8}	190	500	Hiroshima University [14]

Table 2.1: An overview of relevant publications related to state-of-the-art silica membranes with tubular or hollow fiber geometry

Figure 2.1 shows a schematic representation of the coating set-up. Due to the principle of communicating vessels the height of the liquid in the membrane module is directly related to the vertical position of the feed vessel. By moving the feed vessel with a controlled speed in vertical direction, coating is performed such that the membrane tube is first filled and subsequently emptied. After this procedure a thin film of the coating solution remains on the inside of the tube. To reduce the probability of contamination, coating is performed in a system that is completely closed from the surroundings, under nitrogen. This procedure avoids the requirement of clean room facilities.

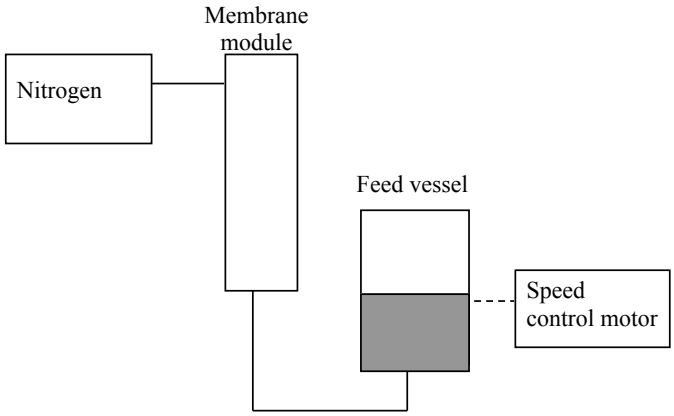

Figure 2.1: Schematic diagram of the coating set-up

The intermediate γ-alumina layer is doped with lanthanum to prevent pore growth as a result of the phase transformation to α-alumina [15]. To prevent delamination mono aluminum phosphate (MAP) is used as a ceramic bonding between the α-alumina support and γ-alumina intermediate layer [16]. Membranes with different dimensions have been prepared and their single gas permeation performance has been compared with that of state-of-the-art silica membranes reported in literature.

2.2 Experimental

2.2.1 Materials

Tubes of α-alumina (length 55 cm and 10 cm, internal diameter 0.7 cm) with improved surface morphology were purchased from Pervatech (Netherlands). Mono aluminum phosphate (MAP, $Al(H_2PO_4)_3$) (Alfa Aesar, 50% wt solution) was diluted 10 times with water. Lanthanum nitrate hexahydrate, tetraethyl orthosilicate (TEOS), and aluminum tri-sec-butylate (AlTSB) were purchased from Merck and stored in a nitrogen glove box to prevent reactions with water. Poly vinyl alcohol (PVA) (86.7-88.7 mol% hydrolysis, M_w ~67,000) was purchased from Aldrich. The chemicals were not treated prior to use, but used as received.

2.2.2 Sol synthesis

Boehmite sols (γ-AlOOH) were synthesized using AlTSB as precursor [17]. For membranes with enhanced (hydro)thermal stability the boehmite was doped with 6 % lanthanum [15], by thoroughly mixing the appropriate amounts of a lanthanum nitrate solution and boehmite sol. Coating solutions were obtained by mixing 30 ml boehmite sol with 20 ml PVA solution (30 g PVA/L in 0.05 M HNO_3).

Polymeric silica sols were prepared by acid-catalyzed hydrolysis and condensation of TEOS, as described in detail by De Vos and Verweij [18].

2.2.3 Coating procedure

A glass seal was applied to the tubular supports. The resulting tubes were coated by using a communicating vessel system, followed by calcining after each coating step, which is described in the next paragraph. All steps were carried out under clean-room conditions. Figure 2.2 schematically depicts the membrane fabrication method.

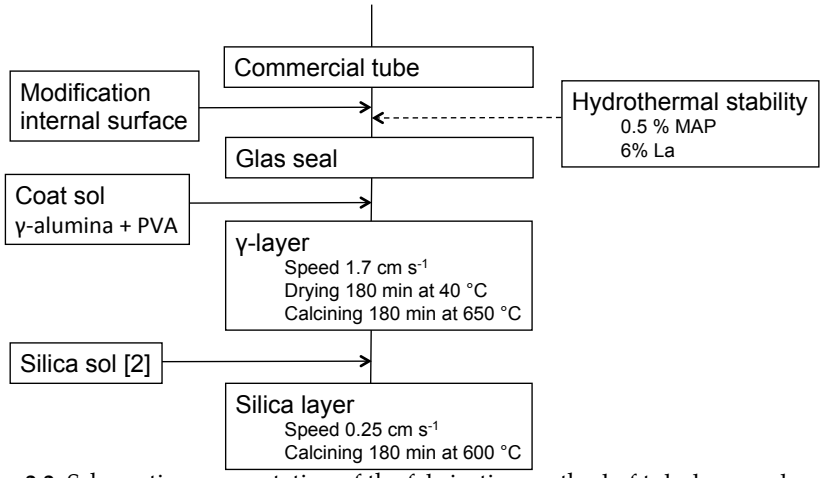

Figure 2.2: Schematic representation of the fabrication method of tubular membranes

The tubes were brought in contact with the boehmite coating solution for 3 min (filling / emptying at 1.7 cm s^{-1}). The coating was repeated once, with a shorter contact time (30 s). The resulting tubes were brought in contact with the silica coating solution for 10 s (filling at 2.5 cm s^{-1}, emptying at 0.25 cm s^{-1}). The coating procedure was repeated once.

For membranes with intended enhanced (hydro)thermal stability the same coating procedure was used, preceded by an initial coating step with MAP-solution for 10 s (filling / emptying at 1.7 cm s^{-1}) and lanthanum doping of the boehmite sol.

For comparison, flat supports were coated with a rotating dip-coater (rotating speed = 1.4 cm s^{-1} for all coating solutions) with the same coating solutions.

2.2.4 Calcining procedures

The MAP treated alumina tubes were dried at 40 ºC and 60% relative humidity for 3 h, followed by firing at 300 °C in air for 1 h (heating / cooling rate 1 ºC min^{-1}).

At 40 ºC and 60% humidity the γ-Al_2O_3 layers were dried for 3 h and calcined in air at a temperature of 650 ºC for 3 h (heating / cooling rate 1º C min^{-1}). Directly after coating, the silica layers were calcined in air at a temperature of 600 ºC for 3 h (heating / cooling rate 0.5 ºC min^{-1}).

2.2.5 Characterization

At different longitudinal positions on the inside of the 55 cm long tubular silica membranes SEM pictures were taken of the cross-section (Zeiss 1550 High Resolution SEM, at 1.5 kV).

Single gas permeation of flat plates and tubes was measured in a pressure controlled dead-end set-up. The measurements were performed at different temperatures (T = 150 - 450 °C), pressures (Δp = 1-4 bar and $p_{permeate}$= 1 atm) and gasses (helium, hydrogen, carbon dioxide, nitrogen, oxygen and methane). Prior to the measurements, the membranes were pretreated by permeating He or H_2 at 200 °C for 1 night. The single gas permeance was calculated from:

$$\boldsymbol{F} = \frac{\boldsymbol{N}}{\Delta \boldsymbol{p}} \qquad (1.1)$$

Where N is the molar flux through the membrane. The permselectivity F_α for gas i with respect to a gas j was calculated from the ratio of single gas permeance:

$$\boldsymbol{F_\alpha} = \frac{\boldsymbol{F_i}}{\boldsymbol{F_j}} \qquad (1.2)$$

To investigate the long-term stability of the membranes, measurements were conducted over a period of 2900 h.

Gas separation measurements were performed in a pressurized cross-flow cell at 250 °C (retentate flow = 45.8 L hr^{-1} consisted of 89% H_2 and 11% CH_4, permeate flow = 3.2 L hr^{-1}, permeate pressure = 1.45 bar). Gas selectivity for H_2 with repect to CH_4 was calculated from:

$$\alpha_{H_2/CH_4} = \left(\frac{\chi_{H_2}}{\chi_{CH_4}}\right)_{permeate} \cdot \left(\frac{\chi_{CH_4}}{\chi_{H_2}}\right)_{retentate} \quad (1.3)$$

Where χ is the mol fraction.

2.3 Results and discussion.

A typical stack of layers comprised in the tubular membranes is depicted in Figure 2.3. A distinct interface is present between the γ-alumina intermediate layer (thickness 3 μm) and the silica top layer (30 nm thick). The variation in silica layer thickness measured at different longitudinal positions in the tubes was within experimental error. As compared to flat supports prepared in this work and by others [18] the silica layer thickness of the tubular membranes was comparable, although different coating systems were used.

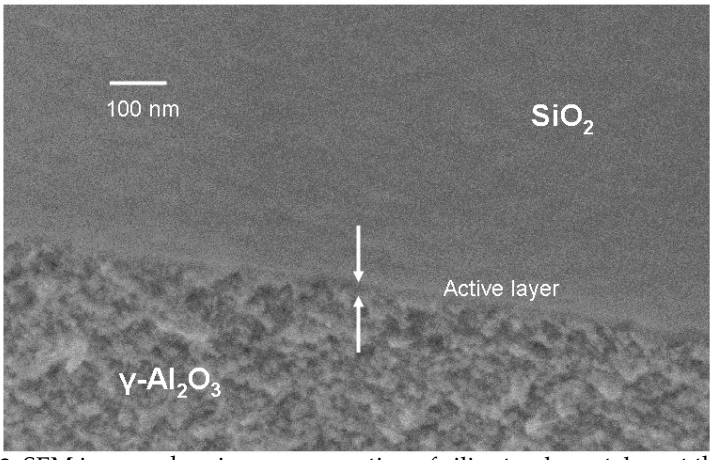

Figure 2.3: SEM images showing a cross section of silica top layer taken at the outer end of a 55 cm tubular membrane

The influence of the coating speed and concentration of the coat sol on the silica top layer was measured in another experiment and the results are depicted in Table 2.2. This table shows that the silica layer thickness increases with increasing coating speed and increasing sol concentration.

Sample preparation			XPS Profile	
Sample number	Coating speed (cm sec^{-1})	Sol concentration (10^{-1} mol L^{-1})	Layer thickness (nm)	Thickness layer SiO_2 intruded in Al_2O_3 (nm)
1	0,25	1,8	22	65
3	0,6	0,9	22	87
5	0,6	1,8	43	109
7	0,25	0,9	0	43

Table 2.2 Layer thickness as a function of coating parameters, determined from XPS analysis

Measurement at both ends of the tube shows no correlation between layer thickness and contact time, as the difference in layer thickness is within experimental error whereas the contact time at these locations is 10 and 220 s, respectively.

These observations suggest that the layer formation occurs via the dip coating process [1, 2] and capillary suction of the substrate has minor influence on the thickness of the layer. During dip coating, the withdrawal speed influences the amount of sol, which can flow back into the meniscus during coating; a slower coating speed creates thinner layers.

In Figure 2.4, single gas permeance data (T = 250°C, Δp = 2 bar) are presented as a function of the kinetic diameter of the permeating molecules for the different support geometries (flat, short, and long tubes). The observed trend, i.e., a high permeance for small molecules and a sharp decrease in permeance for larger molecules, is typical for micro-porous silica membranes. The performance of the tubular membranes is comparable to that of the on laboratory scale made flat plate membranes (ø = 39 cm) studied by De Vos and Verweij [18], notwithstanding that the surface area is 1000 times larger.

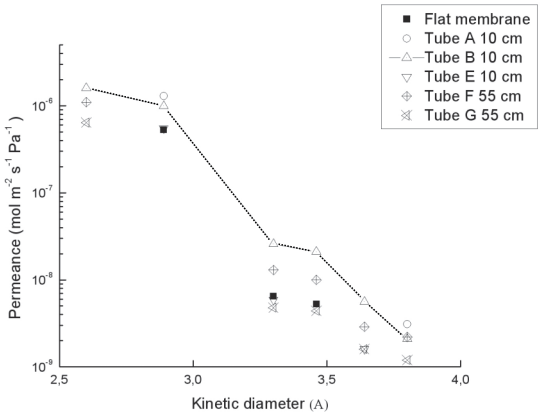

Figure 2.4: Permeance as function of kinetic diameter, line is a guide to the eye.

The data in Figure 2.4 indicates variations in permeation between the different samples. For each of the gases studied the change in permeance per sample is similar. Consequently, permselectivity does not vary significantly between the different samples.

Table 2.3 shows gas permeation data of 9 tubes. For both 10 cm as well as 55 cm long tubes hydrogen permeance is in the range $0.5 – 1 \times 10^{-6}$ mol m^{-2} s^{-1} Pa^{-1}. Tubes F and G (length 55 cm) display an average permselectivity of ~390 for helium of methane. The gas separation selectivity of hydrogen over methane of the other 55 cm tubes (H and I) is in the same range (~350). The performance of tubes A, B and E (10 cm) is comparable to that of the 55 cm tubes. The permselectivity of tubes C and D (10 cm) is lower. These tubes show a higher methane permeance ($0.5\text{-}1 \times 10^{-8}$ mol m^{-2} s^{-1} Pa^{-1}), possibly due to leakage of the glass sealing. The effect of leakage is more pronounced for the shorter tubes, because of the 5 times lower membrane surface area.

Tubular membrane	F_α H_2/CH_4	Permeance H_2	Tubular membrane	F_α He/CH_4	Permeance He	Separaton factor H_2/CH_4	Permeance H_2
10 cm		(10^{-7} mol $m^{-2}s^{-1}$ Pa^{-1})	55 cm		(10^{-7} mol $m^{-2}s^{-1}$ Pa^{-1})		(10^{-7} mol $m^{-2}s^{-1}$ Pa^{-1})
A	420	10					
B	490	10					
C	190	10					
D	110	10					
E	660	6					
			F	400	11		
			G	370	6.4		
			H			350	4.7
			I			360	5.1

Table 2.3: Permeance, permselectivity, and selectivity of tubular silica membranes, T = 250 °C, Δp = 2 bar

For membranes with a lanthanum doped γ-alumina layer and MAP bonding prolonged performance was tested in a dead-end gas permeation set-up for a total duration of 2900 h (Figure 2.5). In the first 2100 h the permeance was measured at temperatures up to 350 °C with different gases at different pressures. Figure 5 shows the permeation data of hydrogen, methane and carbon dioxide of tube B in time at a pressure difference of 3.8 bar. Permeance of the different gases did not vary significantly in time. Between 2100 and 2500 h the maximum temperature of the measurement was increased to 400 °C and 450 °C.

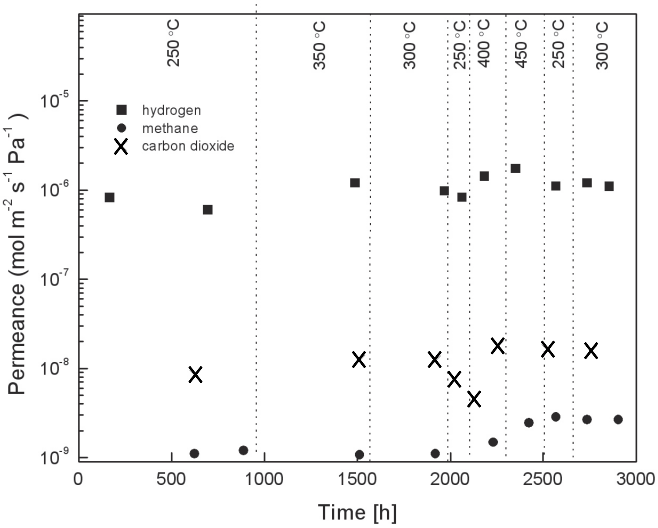

Figure 2.5: Prolonged membrane performance of tube B, single gas permeance (presented data obtained at T = 250 ºC, D_p = 3.9 bar)

The final gas permeance data, obtained after 2500 h, shows that membrane properties have changed irreversibly at temperatures >350 °C; a minor increase in permeance of hydrogen is observed, whereas permeance of methane (measured at 250 °C) increases 115%. The activation energy E_a for transport of hydrogen decreases from 19 kJ mol^{-1} to 6.3 kJ mol^{-1}. The changes in selectivity and activation energy suggest that after prolonged exposure to high temperature the pore morphology of the silica has

changed and an increased number of larger pores are present. The change in pore morphology is not unexpected, given the inherent non-equilibrium nature of this amorphous material. The changes in materials properties at temperatures that are low as compared to the calcination temperature of 600 °C appear to be related to the longer duration of exposure. The data acquired in the long-term measurement indicates that the high performance of the membranes can be maintained for more than 2100h at these conditions.

2.4 Conclusions

High performance micro-porous silica membranes have been coated on the inside of tubular supports up to 55 cm long, with a improved surface morphology. The performance of these membranes is reproducible and compares favorably with the performance of low surface area flat plate and short tubular (10 cm) membranes. At 250 °C and a pressure difference of 2 bar the 55 cm long tubular membranes display hydrogen permeance in the range 0.5 – 1 $\times 10^{-6}$ mol $m^{-2}s^{-1}Pa^{-1}$, and permselectivity of hydrogen with respect to methane in the range 350-400. At ≤ 350 °C, no significant changes in the permeance and permselectivity have been observed over a period of more than 2100 h.

The present method allows straightforward and reproducible coating of large surface area high performance silica membranes, and can be anticipated to be beneficial for commercial application of these membranes.

References

[1] C.J. Brinker, Sol-gel Science : the physics and chemistry of sol-gel processing, Academic Press, 1990.

[2] S.F.a.S. Kistler, P.M., Liquid film coating, Chapman & Hall, Cambridge, 1997.

[3] B.-K. Sea, M. Watanabe, K. Kusakabe, S. Morooka, S.-S. Kim, Formation of hydrogen permselective silica membrane for elevated temperature hydrogen recovery from a mixture containing steam, Gas Separation & Purification, 10 (1996) 187-195.

[4] G.-J. Hwang, J.-W. Kim, H.-S. Choi, K. Onuki, Stability of a silica membrane prepared by CVD using [gamma]- and [alpha]-alumina tube as the support tube in the HI-H_2O gaseous mixture, Journal of Membrane Science, 215 (2003) 293-302.

[5] S. Gopalakrishnan, M. Nomura, T. Sugawara, S.-i. Nakao, Preparation of a multi-membrane module for high-temperature hydrogen separation, Desalination, 193 (2006) 230-235.

[6] Y. Gu, P. Hacarlioglu, S.T. Oyama, Hydrothermally stable silica-alumina composite membranes for hydrogen separation, Journal of Membrane Science, 310 (2008) 28-37.

[7] T. Tsuru, T. Morita, H. Shintani, T. Yoshioka, M. Asaeda, Membrane reactor performance of steam reforming of methane using hydrogen-permselective catalytic SiO_2 membranes, Journal of Membrane Science, 316 (2008) 53-62.

[8] M. Asaeda, S. Yamasaki, Separation of inorganic/organic gas mixtures by porous silica membranes, Separation and Purification Technology, 25 (2001) 151-159.

[9] K. Kusakabe, F. Shibao, G. Zhao, K.-I. Sotowa, K. Watanabe, T. Saito, Surface modification of silica membranes in a tubular-type module, Journal of Membrane Science, 215 (2003) 321-326.

[10] T.A. Peters, J. Fontalvo, M.A.G. Vorstman, N.E. Benes, R.A.v. Dam, Z.A.E.P. Vroon, E.L.J.v. Soest-Vercammen, J.T.F. Keurentjes, Hollow fibre microporous silica membranes for gas separation and pervaporation: Synthesis, performance and stability, Journal of Membrane Science, 248 (2005) 73-80.

[11] Y. Yoshino, T. Suzuki, B.N. Nair, H. Taguchi, N. Itoh, Development of tubular substrates, silica based membranes and membrane modules for hydrogen separation at high temperature, Journal of Membrane Science, 267 (2005) 8-17.

[12] M.K. Koukou, N. Papayannakos, N.C. Markatos, M. Bracht, H.M. Van Veen, A. Roskam, Performance of ceramic membranes at elevated pressure and temperature: effect of non-ideal flow conditions in a pilot scale membrane separator, Journal of Membrane Science, 155 (1999) 241-259.

[13] C.-Y. Tsai, S.-Y. Tam, Y. Lu, C.J. Brinker, Dual-layer asymmetric microporous silica membranes, Journal of Membrane Science, 169 (2000) 255-268.

[14] K. Yoshida, Y. Hirano, H. Fujii, T. Tsuru, M. Asaeda, Hydrothermal Stability and Performance of Silica-Zirconia Membranes for Hydrogen Separation in Hydrothermal Conditions, Journal of Chemical Engineering of Japan, 34 (2001) 523-530.

[15] H.K. Arian Nijmeijer, Rune Bredesen and Henk Verweij., Preparation and Properties of Hydrothermlly Stable Gamma Alumina Membranes, Journal of the European Ceramic Society, 84 (2001) 136-140.

[16] A. Nijmeijer, Hydrogen-selective Silica Membranes for Use in Membrane Steam Reforming, PhD Thesis, (1999).

[17] R.M. De Vos, High-Selectivity, High-Flux Silica Membranes for Gas Seperation, (1998).

[18] R.M. De Vos, H. Verweij, Improved performance of silica membranes for gas separation, Journal of Membrane Science, 143 (1998) 37-51.

Chapter 3:

Al_2O_3 capillary supported PDMS membranes for solvent resistant nanofiltration.

This chapter is based on: S.M. Dutczak, M.W.J. Luiten-Olieman, H.J. Zwijnenberg, L.A.M. Bolhuis-Versteeg, L. Winnubst, M.A. Hempenius, N.E. Benes, M. Wessling, D. Stamatialis, Journal of Membrane Science, 372 (2011) 182-190.

Abstract

Solvent resistant nanofiltration (SRNF) is a membrane separation process allowing for an efficient separation of small molecules of 200-1000 g mol^{-1} from organic solvents. The application of SRNF in industry is currently hindered by a limited choice of SRNF membranes and configurations. Despite clear advantages of capillary membranes (high surface to volume ratio, no spacers required and therefore more compact and simpler modules can be built), commercial SRNF membranes are almost exclusively produced in a spiral wound form. In this work, SRNF capillary membranes have been prepared and studied, made of an Al_2O_3 support coated with a selective poly(dimethylsiloxane) (PDMS) top layer. The advantages of a ceramic support such as high mechanical, thermal and chemical stability will be combined with the excellent separation properties of the PDMS coating. The membranes are systematically investigated including: permeation experiments (permeance/molecular weight cut – off, MWCO) using a high-pressure set-up and study of morphology using SEM imaging. The prepared membranes are stable for at least 40 h in toluene and have MWCO of 500 Da.

3.1 Introduction

Solvent resistant nanofiltration (SRNF) is an energy-efficient separation process with high potential in many branches of industry, ranging from petro-chemistry [1] to pharmaceuticals [2-6]. SRNF is a relatively new membrane process capable of effective separation of molecules in the range of 200 - 1000 g mol^{-1} in various organic solvents. Most of the SRNF membranes reported in the literature are either asymmetric integrally skinned made of polyimides (PI) [7] or composites comprising of a thin PDMS separating layer on a polyacrylonitrile (PAN) [8-15] or PI porous support [16]. In order to improve the chemical resistance of PI membranes to organic solvents, a diamine crosslinking step has been applied, too [17, 18]. The crosslinking can be performed as a post casting process or be incorporated into the phase inversion process itself [19].
In industry, the majority of the organic solvent nanofiltration processes use commercial polymeric membranes, which are exclusively in a spiral wound form (e.g. SolSep NF 030306; MET Starmem™). The Starmem™ PI membranes have been used to separate phase transfer catalyst (PTC) from toluene [20, 21] and for the recovery of dewaxing solvents (e.g. toluene) from dewaxed lube oil filtrates in petrochemistry [22]. A recent publication also showed, that SolSep membranes can be successfully used in different separation and purification stages in the biodiesel production process [23].
A hollow fiber (HF) or capillary membrane provides a high surface-area-to-volume ratio and can withstand large hydrostatic pressures. Polymeric hollow fibers for aqueous systems are widely used in various biomedical, medical and industrial applications [24, 25]. However SRNF hollow fibers or capillary membranes are not available. Recently Loh et al. developed polyaniline (PANI) hollow fibers with good stability in dimethylformamide and acetone [26].
Ceramic supports, in contrast to polymeric support membranes [6, 27], offer high chemical stability for almost all organic solvents and no compaction occurs at high pressures. This makes them interesting candidates as membrane supports.

In this work the preparation of Al_2O_3 supported PDMS capillary membranes is presented; a commercial Hyflux InoCep M20 α-Al_2O_3 capillary support is coated with a selective poly(dimethylsiloxane) (PDMS) top layer. As a separation layer PDMS is chosen due to its well-established position in SRNF. To the best of our knowledge, this work is the first

reporting composite Al_2O_3/PDMS capillary membranes for SRNF. Other studies developed capillary/hollow fibers or tubular membranes based on a PDMS selective layer but only for pervaporation or VOC removal [28-31]. Membranes are systematically investigated including permeation experiments (permeance / MWCO) using a high pressure cross flow set-up and study of morphology using SEM imaging.

3.2 Experimental

3.2.1 Materials

α-Al_2O_3 capillaries, InoCep™ M20 (I.D. 2.8 mm, O.D. 3.8 mm) were purchased from HyFlux Ltd. (The Netherlands) with pore size of 20 nm on the inside of the capillary and 800 nm on the outside (as reported by the manufacturer). Toluene (for analysis) was purchased from Merck (The Netherlands). General Electric PDMS RTV 615 kit was purchased from Permacol B.V. (The Netherlands). The silicone kit consisted of two components; a vinyl terminated pre-polymer (RTV-A) and a Pt-catalyzed cross-linker (RTV-B) containing a polyhydrosilane component. As potting a two component epoxy resin Araldite® 2014-1 obtained from Viba (The Netherlands) was used and a Sauereisen electrical cement No. DW-30 from Sepp Zeug Gmbh & Co. Kg Adhesive Cements (Germany). Polystyrene was prepared in our group [32].

3.2.2 Sol synthesis

RTV 615 pre-polymer (RTV-A), 15% (w/w), was added to toluene and heated till 60°C under reflux and stirring. The crosslinking reaction started after adding component (RTV-B) and was terminated, after certain time, by placing the reaction mixture in an ice bath. Al_2O_3 capillaries were coated on the outside after plugging the end of the capillary via dip coating or on the inside via a communication vessel system, which is described in detail in paragraph 2.2.3. The coating speed was 0.9 cm/s and the contact time 30 sec. The membranes were kept at room temperature for 30 min to

evaporate the solvent. Subsequently, the coated tubes were incubated at 60°C for 8 h to complete the crosslinking reaction.

All membranes were prepared in an ISO-6 class cleanroom. The produced membranes were named CY/X. C indicates that the support is a capillary, Y is the pore diameter (nm) of the support and X is the viscosity (mPa s) of PDMS solution used for coating.

3.2.3 Module preparation

The membranes were potted in cross-flow stainless steel modules. Each module contained one capillary of 155 mm active length. The membrane area of each C800/X module was 1.86×10^{-3} m^2 and of the C20/X 1.36×10^{-3} m^2. Araldite® 2014-1 was used as a potting material for membranes C800/X. The resin was allowed to set at room temperature for minimum 24 h before permeation measurements. Potting fibers coated on the inside of the capillaries, C20/X, with Araldite® 2014-1 caused problems; cracks of the membrane were observed. These membranes were potted with Sauereisen electrical cement No. DW-30 and kept at room temperature for minimum 48 h.

3.2.4 Characterization

The viscosity of the PDMS mixtures was measurements at 25°C with a Brookfield DV-II+ Pro viscometer using a spindle nr-61 (ø18.9 mm) and glass cylinder (ø26 mm).

SEM images were taken of the cross-sections of the fibers (Jeol JSM5600LV, at 5 kV). The fibers were immersed in liquid nitrogen, before fracturing, to obtain a well-defined cross-section and dried in vacuum oven at 30°C for 12 h. Samples were sputtered with gold (Balzers Union SCD 040, 4 min, current 13 mA).

The concentration of the PS oligomers as a function of MW in the feed and permeate stream was determined by GPC chromatography (Agilent Technologies 1200 Series" GPC system, detector Shodex RI-71, colomn PSS SDV with porosity 1000 Å). As a mobile phase analytical grade toluene was

used. To obtain retention curves, the data was processed by the GPC software (Win GPC Unity).
Gas permeation measurements were performed in a constant volume/variable pressure set up (see details elsewhere [33]). The gas permeance values were calculated based on a pressure increase in a calibrated constant volume at the permeate side, at 30°C.

3.2.5 PDMS layer thickness determination

The PDMS layer consist of a layer on top of the support (l_{top}) and a layer intruded in the support (l_{intr}). The total PDMS layer thickness (l_{total}) was calculated based on the gas permeation measurements, assuming that the PDMS intrinsic permeability of N_2 equals $9.4 \cdot 10^{-14}$ mol $m^{-1}s^{-1}Pa^{-1}$ and CO_2 $1.1 \cdot 10^{-12}$ mol $m^{-1}s^{-1}Pa^{-1}$ [34]. The l_{top} was obtained from SEM images of cross sections of at least three different membranes per case and an average of five SEM images per cross section. Subsequently, l_{intr} could be calculated.

3.2.6 Permeation experiments

Permeation experiments were performed in cross-flow high-pressure permeation set up (Figure 3.1) in a total recycle mode, at 18°C. A gear pump was used for circulation and equipped with frequency inverter allowing precise control over the cross flow velocity, the cross flow velocity of the feed solution was kept above 2 m s^{-1}. An HPLC pump was used to pressurize the system up to 40 bar. Permeation experiments were performed for around 20 h in a total recycle mode.

The membranes C800/X, with a PDMS layer on the outside of the capillary, have been tested outside-in and the C20/X, with PDMS layer on the inside, inside-out. The flux through the membrane [J, in L $m^{-2}h^{-1}$] was calculated using the following equation:

$$J = \frac{V}{A \cdot t}$$

where V is the permeate volume [L], A the membrane area [m^2] and t is the permeation time [h]. The permeance coefficient, P [L $m^{-2}h^{-1}bar^{-1}$], was calculated from the slope of the flux versus trans membrane pressure (TMP) graph:

$$\boldsymbol{P} = \frac{\boldsymbol{J}}{\Delta \boldsymbol{p}}$$

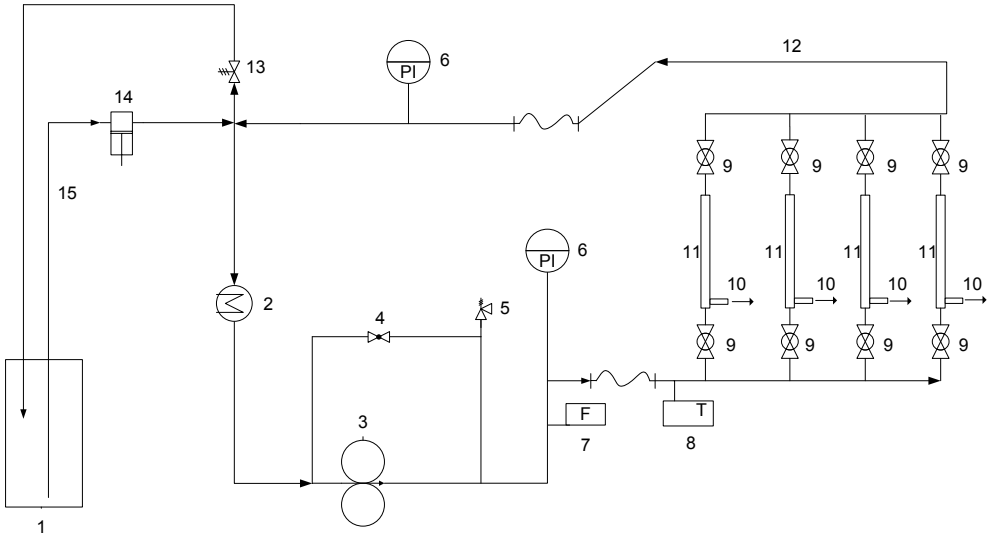

Figure 3.1: High pressure permeation set up: 1) feed vessel, 2) heat exchanger, 3) gear pump, 4) bypass ball valve, 5) pressure relief, 6) pressure indicator, 7) flow meter, 8) temperature controller, 9) ball valves, 10) permeate line, 11) membrane modules, 12) retentate line, 13) back pressure valve, 14) HPLC pump, 15) feed line

3.3 Results and discussion

For the preparation of membranes with high flux and high separation a low concentration PDMS coat solution (in toluene) is required with a viscosity around 100 mPa s. To achieve this the coating solution is pre-crosslinked [11].

In Figure 3.2 the viscosity of a 15 % (w/w) PDMS solution is depicted as a function of crosslinking reaction at different temperatures. Pre-crosslinking at 60 °C (procedure described by Stafie et al. [10, 12]) result in a sharp increase in viscosity in a short time; a minor change in reaction time at this moment results in a major increase in viscosity which makes it difficult to produce a sol with a certain viscosity in a reproducible manner.

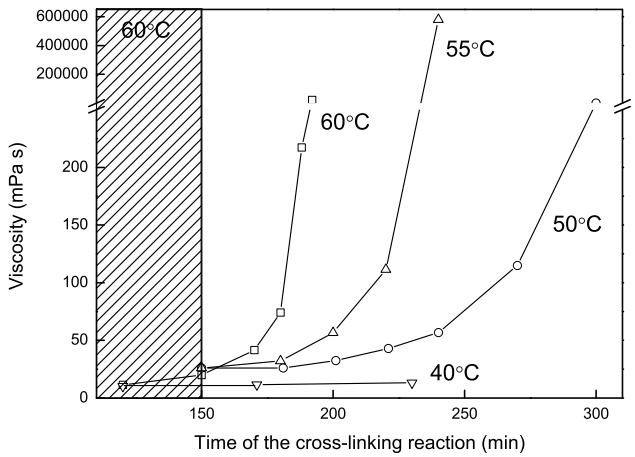

Figure 3.2 : Crosslinking of PDMS coating solutions, first step at the same temperature (60°C) followed by a step at different temperatures for the 4 coating sols (measurement error is less than 10%)

To improve the preparation method, the reaction temperature was lowered after 150 min. to resp. 55°C, 50°C and 40°C. At lower temperatures, the increase in viscosity is significantly lower. The viscosity increase at 50°C (after 150 min) was most gradually and preferable for future experiments.

Preliminary coating experiments with 15 % (w/w) solution showed that the layer thickness was too high and a more diluted coat sol was required to decrease the layer thickness.

Crosslinking solutions with lower PDMS concentrations resulted in no change in viscosity in the first 8 h and a method was developed starting with a 15 % (w/w) and diluting it during the crosslinking reaction. The results are plotted in Figure 3.3 where the viscosity is plotted as function of the reaction time.

In the first step a 15% (w/w) solution was crosslinked for 150 min at 60ºC and subsequently for 120 min at 50ºC. Next, in step II the solution was diluted with toluene to 7.5% (w/w) and crosslinking was continued at 60ºC for 120 min. Then, in step III, the mixture was diluted again to 3.75% (w/w) and the reaction continued at 60ºCfor 150 min. The results show that one can tailor the viscosity of diluted solutions. Coat sols (3.75% (w/w)) with different viscosities, 55, 69, 100 and 245 mPa s, were selected for the preparation of membranes

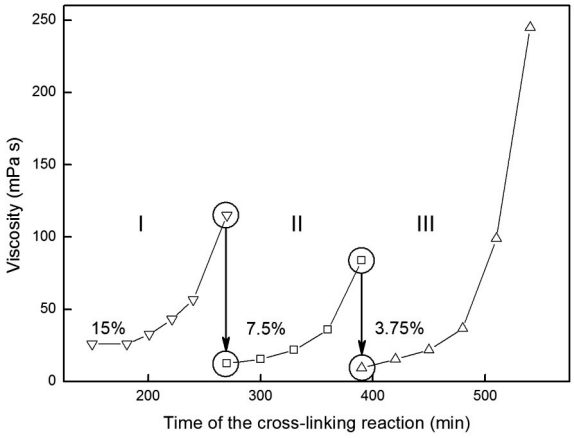

Figure 3.3: Viscosity as function of the crosslinking of PDMS coating solutions: effect of dilution on viscosity of PDMS coating solution (measurement error is less than 10%)

SEM images of the cross section of the Hyflux InoCep M20 support are depicted in Figure 3.4. The support has pores of 800 nm (as reported by the manufacturer) and is coated on the inside with α-Al_2O_3 (~5 μm layer thickness). This coated layer contains pores of 20 nm (according to the manufacturer).

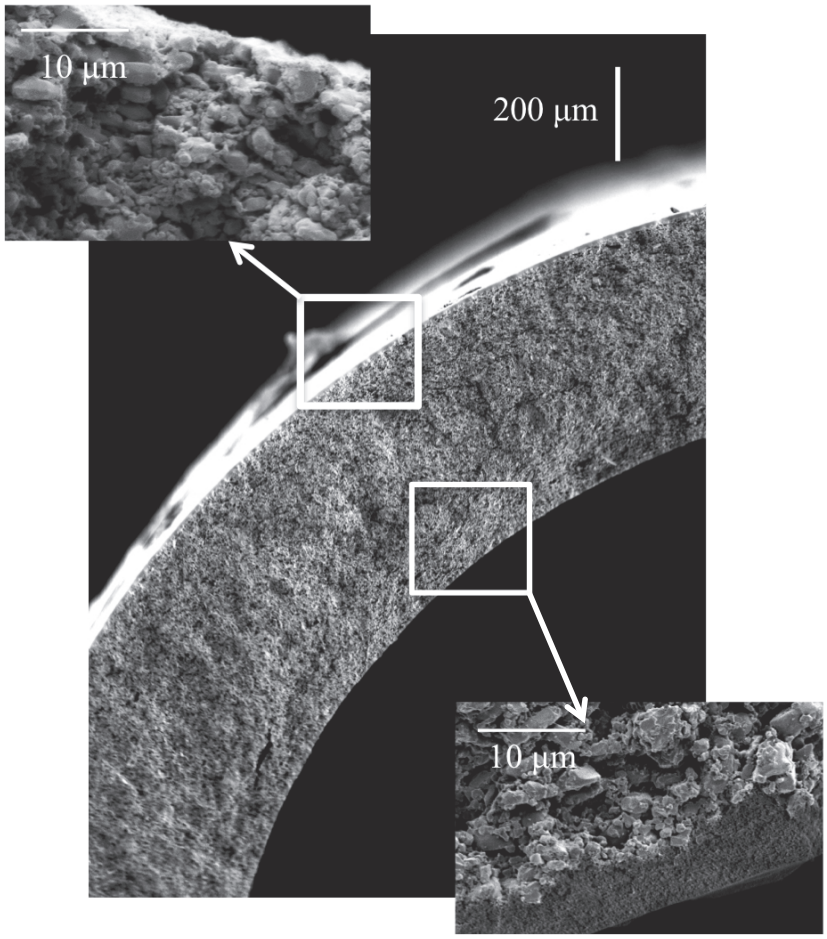

Figure 3.4 : SEM images of Hyflux InoCep M20 capillary support with on top a detailed cross-section of the outer layer and on the bottom of the inner layer

Figure 3.5 presents the flux of toluene as a function of transmembrane pressure (TMP). Because of the very high flux of toluene through InoCep M20 support we were not able to apply higher pressures in our experimental set up. The toluene permeance of the M20 capillary is 575 ± 5 l $m^{-2}h^{-1}bar^{-1}$.

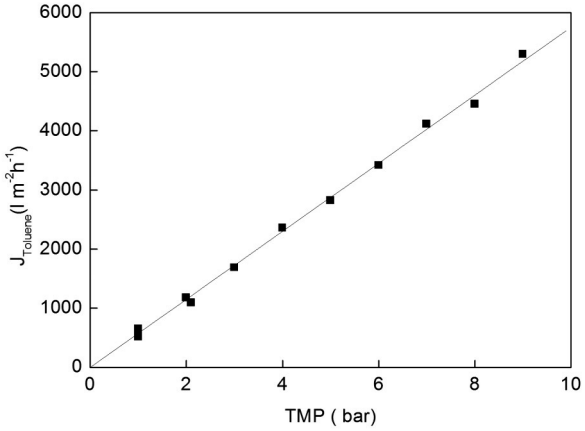

Figure 3.5 Toluene flux as function of transmembrane pressure of a Hyflux Inocep C20 support

In Table 3.1 an overview is presented of the coating experiments. In the first experiment the coating was applied on the outside of the fiber (pore size of support = 800 nm). In the second experiment the coating was applied on the inside of the Al_2O_3 capillary (pore size of the support = 20 nm).

Code	Support pore size, [nm]	PDMS [w/w %]	Viscosity [mPa s]
C800/69	800	3.75%	69
C800/100	800	3.75%	100
C800/245	800	3.75%	245
C20/55	20	3.75%	55
C20/245	20	3.75%	245

Table 3.1 Characteristics of membranes

The coat sol contains the same concentration of PDMS (3.75 % (w/w)) but the viscosity of the sol varies between 55 and 245 mPa s. After coating SEM images were taken and depicted in Figure 3.6.

Two images, displayed on top, are SEM images of capillaries coated with a low viscosity coat sol (~60 mPa s) resulting in a thin layer on top of the support. On the left side, the coating was deposited on a support with larger pore size (800nm), pore intrusion can be seen, while that is not visible in the SEM image on the right (support with smaller pore size 20 nm). On the bottom 2 SEM images are depicted of fibers coated with a higher viscous coat sol (245 mPa s). On both images no pore intrusion is visible, but the coating on top is rather thick > 15 μm.

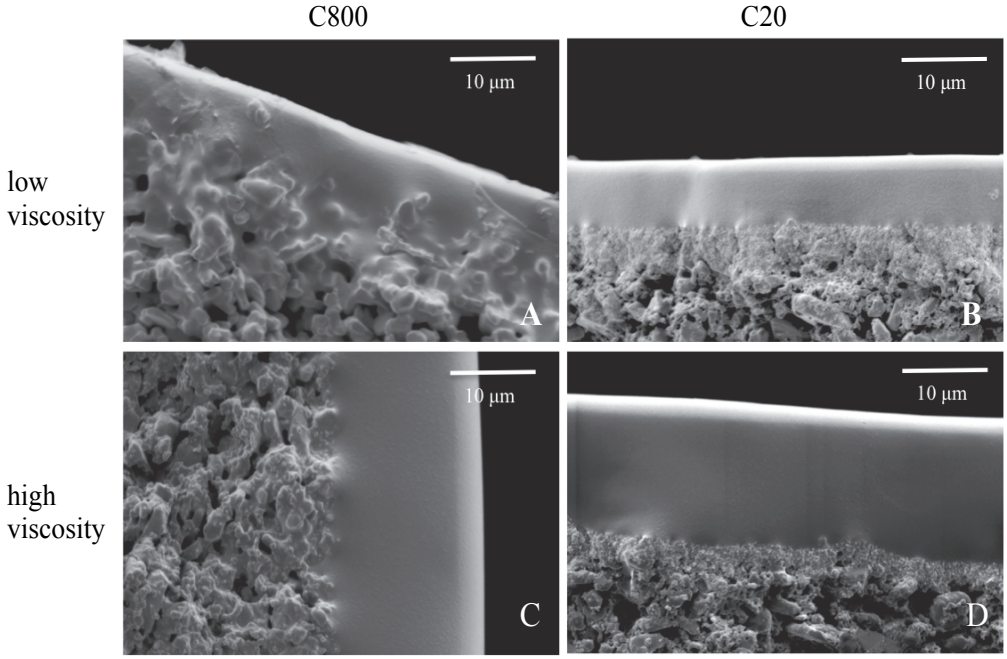

Figure 3.6: Al_2O_3 supported PDMS membrane: (A) C800/69, (B) C20/55. (C) C800/245, (D) C20/245

Gas permeation data has been measured to quantify the intruded layer. The calculation of the total layer thickness can only be used for high quality membranes, because defects influence the results. The selectivity, $\alpha_{CO2/N2}$, can be used a quality check. For fibers coated on Al_2O_3 supports with pores of 800 nm $\alpha_{CO2/N2}$ was above 10 (the ideal $\alpha_{CO2/N2}$ is 11.3 [11]) showing a

good quality of the coating but for membranes C20/X the $\alpha_{CO2/N2}$ was ~8.4 indicating some defects in the separation layer. These defects influence the gas permeation measurements leading to a slightly lower calculated total PDMS layer thickness.

In Table 3.2 the results are presented showing the layer thickness on top of the support, l_{top}, measured with SEM, the calculated total layer thickness, l_{total}, based on the gas permeation measurements, and the calculated PDMS layer in the support, l_{intr}.

Code	Viscosity [mPa s]	l_{top}, [μm]	l_{intr}, [μm]	l_{total}, [μm]	Toluene permeance [L $m^{-2}h^{-1}bar^{-1}$]
C20/55	55	7.3±0.3	0	7.1±0.2	1.6 ± 0.1
C20/245	245	16±4	0	16±1	0.9 ± 0.6
C800/69	69	6±3	45	51±1	0.07 ± 0.01
C800/100	100	10±1	18	28±1	0.22 ± 0.02
C800/245	245	18±3	14	32±6	0.14 ± 0.02

Table 3.2: Layer thickness of PDMS membranes

For the supports of 20 nm pores (C20), the calculations shows that almost no pore intrusion have taken place. Increasing the viscosity of the coat sol results in an increase in PDMS layer thickness. The layer thickness increases with the square root of the viscosity. This confirms that film formation occurs via 'film coating', described by the relation $h_\infty = 2/3 (v\eta/\rho g)^{-0.5}$ [35].

In contrast, for the supports with 800 nm pore diameter an increase in viscosity of the coat sol results in a decrease in total layer thickness. The total layer thickness of the membranes coated on a support with 800 nm pore is more than 2 times larger than membranes coated on support with

20 nm pore size. Here, in addition to film coating slips casting occurs, resulting in a more intruded layer for lower viscous coat sol.

Liquid permeation (toluene) results are presented in Figure 3.7. The error bars represent deviation between the samples of the membranes (at least 3 membranes) from the same batch. For a single fiber, results of repeated measurements differ <1%. Within the studied pressure range the lines remains straight indicating that no membrane compaction has occurred. The toluene flux of membranes coated on a support with 800 nm pores is significantly lower as compared to the membranes coated on 20 nm supports. This is expected, because the total layer thickness was more than 2 times higher. Comparing the flux data of these measurements with the total layer thickness shows that an increase of total layer thickness results in a decrease of flux.

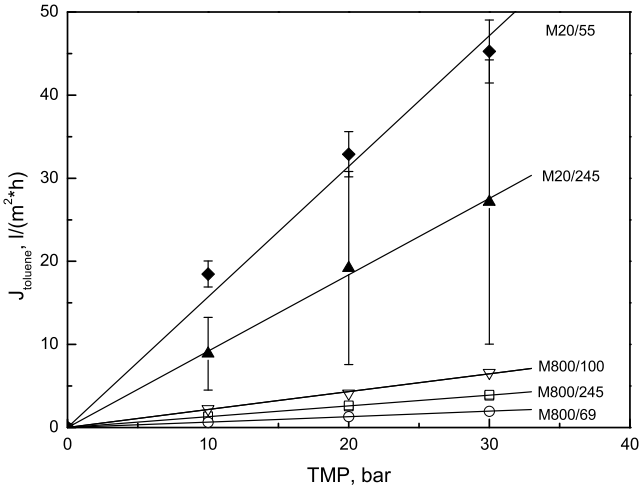

Figure 3.7: Toluene flux as function of TMP of Al_2O_3 / PDMS hollow fiber membranes

For membranes on a support with smaller pores (C20/55 and C20/245) the permeation of toluene is significant higher. A high standard deviation was found for the membrane C20/245. The low reproducibility could be caused by the high viscosity of the low concentrated coat solution (3.75 %), which can result in samples with non-uniform top layer.
The reproducibility of the C20/55 composite membranes is considerably better as demonstrated by the small thickness deviation between the samples (see Table 3.2). The thickness of the PDMS layer of our membrane

C20/55 is 7 μm and is lower than that reported for other capillary membranes for pervaporation (~10μm) [29] and hollow fibers for VOC removal (15.4 μm) [28]. In conclusion, the membranes prepared on a 20 nm pores support, coated with a 3.75 % (w/w) PDMS sol with a viscosity of 55 mPa s, display the highest permeance and were used for molecular weight cut-off characterization.

Figure 3.8 (left) presents the flux of pure toluene and the flux of toluene/PS oligomers as function of TMP for the C20/55 membrane. The data show a comparable linear relation between permeance and pressure for toluene with or without the PS oligomers. Hence, for the chosen concentration of PS oligomers concentration polarization phenomena have no significant effect on solvent permeance, and in this pressure range no compaction occurs either. Figure 3.8 reveals a permeance of $P_{toluene}$ = 1.6 ± 0.1 L $m^{-2}h^{-1}bar^{-1}$ and MWCO of 500 Da.

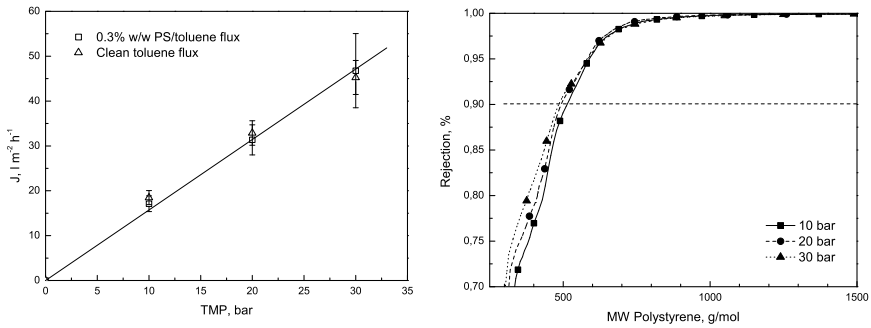

Figure 3.8: Transport through C20/55 membrane; on the left toluene and toluene-PS transport through the membrane and on the right PS oligomer retention by the membrane

As compared to some silicone based composite membranes reported in literature, the developed Al_2O_3 supported PDMS membrane has comparable performance (PAN-PE/PDMS. 1.2 L $m^{-2}h^{-1}bar^{-1}$ [27]; PAN/PDMS 2.0 L $m^{-2}h^{-1}bar^{-1}$[10]). The permeance is lower compared to that of the PAN/PDMS membrane reported by Ebert et al. (8.2 L $m^{-2}h^{-1}bar^{-1}$ and 90% retention of PEG 900, [9]) and Gevers et al., (3.3 L $m^{-2}h^{-1}bar^{-1}$ and 98 % rejection of the Wilkinson catalyst 952 Da [16]). MPF-50 (Koch) has comparable performance; a toluene permeance of 1.3 L $m^{-2}h^{-1}bar^{-1}$ and MWCO about 700 Da [6]. Comparing to non-silicone NF membranes, a

cross-linked polyimide membrane developed by See Toh et al. has a toluene permeance 3.2 L $m^{-2}h^{-1}bar^{-1}$ and MWCO 400 Da, based on PS oligomers rejection [17]. Polyimide Starmem™ membrane has a toluene permeance 1.8 L $m^{-2}h^{-1}bar^{-1}$ and MWCO 220 Da, based on rejection of n-alkanes [6, 13].

3.4 Conclusions

In this work, we have developed PDMS toplayer on an Al_2O_3 commercial Hyflux InoCep M20 α- Al_2O_3 capillary support. The total PDMS layer thickness is influenced by the pore size distribution of the support; a support with larger pores (800 nm) allows for more pore intrusion than a support with smaller pores. The layer thickness on top of the support can be tuned by changing the viscosity of the coat sol; lower viscosity results in a thinner layer. Liquid permeation data showed a higher permeance for thinner PDMS layers.

A PDMS membrane on Al_2O_3 capillary, prepared of a 3.75 %(w/w) PDMS sol (viscosity 55 mPa s), displays the highest toluene permeance, 1.6 L $m^{-2}h^{-1}bar^{-1}$, combined with a MWCO of ~500 Da (based on PS). This membrane shows stable performance for over 40 h in toluene.

References

[1] L.S. White, Development of large-scale applications in organic solvent nanofiltration and pervaporation for chemical and refining processes, Journal of Membrane Science, 286 (2006) 26.

[2] X. Cao, X.Y. Wu, T. Wu, K. Jin, B.K. Hur, Concentration of 6-aminopenicillanic acid from penicillin bioconversion solution and its mother liquor by nanofiltration membrane, Biotechnology and Bioprocess Engineering, 6 (2001) 200-204.

[3] J.C.T. Lin, A.G. Livingston, Nanofiltration membrane cascade for continuous solvent exchange, Chemical Engineering Science, 62 (2007) 2728-2736.

[4] J.P. Sheth, Y. Qin, K.K. Sirkar, B.C. Baltzis, Nanofiltration-based diafiltration process for solvent exchange in pharmaceutical manufacturing, Journal of Membrane Science, 211 (2003) 251-261.

[5] D. Shi, Y. Kong, J. Yu, Y. Wang, J. Yang, Separation performance of polyimide nanofiltration membranes for concentrating spiramycin extract, Desalination, 191 (2006) 309-317.

[6] P. Vandezande, L.E.M. Gevers, I.F.J. Vankelecom, Solvent resistant nanofiltration: Separating on a molecular level, Chemical Society Reviews, 37 (2008) 365-405.

[7] Y.H. See-Toh, F.C. Ferreira, A.G. Livingston, The influence of membrane formation parameters on the functional performance of organic solvent nanofiltration membranes, Journal of Membrane Science, 299 (2007) 236-250.

[8] S. Aerts, A. Vanhulsel, A. Buekenhoudt, H. Weyten, S. Kuypers, H. Chen, M. Bryjak, L.E.M. Gevers, I.F.J. Vankelecom, P.A. Jacobs, Plasma-treated PDMS-membranes in solvent resistant nanofiltration: Characterization and study of transport mechanism, Journal of Membrane Science, 275 (2006) 212.

[9] K. Ebert, J. Koll, M.F.J. Dijkstra, M. Eggers, Fundamental studies on the performance of a hydrophobic solvent stable membrane in non-aqueous solutions, Journal of Membrane Science, 285 (2006) 75-80.

[10] N. Stafie, Poly(dimethyl siloxane) – based composite nanofiltration membranes for non-aqueous applications, Ph.D. thesis, University of Twente, Enschede, The Netherlands, (2004).

[11] N. Stafie, D.F. Stamatialis, M. Wessling, Insight into the transport of hexane-solute systems through tailor-made composite membranes, Journal of Membrane Science, 228 (2004) 103-116.

[12] N. Stafie, D.F. Stamatialis, M. Wessling, Effect of PDMS cross-linking degree on the permeation performance of PAN/PDMS composite nanofiltration membranes, Separation and Purification Technology, 45 (2005) 220-231.

[13] D.F. Stamatialis, N. Stafie, K. Buadu, M. Hempenius, M. Wessling, Observations on the permeation performance of solvent resistant nanofiltration membranes, Journal of Membrane Science, 279 (2006) 424-433.

[14] E.S. Tarleton, J.P. Robinson, C.R. Millington, A. Nijmeijer, M.L. Taylor, The influence of polarity on flux and rejection behaviour in solvent resistant nanofiltration--Experimental observations, Journal of Membrane Science, 278 (2006) 318-327.

[15] E.S. Tarleton, J.P. Robinson, M. Salman, Solvent-induced swelling of membranes -- Measurements and influence in nanofiltration, Journal of Membrane Science, 280 (2006) 442-451.

[16] L.E.M. Gevers, S. Aldea, I.F.J. Vankelecom, P.A. Jacobs, Optimisation of a lab-scale method for preparation of composite membranes with a filled dense top-layer, Journal of Membrane Science, 281 (2006) 741-746.

[17] Y.H. See Toh, F.W. Lim, A.G. Livingston, Polymeric membranes for nanofiltration in polar aprotic solvents, Journal of Membrane Science, 301 (2007) 3-10.

[18] K. Vanherck, P. Vandezande, S.O. Aldea, I.F.J. Vankelecom, Cross-linked polyimide membranes for solvent resistant nanofiltration in aprotic solvents, Journal of Membrane Science, 320 (2008) 468-476.

[19] K. Vanherck, A. Cano-Odena, G. Koeckelberghs, T. Dedroog, I. Vankelecom, A simplified diamine crosslinking method for PI nanofiltration membranes, Journal of Membrane Science, 353 (2010) 135-143.

[20] A. Livingston, L. Peeva, S. Han, D. Nair, S.S. Luthra, L.S. White, L.M. Freitas Dos Santos, Membrane Separation in Green Chemical Processing, Annals of the New York Academy of Sciences, 984 (2003) 123-141.

[21] S.S. Luthra, X. Yang, L.M. Freitas dos Santos, L.S. White, A.G. Livingston, Homogeneous phase transfer catalyst recovery and re-use using solvent resistant membranes, Journal of Membrane Science, 201 (2002) 65-75.

[22] L.S. White, C.R. Wildemuth, Aromatics enrichment in refinery streams using hyperfiltration, Industrial and Engineering Chemistry Research, 45 (2006) 9136-9143.

[23] R. Othman, A.W. Mohammad, M. Ismail, J. Salimon, Application of polymeric solvent resistant nanofiltration membranes for biodiesel production, Journal of Membrane Science, 348 (2010) 287-297.

[24] I. Moch, Hollow-Fiber Membranes, Kirk-Othmer Encyclopedia of Chemical Technology, in: Kirk-Othmer Encyclopedia of Chemical Technology, Wiley, 2005.

[25] S. McKelvey, A, D. Clausi, T., W.J. Koros, A guide to establishing hollow fiber macroscopic properties for membrane applications, Journal of Membrane Science, 124 (1997) 223-232.

[26] X.X. Loh, M. Sairam, J.H.G. Steinke, A.G. Livingston, A. Bismarck, K. Li, Polyaniline hollow fibres for organic solvent nanofiltration, Chemical Communications, (2008) 6324-6326.

[27] I.F.J. Vankelecom, K. De Smet, L.E.M. Gevers, A. Livingston, D. Nair, S. Aerts, S. Kuypers, P.A. Jacobs, Physico-chemical interpretation of the SRNF transport mechanism for solvents through dense silicone membranes, Journal of Membrane Science, 231 (2004) 99-108.

[28] S. Liu, W.K. Teo, X. Tan, K. Li, Preparation of $PDMS^{vi}$-Al_2O_3 composite hollow fibre membranes for VOC recovery from waste gas streams, Separation and Purification Technology, 46 (2005) 110-117.

[29] F. Xiangli, Y. Chen, W. Jin, N. Xu, Polydimethylsiloxane (PDMS)/Ceramic Composite Membrane with High Flux for Pervaporation of Ethanol-Water Mixtures, Industrial and Engineering Chemistry Research, 46 (2007) 2224-2230.

[30] F. Xiangli, W. Wei, Y. Chen, W. Jin, N. Xu, Optimization of preparation conditions for polydimethylsiloxane (PDMS)/ceramic composite pervaporation membranes using response surface methodology, Journal of Membrane Science, 311 (2008) 23-33.

[31] G.O. Yahaya, Separation of volatile organic compounds (BTEX) from aqueous solutions by a composite organophilic hollow fiber membrane-based pervaporation process, Journal of Membrane Science, 319 (2008) 82-90.

[32] H.J. Zwijnenberg, S. Dutczak, M.E. Boerrigter, M. Hempenius, M. Luiten-Olieman, N.E. Benes, M. Wessling, D. Stamatialis, Important factors influencing molecular weight cut-off determination of membranes in organic solvents Journal of Membrane Science, (2011).

[33] S.R. Reijerkerk, M.H. Knoef, K. Nijmeijer, M. Wessling, Poly(ethylene glycol) and poly(dimethyl siloxane): Combining their advantages into efficient CO2 gas separation membranes, Journal of Membrane Science, 352 (2010) 126-135.

[34] R. Baker, Membrane Technology and Applications, 2nd Edition John Wiley & Sons, Ltd, 2004.

[35] M. Mulder, Basic Principles of Membrane Technology, first ed., Kluwer Academic Publishers, Dordrecht, 2000.

Chapter 4:

Porous stainless steel hollow fiber membranes via dry-wet spinning

THIS CHAPTER HAS BEEN PUBLISHED:

Mieke W. J. Luiten-Olieman, Louis Winnubst, Arian Nijmeijer, Matthias Wessling, Nieck E. Benes, Porous stainless steel hollow fibers membranes via dry-wet spinning, Journal of Membrane Science, 370 (2011) 124-130

Abstract

Porous stainless steel hollow fibers have been prepared via the dry-wet spinning process, based on phase inversion of a particle loaded polymer solution, followed by sintering. The morphology of the green fibers combines sponge like structures and macrovoids, and is related to the dynamics of the phase inversion process. The morphology can be tuned by changing the spinning conditions and the composition of the spinning mixture. In analogy to their ceramic counterparts the morphology of the stainless steel fibers is preserved during sintering, apart from shrinkage due to densification. At a length scale comparable to the diameter of the steel particles the microstructure and related pore size distribution are more strongly affected by the sintering temperature, as compared to their ceramic counterparts. Sintering the stainless hollow fibers at temperatures > 1100 °C results in a sharp decrease in nitrogen permeance and an increase in bending strength, due to densification. The strength (~1 GPa) and nitrogen permeance (0.1 mmol m^{-2} Pa^{-1} s^{-1} at 21 °C) of stainless steel fibers sintered at 1050 - 1100 °C are superior as compared to their ceramic counterparts. The excellent properties of the stainless steel hollow fibers make them suitable as membrane (supports) for applications involving harsh environments.

4.1. Introduction

The combination of high chemical, thermal and mechanical stability of ceramic and metal (inorganic) membranes offers an interesting alternative for separation processes where organic polymer membranes suffer from limited stability. Their resistance against high pressures, high temperatures, and corrosive environments allow ceramic membranes to be used in a variety of applications. Major drawbacks of ceramic membranes include their brittleness. In contrast, metal membranes have a high mechanical strength, offer good thermal shock resistance, and allow for welding or brazing. Other distinct properties of metal membranes are their electrical and thermal conductivities. Porous metal is often used as membrane support [1] for different top layers; including nickel [2], palladium [3-5], zeolites [6], and sol-gel derived metal oxides (SiO_2, TiO_2, ZrO_2) [7]. Corresponding applications include carbon dioxide separations, water gas shift reactions, and reforming reactions [8-11].

The geometry of porous stainless steel membranes is generally tubular or flat. In this chapter we describe the preparation and characterization of porous stainless steel hollow fibers (outer diameters between 1.2 - 1.5 mm) prepared via the dry-wet spinning process, based on the principle of phase inversion [12] (see chapter 1.1).

The aim of this study is to develop a porous stainless steel hollow fiber with an outer surface that is sufficiently smooth (without macrovoids) for applying thin and defect free selective top layers.

4.2. Experimental

4.2.1 Materials

Stainless steel powder (316L) with particle size of 4.17 μm (D50 by the manufacturer) was purchased from Epson Atmix Corporation (Japan). Polyethersulfone (PES, Ultrason, 6020P) was used as polymer and N-methylpyrrolidone (NMP, 99,5wt%, Aldrich) as solvent. Polyvinylpyrrolidone (PVP K95, Aldrich) was used as viscosity enhancer and de-ionized water as non-solvent. The stainless steel powder and PES

were dried before use; all other chemicals were used without further treatment.

4.2.2 Preparation of spinning mixtures

Stainless steel powder (48, 70 or 80 wt%) was added to a mixture of NMP and H_2O (0-3 wt%) and followed by stirring for one hour. Subsequently, PES was added in three steps with a time interval of 2 hours, and stirred overnight. For rheology measurements the order in which the chemicals were added can be different, as is indicated in Table 4.1. For some experiments PVP (1 – 2 wt%) was added to regulate the viscosity of the mixture (see Table 4.1) followed by stirring overnight. Prior to spinning, the spinning mixture was degassed by applying vacuum for 30 min and left overnight under dry air. Table 4.1 gives an overview of the spinning mixture compositions used in this study.

Experiment	Stainless steel (wt%)	NMP (wt%)	PES (wt%)	PVP (wt%)	H_2O (wt%)	Order in which chemicals are added
1	48	40.0	9.7	2	0	NMP/SS/PES/PVP
2	70	21.7	7.3	1	0	NMP/SS/PES/PVP
3	80	15.0	5.0	0	0	NMP/SS/PES
4	48	39.0	13.0	0	0-3.5	NMP/SS/PES/H_2O
5	70	22.5	7.5	0	0-2.5	NMP/SS/PES/H_2O
6	80	15.0	5.0	0	0-1	NMP/SS/PES/H_2O
7	70	21.0	7.0	0	2.0	NMP/H_2O/SS/PES
8	48	37.5	12.5	0	2.0	NMP/H_2O/SS/PES
9	48	37.5	12.5	0	2.0	NMP/H_2O/SS/PES

Table 4.1: Composition of spinning mixtures of the performed experiments

4.2.3. Viscosity measurements

The rheology of the spinning mixture was measured with a Brookfield viscometer (DV-II$^+$ Pro) at different speeds (0.3-100 rotations per minute) with spindle LV4-64 at 20 ± 1 °C.

4.2.4 Spinning experiments

Spinning mixtures were pressurized in a stainless steel vessel using nitrogen (2 bar), and consequently pressed through a spinneret (inner and outer diameter of 0.8 mm / 2.0 mm, respectively). De-ionized water was pumped though the bore of the spinneret with a speed of 7 ml min^{-1}. The coagulation bath contained tap water and the length of the air gap was 3 cm. All spinning experiments were carried out at ambient temperature (20-21 °C) and an overview of the spinning conditions are mentioned in Table 4.2.

Condition	Value
Compostion spinning mixture	see Tabel 1
Bore liquid	H_2O
External coagulant	H_2O
Mixture extrusion pressure (bar)	2
Air gap (cm)	3
Bore liquid flow rate (ml/min)	7
Spinneret diameter (mm)	OD/ID=2.0/0.8
Temperature (°C)	21
Relative humidity (%)	40

Table 4.2 Spinning conditions

4.2.5 Drying and sintering

After spinning the fibers were first kept in a water bath for 1 day for removing traces of NMP, followed by drying and stretching (1 cm per m) for 1 day. The removal of the polymer was performed at 600 °C for 60 min (heating rate 5 °C min^{-1}) and fibers were sintered at 1050 °C, 1100 °C, 1150 °C or 1200 °C for 30 or 60 min (heating rate 5 °C min^{-1}, cooling rate 10 °C min^{-1}) in a nitrogen atmosphere. Unless mentioned otherwise, the sintering time was 60 min.

4.2.6 Characterization

SEM images were taken of the cross-sections of the fibers. The samples of the green compact were immersed into liquid nitrogen before fracturing, to obtain a well-defined cross-section (JEOL JSM 5600 LV, at 1,5 kV).

The thermogravimetric spectra were recorded on a Netzsch STA 449 F3 under nitrogen environment at a heating rate of 5 °C min^{-1} over a range of 25 - 800 °C.

Mechanical strength (σ) was measured with a 4 point bending test (Instron 5564A). The bending strength was calculated from:

$$\sigma = \frac{16FKd_o}{\pi(d_o^4 - d_i^4)} \tag{4.1}$$

In this equation F is the force at fracture, K half of the difference between outer and inner span (= 5 mm), and d_i and d_o are the inner and outer diameter diameters of the hollow fiber, respectively.

The pore size distribution was measured using two different techniques: with a capillary flow porometer based on the principle of the liquid extrusion porometry technique (Porolux 1000, IB-FT GmbH), and with a mercury porosimetry analyzer (Poremaster PM-33-14, Quantachrome® Instruments).

The electrical resistance of the stainless steel hollow fiber was measured with a multimeter, Benning M1, at room temperature over a length of 10 cm.

Single gas permeation was measured in a pressure controlled dead-end permeation set-up. Fibers were sealed on one end with Araldite®. The measurements were performed at room temperature and 2 bar pressure difference ($p_{permeate}$ = 1 atm). The single gas permeance F of nitrogen was calculated from the following equation:

$$F = \frac{N}{\Delta p} \tag{4.2}$$

Here N is the molar flux through the membrane and Δp is the trans membrane pressure.

4.3. Results and discussion

Particle loaded spinning mixtures display a shear thinning viscosity that is strongly dependent on the mixtures composition.

Figure 4.1 shows the viscosity of particle loaded spinning mixtures as a function of the concentration of non-solvent, at a fixed shear rate (1.5 RPM). Addition of water before or after the addition of polymer (see Table 4.2) did not significantly influence the results. In general a higher viscosity is observed for mixtures with higher particle loading, and for all spinning mixtures the viscosity initially increases with the water concentration. Above a critical water concentration a strong reduction in viscosity is observed, which is associated with phase separation of the mixture. This de-mixing of the mixture into two separate phases is also observed by eye.

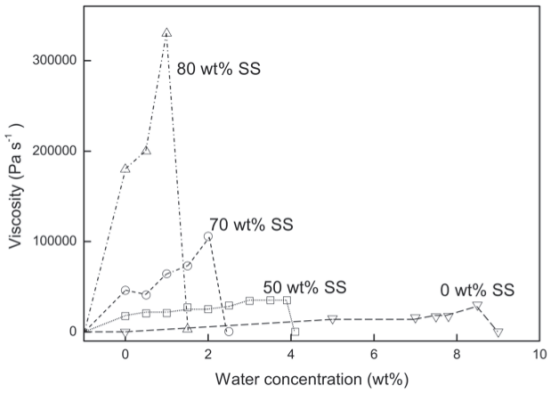

Figure 4.1: Viscosity of spinning mixtures with different loading of stainless steel as function of water concentration steel at fixed shear rate (1.5 RPM), lines are guides to the eye

No effect, of the extent and duration of mixing/stirring on the critical water concentration, has been observed, suggesting that the two phase system corresponds to thermodynamic equilibrium. For a spinning mixture without stainless steel particles we observe phase separation at a water concentration comparable to that found by Lau at al.[13]. At increasing particle loading the amount of water required to induce de-mixing distinctly reduces (3.5 - 3.0 - 1.5 wt% water, for 48 – 70 - 80 wt% particle loading, respectively), indicating that for the mixtures containing more particles the two-phase region in the phase diagram is larger.

In Figure 4.2 SEM micrographs are depicted of cross sections of porous stainless steel hollow fibers, derived from spinning mixtures with different loading of stainless steel particles. Fibers on the left hand side are green compacts, fibers on the right hand side have been sintered at 1100 °C. After thermal treatment, the geometry of the fibers prepared with 48 wt% stainless steel (Figure 4.2b) has significantly changed. Probably there are insufficient particles to preserve the structure during burnout of the polymer. The morphologies of the fibers prepared of spinning mixtures containing 70 wt% and 80 wt% stainless steel are preserved upon sintering, except for shrinkage Figure 2.4d, f). This behavior is analogous to ceramic hollow fibers prepared via phase inversion [14]. The thermal treatment of the fibers was conducted in a nitrogen atmosphere and oxidation problems have not been observed.

Figure 4.2 shows that the loading of stainless steel particles in the spinning mixture has an apparent influence on the morphology of the derived hollow fiber. The cross section of a fiber prepared from a spinning mixture containing 48 wt% stainless steel particles (Table 4.2, exp. 1), depicted in Figure 4.3a, reveals macrovoids (finger like voids) originating from both the inner and outer surface of the fiber. These macrovoids extend almost to the center of the fiber cross section, where a sponge like structure can be seen.

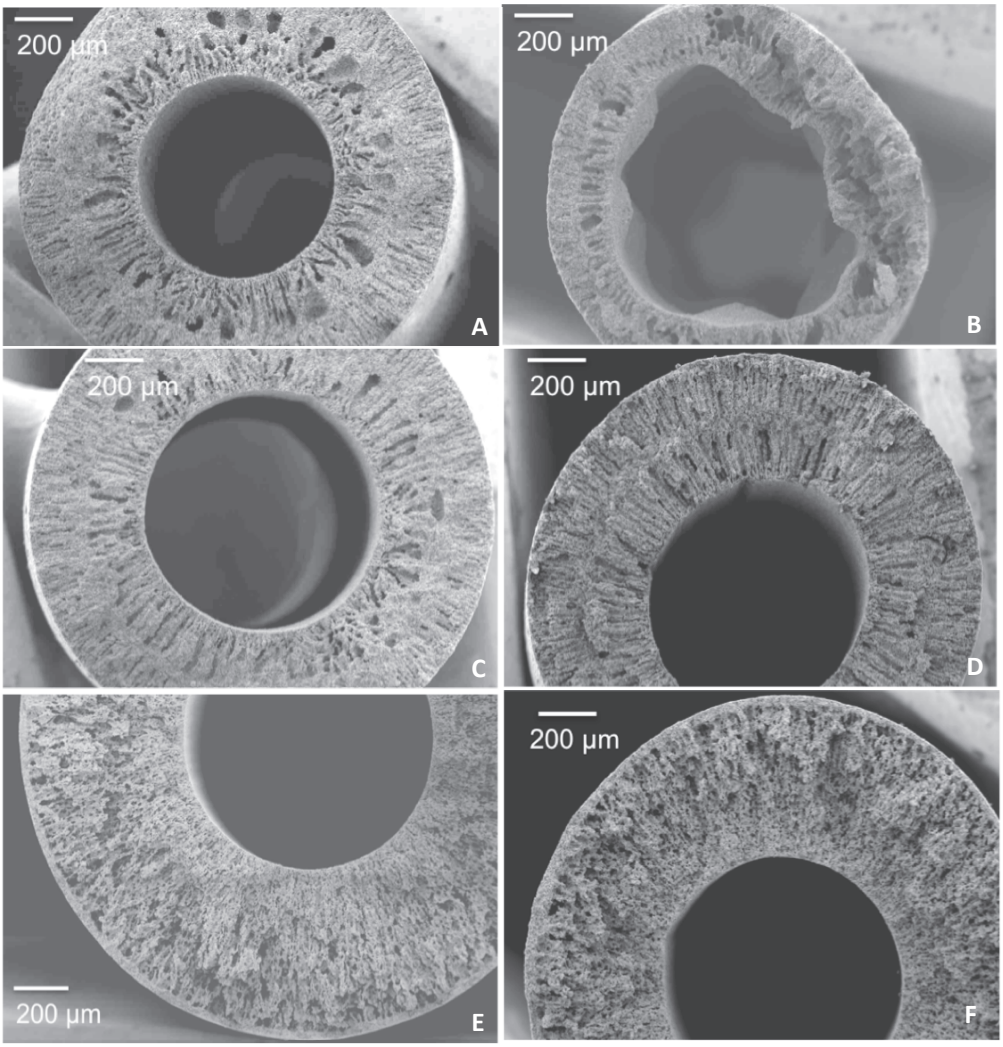

Figure 4.2: SEM images of fibers with 48-70-80 wt% of stainless steel. (a): 48 wt% green compact, (b): 48 wt% sintered 1100 °C, (c): 70 wt% green compact, (d): 70 wt%, sintered 1100 °C (e): 80 wt% green compact, (f): 80 wt% sintered 1100 °C

When the loading of the particles is increased to 70 wt% a decrease in the size of the especially the larger macrovoids is observed (Figure 4.3c, Table 4.1, exp. 2). This difference in morphology is probably related to the reduction in the amount of water required to induce phase separation of a spinning mixture containing more stainless steel particles.

It is well known that for spinning mixtures with a composition closer to the phase boundary more regular (sponge like) structures are obtained, with less and smaller voids [15, 16] .

Increasing the loading to 80 wt% (Table 4.1, exp. 3) results in a sponge like structure at the outer surface of the fiber. This sponge like structure is due to the relatively long residence time of the highly viscous spinning mixture in the air gap, and the consequently more pronounced exposure of the fiber to water vapor [17]. The sponge-like region inhibits growth of macrovoids from the outside of the fiber, while at the same time fast exchange of solvent, and non-solvent from the bore liquid induces long thin macrovoids [14]. The uniform sponge like structure on the outside of the fiber derived from the 80 wt% spinning mixture is beneficial for use as membrane support; however, the high viscosity of the spinning mixture complicates a controlled spinning process. By adding a small amount of non-solvent to the spinning mixture with lower particle loading similar fiber morphology may be achieved, while avoiding a too high viscosity. Accordingly, further experiments were performed with spinning mixtures containing 70 wt% stainless steel particles and 2 w t% water.

Figure 4.3 depicts SEM images of cross sections of resulting fibers. The left hand side image of a green compact (Figure 4.3a), displays a cross section with macrovoids on the inner part of the fiber and a denser sponge like structure at the outer surface of the fiber. The image on the right hand side (Figure 4.3b), of a fiber sintered at 1100 °C, indicates that no significant changes occur in morphology during heat treatment, except for shrinkage. SEM images with higher magnification of the green compact (Figure 4.3c), and of the sintered fiber (Figure 4.3d), confirm this.

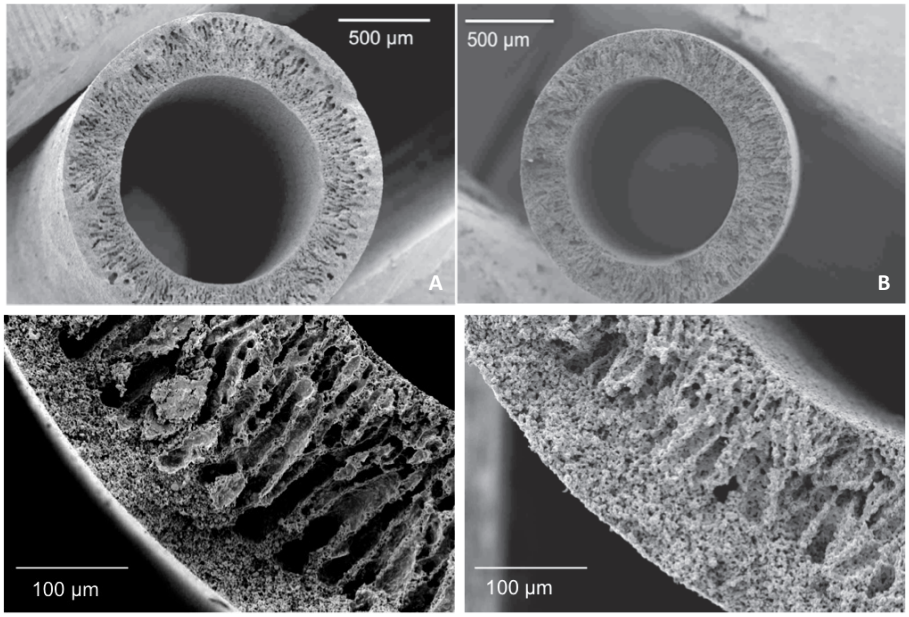

Figure 4.3: SEM image of stainless steel fiber derived from 70 wt% particle loaded spinning mixture with 2 wt% water (a): green compact, (b): sintered at 1100 °C, (c): green compact, higher magnification, (d): sintered at 1100 °C, higher magnification

Figure 4.4 depicts the electrical resistance of the stainless steel hollow fiber as function of the sintering temperature. Initially the electrical resistance decreases with increasing sintering temperature up to 1000 °C, and subsequently stabilizes at a value of 0.03 Ω cm^{-1}. The initial decrease of the electrical resistance is due to burnout of the polymer, which according to TGA analysis (Figure 4.5) is almost complete at a temperature of 600 °C, while necks between the steel particles are starting to form. The stabilization of the electrical resistance at a sintering temperature of 1000 °C indicates that the neck area is sufficient to create a conductive path, and a further increase of the sintering temperature merely results in denser (lower resistance) and thinner fibers (higher resistance). Therefore, the overall effect on electrical resistance is minor.

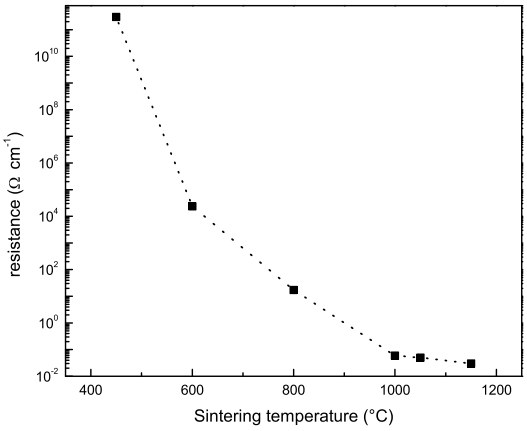

Figure 4.4: Electrical resistance of stainless steel hollow fibers as function of sintering temperature (70 wt% stainless steel and 2 wt% water)

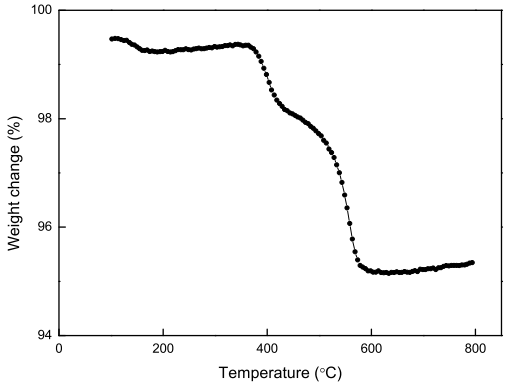

Figure 4.5: TGA graph of a fiber derived from a particle loaded spinning mixture with 70 wt% of stainless steel and 2 wt% water

In contrast to the asymptotic behavior of the electric conductivity at sintering temperatures above 1000 °C, the mechanical strength and gas transport properties of the porous hollow fibers show a strong correlation with sintering temperature in the range of 1000-1200 °C.

Figure 4.6 shows that the bending strength of the stainless steel fibers increases with sintering temperature from 450 MPa at 1050 °C to 3500 MPa at 1200 °C. The bending strength is calculated from an equation that is commonly used for ceramic fibers (Equation 4.1). It should be noted that this equation is not valid for a quantitative analysis of the bending strength of ductile materials, and the high values reported here should be interpreted with caution. However, the large increase suggests significant changes in the microstructure of the fibers with sintering temperature. The ductile nature of the fibers and the large bending strength signify that the stainless steel hollow fibers have superior mechanical properties as compared to their ceramic counterparts.

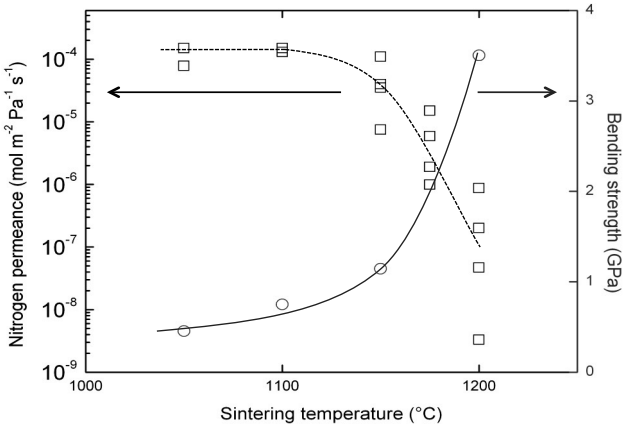

Figure 4.6: Bending strength and nitrogen permeance stainless steel hollow fibers as wt% of stainless steel and 2wt% water.

For comparison, in literature a bending strength of 340 Pa and nitrogen permeance of 2×10^{-6} mol m^{-2} Pa^{-1} s^{-1} have been reported for Al_2O_3 hollow fibers with similar dimensions [18]. For the stainless steel hollow fibers the nitrogen permeance is ~10^{-4} mol $m^{-2}Pa^{-1}$ s^{-1} and does not change significantly

with sintering temperature in the range 1050 - 1100 °C. At these temperatures, changes in the pore size distribution are minor and the pores remain interconnected (see Figure 4.8). A rough estimate of the average pore size, assuming nitrogen transport occurs predominantly by Knudsen diffusion, yields a value in the range 1-3 μm, which is in good agreement with the mean value of 1.4 μm obtained from capillary flow porometry analysis.

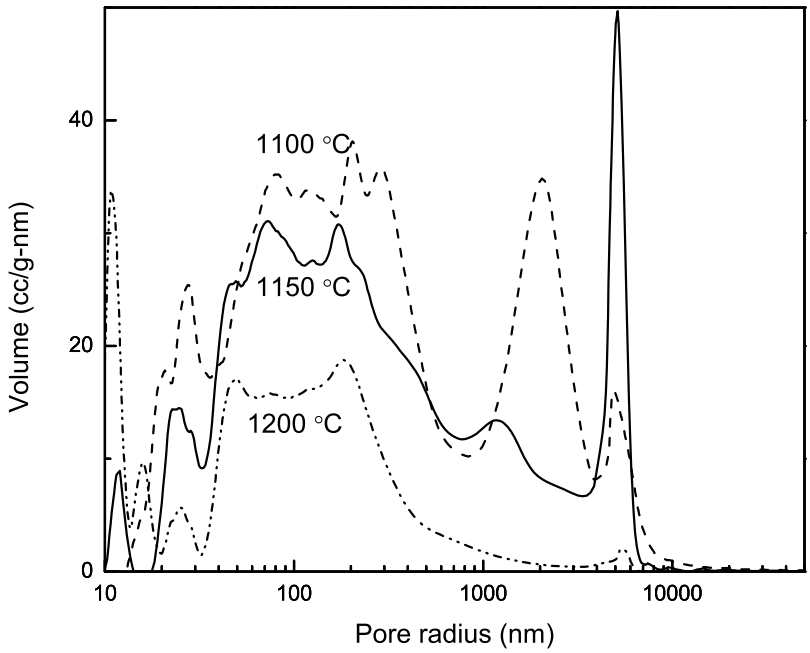

Figure 4.7: Bending strength and nitrogen permeance stainless steel hollow fibers as function of sintering temperature (70 wt% stainless steel and 2 wt% water)

Sintering at temperatures ≥ 1150 °C results in a sharp decrease in gas permeance. The large variation in nitrogen permeance of different fibers sintered in this temperature range is indicative of a densified pore structure that is close to the percolation limit; small changes in such a structure have a pronounced effect on the transport resistance. A more detailed analysis of the evolution of the pore size distribution with sintering temperature,

determined with the mercury porosimetry analyzer, is depicted in Figure 4.8. The fiber sintered at 1100 °C has a pore size distribution with pores in the ranges 0.2 - 0.6 μm and 1 - 10 μm. Sintering at a temperature of 1150 °C results in a lower total volume of the pores in both ranges. A fiber sintered at 1200 °C contains predominantly smaller pores and pores ≥ 1 μm have disappeared. The rise in volume of the pores ~10 nm at 1200 °C indicates a complex evolution of pore size distribution with temperature. The total pore volumes of fibers sintered at different sintering temperatures are shown in Figure 4.9. This total volume (per gram fiber) decreases significantly with increasing sintering temperature due to densification and pore shrinkage. Noteworthy is the large impact of pores ≥ 1 μm on the total pore volume. For the fiber sintered at 1100 °C these pores represent more than 50% of the total pore volume. Sintering at 1150 °C leads to a small reduction in the fractional volume occupied by these pores, whereas after sintering at 1200 °C pores ≥ 1 μm do not contribute significantly to the total pore volume.

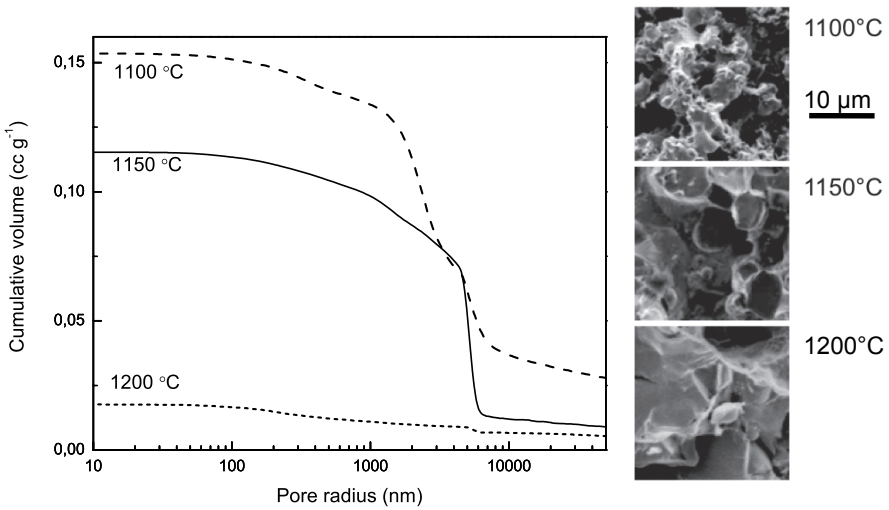

Figure 4.8 Pore size distribution of stainless steel hollow fibers as function of sintering temperature (70 wt% stainless steel and 2 wt% water)

A SEM micrograph of a fiber sintered at 1100 °C (also pictured in Figure 4.9) shows that the fiber consist of connected particles with different sizes.

A fiber sintered at 1150 °C shows a dense packing of larger particles; the smaller particles have disappeared. Sintering at 1200 °C results in a further densification of the microstructure, in which individual particles can no longer be readily identified.

The changes in the microstructure of the stainless steel fibers as a function of sintering temperature, and the related effects on mechanical strength and transport properties, are far more pronounced as compared to ceramic hollow fibers [18]. This is for instance evident from the drop of more than two orders of magnitude in nitrogen permeance for fibers sintered in the range 1150-1200 °C. In addition to the control of fiber morphology during the dry-wet spinning process, for stainless steel fibers the thermal treatment step allows for control of the fibers microstructure and related pore structure.

4.4. Conclusions

Porous stainless steel hollow fibers have been prepared with controlled morphology (macrovoids/sponge like structure) and microstructure (pore size distribution), via the dry-wet spinning process followed by thermal treatment. The morphology of the fibers is predominantly determined during the dry-wet spinning process and can for instance be tuned by controlling the particle loading and the water concentration of the spinning solution. The microstructure is strongly affected by the heat treatment procedure. In this respect, fibers suitable for coating could be prepared with uniform sponge-like structures at the outer surface the fibers. The fibers combine a high strength, 750 - 1150 MPa (sintered at 1050-1100 °C) with a large nitrogen permeance of 1×10^{-4} mol m^{-2} Pa^{-1} s^{-1} at 21 °C. A sharp decrease in nitrogen permeance, and a concurrent increase in bending strength, are observed when the fibers are sintered at temperatures > 1100 °C. This indicates that the microstructure can be controlled, by the sintering temperature, to a far greater extent as compared to ceramic hollow fibers.

References

[1] B. Meng, X. Tan, X. Meng, S. Qiao, S. Liu, Porous and dense Ni hollow fibre membranes, Journal of Alloys and Compounds, 470 (2009) 461-464.

[2] S.-M. Lee, I.-H. Choi, S.-W. Myung, J.-y. Park, I.-C. Kim, W.-N. Kim, K.-H. Lee, Preparation and characterization of nickel hollow fiber membrane, Desalination, 233 (2008) 32-39.

[3] M. Ayturk, I. Mardilovich, E. Engwall, Y. Ma, Synthesis of composite Pd-porous stainless steel (PSS) membranes with a Pd/Ag intermetallic diffusion barrier, Journal of Membrane Science, 285 (2006) 385-394.

[4] K. Rothenberger, A. Cugini, B. Howard, R. Killmeyer, M. Ciocco, B. Morreale, R. Enick, F. Bustamante, I. Mardilovich, Y. Ma, High pressure hydrogen permeance of porous stainless steel coated with a thin palladium film via electroless plating, Journal of Membrane Science, 244 (2004) 55-68.

[5] D. Wang, J. Tong, H. Xu, Y. Matsumura, Preparation of palladium membrane over porous stainless steel tube modified with zirconium oxide, Catalysis Today, 93-95 (2004) 689-693.

[6] C. Kong, J. Lu, J. Yang, J. Wang, Preparation of silicalite-1 membranes on stainless steel supports by a two-stage varying-temperature in situ synthesis, Journal of Membrane Science, 285 (2006) 258-264.

[7] T. Van Gestel, D. Sebold, W.A. Meulenberg, M. Bram, H.-P. Buchkremer, Manufacturing of new nano-structured ceramic-metallic composite microporous membranes consisting of ZrO_2, Al_2O_3, TiO_2 and stainless steel, Solid State Ionics, 179 (2008) 1360-1366.

[8] S. Li, M.A. Carreon, Y. Zhang, H.H. Funke, R.D. Noble, J.L. Falconer, Scale-up of SAPO-34 membranes for CO2/CH4 separation, Journal of Membrane Science, 352 (2010) 7-13.

[9] K. Brands, D. Uhlmann, S. Smart, M. Bram, J.C.D. da Costa, Long-term flue gas exposure effects of silica membranes on porous steel substrate, Journal of Membrane Science, (2010).

[10] A. Brunetti, G. Barbieri, E. Drioli, T. Granato, K.-H. Lee, A porous stainless steel supported silica membrane for WGS reaction in a catalytic membrane reactor, Chemical Engineering Science, 62 (2007) 5621-5626.

[11] S.C. Chen, G.C. Tu, C.C.Y. Hung, C.A. Huang, M.H. Rei, Preparation of palladium membrane by electroplating on AISI 316L porous stainless steel supports and its use for methanol steam reformer, Journal of Membrane Science, 314 (2008) 5-14.

[12] J. De Jong, N.E. Benes, G.H. Koops, M. Wessling, Towards single step production of multi-layer inorganic hollow fibers, Journal of Membrane Science, 239 (2004) 265-269.

[13] W.W.Y. Lau, M.D. Guiver, T. Matsuura, Phase separation in polysulfone/solvent/water and polyethersulfone/solvent/water systems, Journal of Membrane Science, 59 (1991) 219-227.

[14] B. Kingsbury, K. Li, A morphological study of ceramic hollow fibre membranes, Journal of Membrane Science, 328 (2009) 134-140.

[15] M. Mulder, in: Basic Principles of Membrane Technology, Kluwer Academic Publishers, Dordrecht, 1996.

[16] H. Strathmann, The formation mechanism of phase inversion membranes, Desalination, 21 (1977) 241-255.

[17] H.A. Tsai, C.Y. Kuo, J.H. Lin, D.M. Wang, A. Derantani, C. Pochat-Bohatier, K.R. Lee, J.Y. Lai, Morphology control op polysulfone hollow fiber membranes via water vapor induced phase separation, Journal of Membrane Science, 278 (2006) 390-400.

[18] S. Liu, K. Li, R. Hughes, Preparation of porous aluminium oxide (Al_2O_3) hollow fibre membranes by a combined phase-inversion and sintering method, Ceramics International, 29 (2003) 875-881.

Chapter 5:

Porous stainless steel hollow fibers with shrinkage-controlled small radial dimensions

THIS CHAPTER HAS BEEN PUBLISHED:

Mieke W. J. Luiten-Olieman, Michiel J. T. Raaijmakers, Louis Winnubst, Matthias Wessling, Arian Nijmeijer, and Nieck E. Benes, Porous stainless steel hollow fibers with shrinkage-controlled small radial dimensions, Scripta Materialia, 65 (2011) 25-28.

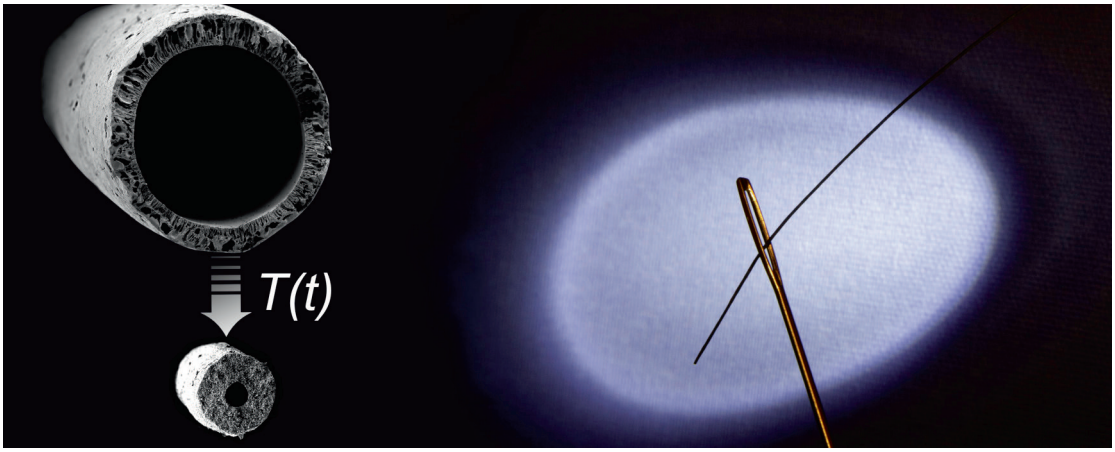
T(t)

Abstract

A method is presented for the preparation of thin (~250 μm) porous stainless steel hollow fiber membranes based on dry-wet spinning of a particle-loaded polymer solution followed by heat treatment. Extraordinary small radial dimensions were achieved by controlled shrinkage during thermal treatment. Above the glass transition temperature of the polymer, the dynamics of surface energy-driven viscous flow allow regulated reduction of the macrovoid volume, resulting in a substantial decrease in the final fiber diameter.

5.1 Introduction

Hollow fiber membranes with small radial dimensions allow a very high surface-area-to-volume ratio, up to ~10^4 m^{-1}, and can sustain large hydrostatic pressures. Polymeric hollow fiber membranes, prepared via the dry-wet spinning, are widely used in various biomedical, medical and industrial applications [1, 2]. Inorganic membranes can offer an interesting alternative for applications in which polymers have limited chemical or thermal stability. Currently, no commercial inorganic hollow fiber membranes exist. In the scientific literature, there are reports of porous ceramic hollow fibers that have been made via dry-wet spinning of a polymer solution containing inorganic particles, followed by heat treatment to burn out the polymer and sinter the particles together [3-8]. The applicability of these fibers is hampered by their limited mechanical strength.

Here, we present a method that allows the preparation of stainless steel hollow fibers with an outer diameter that can be regulated down to ~250 μm, comparable to that of typical polymeric hemodialysis and gas separation membranes [2]. The extraordinarily small radial dimensions are achieved by controlled shrinkage of the green fibers at temperatures exceeding the glass transition temperature. At these temperatures, the dynamics of viscous deformation of the green fibers allow regulated reduction of the macrovoid volume and a substantial decrease in the final fiber diameter. The pronounced changes in fiber morphology upon heat treatment are in contrast to observations reported for other inorganic hollow fiber membranes.

5.2 Experimental

Green hollow fibers were prepared via the dry-wet spinning process based on the principle of phase separation; this process has been described in detail elsewhere [9]. Spinning experiments were performed with a spinneret with inner and outer diameters of 0.5 and 1.1 mm, respectively. De-ionized water was used as the non-solvent in the coagulation bath and as the bore liquid. Spinning mixtures were made by adding stainless steel powder (316L, particle size 4.17 μm according to the manufacturer, Epson Atmix Corporation) to N-methylpyrrolidone (NMP, 99.5 wt%, Aldrich), followed by stirring for 30 minutes. Polyethersulfone (PES, 6020P,

Ultrason) was added in was added in three steps each separated by 2 hours, and the mixture was then stirred for 16 h. The PES/NMP volume ratio was kept constant (1/4), while the concentration of stainless steel was varied in the range of 23 - 62 vol% (with respect to stainless steel+PES, not including the solvent; this definition of the vol% stainless steel relates to the composition of the green fiber and is used throughout the remainder of this work). If necessary, 0 - 1.2 vol% polyvinylpyrrolidone (PVP, K95, Aldrich) was added to regulate viscosity, followed by stirring for 16 hours. The spinning mixtures were degassed before spinning by applying a vacuum for 30 minutes and leaving the mixtures for 16 hours in dry air. The stainless steel powder and PES were dried before use; all other chemicals were used without further treatment. Directly after spinning, the hollow fibers were kept in a water bath for 24 hours day to remove all traces of NMP, followed by drying and stretching (0.5 cm per m) for 24 hours.

The thermal treatment of the fibers involved six sequential steps: the fibers were heated to 200 °C (5 °C min^{-1}), 300 °C (1 °C min^{-1}), 400 °C (5 °C min^{-1}), 600 °C (1 °C min^{-1}), and 1100 °C (5 °C min^{-1}, 30 min dwell) and subsequently cooled to ambient temperature (5 °C min^{-1}). The changes in morphology in the range of 200 - 300 °C were analyzed by heating the fiber to a specified temperature (5 °C min^{-1}), keeping the fiber at this temperature for a specified period, and subsequently cooling it to ambient temperature (10 °C min^{-1}).

5.3 Results and discussion

Three porous stainless steel hollow fibers and 2 commercial membranes, for comparison, are depicted in Figure 5.1. The variation in diameter of the steel fibers is indicative of the range of radial dimensions that can be covered using a single spinneret with fixed dimensions. The only difference in the preparation of the three fibers is the vol% loading of stainless steel. Prior to heat treatment, the diameters of the fibers were approximately equal (~850 μm). The dimensional changes became apparent after heat treatment, during which the fibers showed a distinct shrinkage. The extent of the shrinkage was larger when the green fiber contained a lower loading of steel particles.

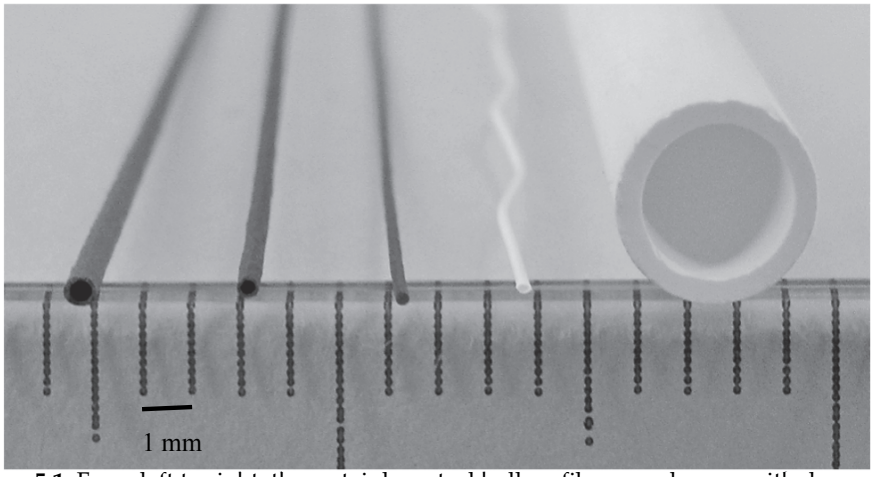

Figure 5.1: From left to right, three stainless steel hollow fiber membranes with decreasing outer diameters (750,460, and 285 μm); for comparison, a polymeric (hemodialysis) hollow fiber (060509, Fresenius) and an alumina capillary (M20, Hyflux)

The most pronounced change in diameter was observed with a particle loading of 23 vol%, where the fiber diameter was reduced to only 34 % of the initial value. This thin stainless steel hollow fiber had a diameter similar to that of the polymeric fiber and was 13 times thinner than the alumina capillary. In other studies dealing with inorganic fibers, the observed moderate shrinkage during heat treatment was ascribed to densification and the burnout of the polymer [3-5, 10, 11]. The reductions in diameter reported here are far more pronounced, and volume balance calculations confirmed that polymer burnout alone cannot account for the dimensional changes. Additionally, alterations in fiber morphology likely contribute to the extensive shrinkage.

A series of representative SEM images were selected to illustrate the changes in fiber morphology during heat treatment (see Figure 5.2). The fibers on the left are green compacts, whereas those on the right were sintered at 1100 °C. For the fiber with the highest loading of stainless steel particles (Figure 5.2-a/b, 62 vol%), the morphology was more or less preserved upon sintering, except for some shrinkage.

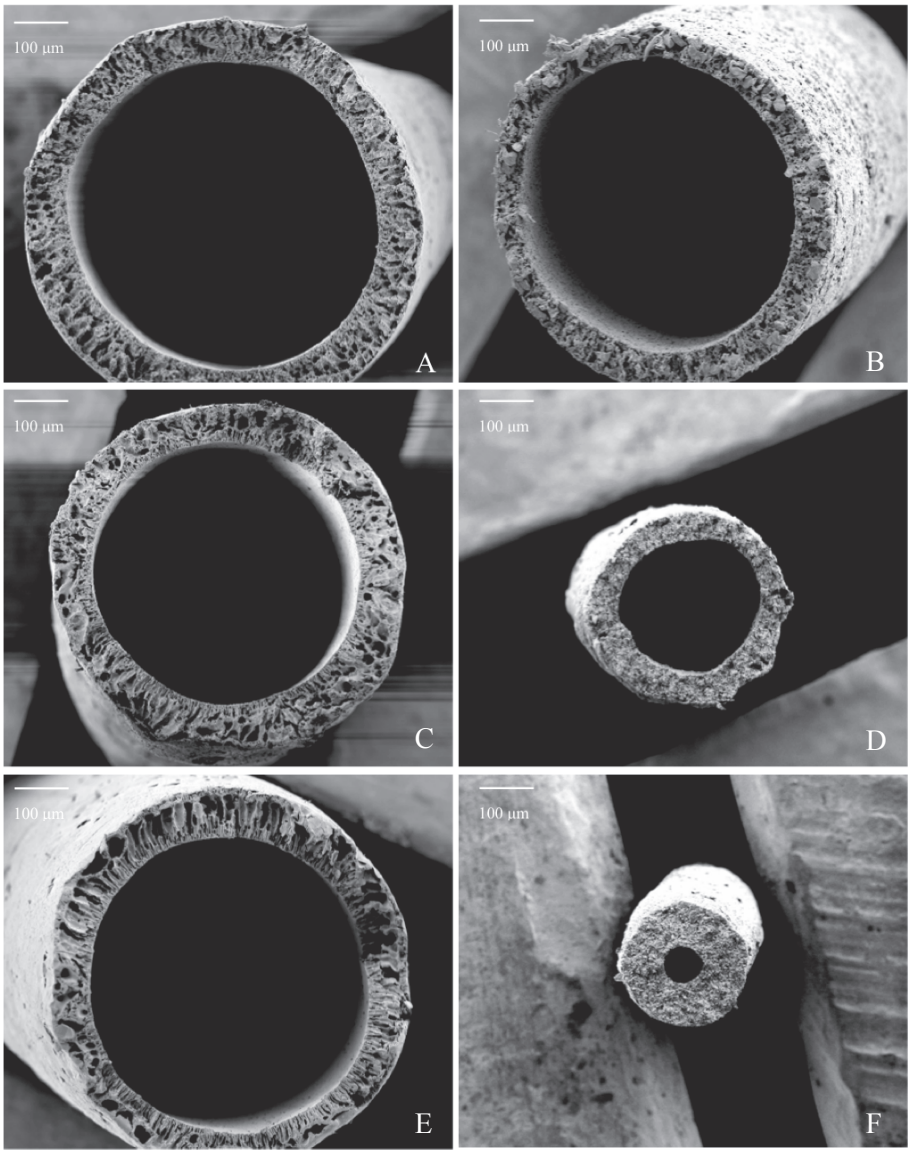

Figure 5.2: SEM images of hollow fibers with 62, 41, and 23 vol% stainless steel. Left, green compacts: (a) 62 vol%, (c) 41 vol%, and (e) 23 vol%; right, fibers sintered at 1100 °C: (b) 62 vol%, (d) 41 vol%, and (f) 23 vol%

After sintering, macrovoids were still present in this fiber, similar to what has been observed by others for inorganic hollow fibers with larger diameters [4, 5, 7, 8, 12, 13]. In contrast, a significant change in the morphology was observed after the sintering of fibers with lower loadings of stainless steel, 41 vol% (Figure 5.2-c/d) and 23 vol% (Figure 5.2e/f). Prior to sintering, these fibers possessed distinct macrovoids, but after sintering, these macrovoids disappeared, and a major decrease in outer diameter was observed.

The evolution of fiber length as a function of temperature is depicted in Figure 5.3. The data clearly show that a predominant part of the shrinkage occurs in the temperature range of 200 - 300 °C. This temperature range includes the glass transition temperature of polyethersulfone (T_g = 225 °C), above which the polymer changes from a glassy to a rubbery material and the mechanical and physical properties change markedly. In particular, the viscoelastic properties of the thermoplastic will vary strongly in this temperature range.

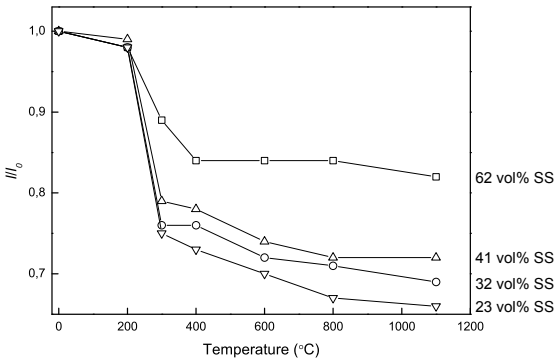

Figure 5.3: Evolution of fiber length l with temperature for different vol% stainless steel, normalized with respect to the initial length, l_0

A sufficiently low viscosity of the green fiber can allow for viscous sintering, i.e., surface tension-driven flow under the influence of surface curvature gradients. During viscous sintering, the macrovoid volume in the fibers is reduced, causing a substantial shrinkage of the fiber, as observed

for the fibers with loadings of 23, 32, and 41 vol%. When the particle loading is too high, the viscoelastic properties of the green fibers are dictated by the particles rather than by the polymer, and viscous deformation is obstructed. This finding explains the moderate shrinkage of the fiber with 62 vol% stainless steel.

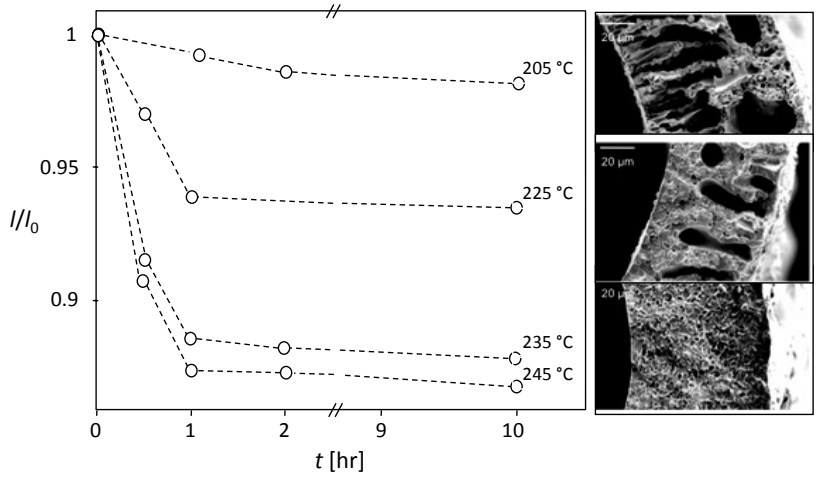

Figure 5.4: 41 vol% stainless steel. Left: normalized fiber length as function of time at different temperatures. Right: SEM micrographs of fibers incubated for 10 hours at 205, 225, and 245 °C

The viscous deformation is driven by a reduction in the surface free energy associated with the macrovoids, and the shape and size of these macrovoids are expected to have an influence on the rate of macrovoid decay [14]. This effect is illustrated in Figure 5.4, where the normalized length of the fibers is plotted against time, while the fiber is held at a specified temperature. The data showed that a reduction in length occurred in the first few hours, and the corresponding rate at which the fiber shrank increased with temperature. This result was expected based on the characteristic time for viscous sintering introduced by Kuiken [14], $t_c=l\eta/\sigma$ (where σ is the surface tension and l is the characteristic length) because the dynamic viscosity η decreases with increasing temperature. Within the timescale of the experiment, for each specified temperature, the extent of shrinkage reached an asymptotic value. At lower temperatures, macrovoids disappear only if they are small, whereas for the larger macrovoids, the surface energy driving force is insufficient to overcome the

viscous forces. With increasing temperature, viscosity decreases, and the decay of larger voids becomes apparent. This behavior was substantiated by the SEM images of fiber cross-sections on the right hand side of Figure 5.4. For the fiber incubated at 205 °C, small macrovoids can be identified. After incubation at 225 °C, small macrovoids were no longer visible, but larger macrovoids were still present. The fiber incubated at 245 °C did not exhibit any apparent macrovoids.

Gas permeance was measured, at 21 °C, as a function of pressure difference, up to 7 bar, using a pressure-controlled dead-end gas permeation set-up up. Stainless steel hollow fibers (41 vol%), sintered at 1100 °C, exhibit a nitrogen permeance of $4 \pm 1 \times 10^{-6}$ mol m^{-2} Pa^{-1} s^{-1}.

5.4 Conclusions

A method was presented for the preparation of porous stainless steel hollow fibers with regulated small radial dimensions by combining a well-established method for the preparation of polymeric hollow fibers with sensible thermal treatment. At ambient temperatures, the morphology of the green fibers, e.g., the degree of macrovoids, can be influenced via the spinning parameters. At temperatures around the glass transition temperature, the shrinkage of the fibers can be controlled; macrovoids with small sizes disappear at lower temperatures, whereas larger macrovoids persist up to higher temperatures. At elevated temperatures (>1000 °C), the pore size distribution of the fibers can be regulated [15]. The method presented here is versatile and generic in nature. Substitution of stainless steel with other particles of different size, shape, and composition will allow the manufacturing of a broad variety of thin porous inorganic hollow fibers.

References

[1] R.W. Baker, Membrane technology and applications, second ed., McGraw-Hill, Chichester, 2004.

[2] I. Moch, Hollow-Fiber Membranes, Kirk-Othmer Encyclopedia of Chemical Technology, in: Kirk-Othmer Encyclopedia of Chemical Technology, Wiley, 2005.

[3] J. De Jong, N.E. Benes, G.H. Koops, M. Wessling, Towards single step production of multi-layer inorganic hollow fibers, Journal of Membrane Science, 239 (2004) 265-269.

[4] B. Kingsbury, K. Li, A morphological study of ceramic hollow fibre membranes, Journal of Membrane Science, 328 (2009) 134-140.

[5] S. Liu, K. Li, R. Hughes, Preparation of porous aluminium oxide (Al_2O_3) hollow fibre membranes by a combined phase-inversion and sintering method, Ceramics International, 29 (2003) 875-881.

[6] T. Van Gestel, D. Sebold, W.A. Meulenberg, M. Bram, H.-P. Buchkremer, Manufacturing of new nano-structured ceramic-metallic composite microporous membranes consisting of ZrO_2, Al_2O_3, TiO_2 and stainless steel, Solid State Ionics, 179 (2008) 1360-1366.

[7] B. Meng, X. Tan, X. Meng, S. Qiao, S. Liu, Porous and dense Ni hollow fibre membranes, Journal of Alloys and Compounds, 470 (2009) 461-464.

[8] S.-M. Lee, I.-H. Choi, S.-W. Myung, J.-y. Park, I.-C. Kim, W.-N. Kim, K.-H. Lee, Preparation and characterization of nickel hollow fiber membrane, Desalination, 233 (2008) 32-39.

[9] M. Luiten-Olieman, L. Winnubst, A. Nijmeijer, M. Wessling, N. Benes, Porous stainless steel hollow fiber membranes via dry-wet spinning, Journal of Membrane Science, 370 (2011)124-130.

[10] S. Liu, K. Li, Preparation TiO2/Al2O3 composite hollow fibre membranes, Journal of Membrane Science, 218 (2003) 269-277.

[11] X. tan, S. liu, K. Li, Preparation and characterisation of inorganic hollow fiber membranes, Journal of Membrane Science, 188 (2001) 7.

[12] N. Droushiotis, U. Doraswami, K. Kanawka, G.H. Kelsall, K. Li, Characterization of NiO–yttria stabilised zirconia (YSZ) hollow fibres for use as SOFC anodes, Solid State Ionics, 180 (2030) 1091-1099.

[13] N. Yang, X. Tan, Z. Ma, A phase inversion/sintering process to fabricate nickel/yttria-stabilized zirconia hollow fibers as the anode

support for micro-tubular solid oxide fuel cells, Journal of Power Sources, 183 (2008) 14-19.

[14] H.K. Kuiken, Viscous sintering : the surface-tension-driven flow of a liquid form under the influence of curvature gradients at its surface Journal of Fluid Mechanics, 214 (1990) 503-515.

[15] M.W.J. Luiten-Olieman, L. Winnubst, M. Wessling, A. Nijmeijer, N.E. Benes, Porous stainless steel hollow fiber membranes via dry-wet spinning, Journal of Membrane Science, (2011).

Chapter 6:
Generic method for inorganic porous hollow fibers preparation with shrinkage-controlled small radial dimensions

THIS CHAPTER HAS BEEN SUBMITTED:
Mieke W. J. Luiten-Olieman, Michiel J. T. Raaijmakers, Louis Winnubst, Ton C. Bor, Matthias Wessling, Arian Nijmeijer, and Nieck E. Benes, Generic method for inorganic porous hollow fibers preparation with shrinkage-controlled small radial dimensions, applied to Al_2O_3, Ni, SiC, stainless steel, and YSZ, Journal of Membrane Science.

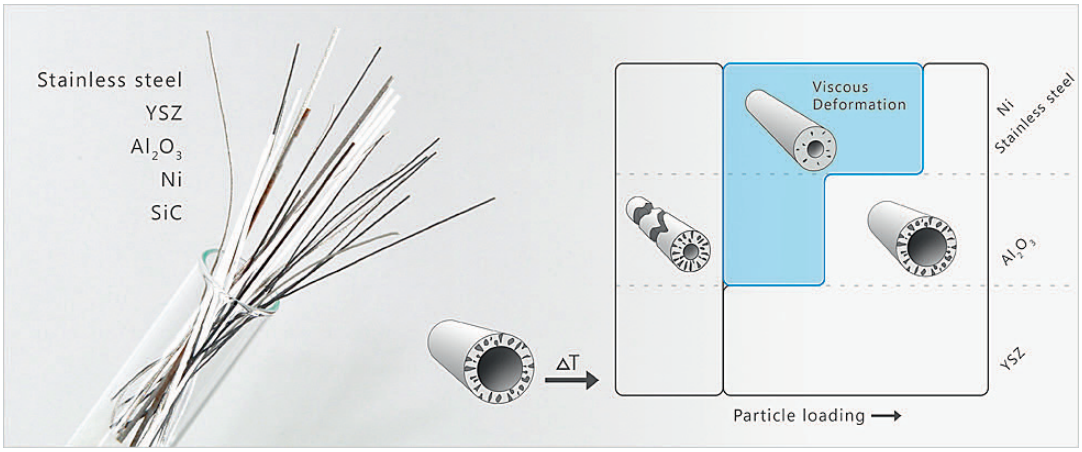
Stainless steel
YSZ
Al_2O_3
Ni
SiC
ΔT
Viscous Deformation
Ni
Stainless steel
Al_2O_3
YSZ
Particle loading

Abstract

A generic and versatile method is presented for the preparation of porous inorganic hollow fibers with small tunable radial dimensions, down to ~250 μm outer diameter. The approach allows fabrication of thin hollow fibers of various materials, as is demonstrated for Al_2O_3, nickel, silicon carbide, stainless steel, and yttria stabilized zirconia. The preparation method is based on dry-wet spinning of a particle-loaded polymer solution followed by thermal treatment. Exceptionally small radial dimensions have been achieved by surface energy driven viscous flow of the green fiber, resulting in a reduction of macrovoid volume. It is shown that the extent of viscous deformation is directly related to the rheology of the particle-loaded green fiber above the glass transition temperature of the polymer. A particle specific limited concentration range can be identified in which viscous deformation is possible. Above a critical particle volume fraction the viscosity of the particle-polymer material increases sharply and the time scale of viscous deformation becomes too long. Below a minimum concentration of particles it is not possible to sinter the particles together. For small particles of Al_2O_3, silicon carbide, and yttria stabilized zirconia the concentration range allowing viscous deformation is very narrow as compared to that of larger metal particles.

6.1 Introduction

In Chapter 5 we have demonstrated that the diameter of stainless steel hollow fibers can readily be tuned to smaller values, down to ~250 μm. The strategy to achieve such small stainless steel fibers is depicted in Figure 6.1, and comprises four different steps.

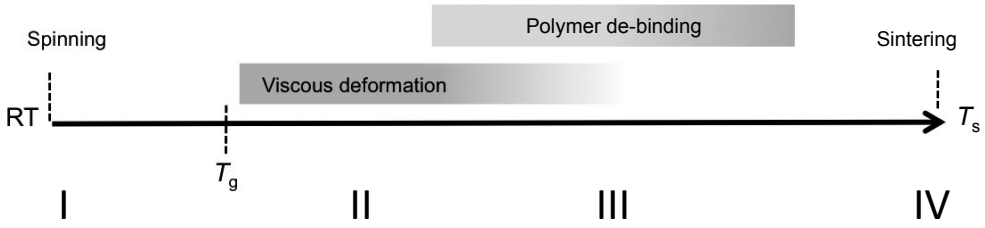

Figure 6.1: Schematic representation of the preparation of inorganic porous hollow fibers

Step I is the dry-wet spinning process. Here a particle loaded polymer solution is pressed through a spinneret and coagulated in a non-solvent bath. Exchange of non-solvent and solvent leads to thermodynamic instability of the spinning mixture and induces phase separation into a polymer lean and a polymer rich phase. The polymer rich phase solidifies, concurrently entrapping the inorganic particles. The morphology of the fiber (prior to heat treatment referred to as 'green fiber') generally exhibits a porous sponge-like structure containing macrovoids. The amount and size of the macrovoids can, for instance, be influenced by varying the viscosity of the spinning mixture, by adding non-solvent to the spinning mixture, by changing the concentration inorganic particles, or by another selection of solvent/non-solvent/polymer combination. In contrast to the majority of other studies, we aim at the presence of a relatively high amount of small macrovoids that are to be removed in step II of the fiber preparation.

In step II the fiber is heated to a temperature above the T_g of the amorphous polymer. Here the dynamics of surface energy driven viscous polymer flow can allow regulated reduction of macrovoid volume, resulting in a substantial decrease in the diameter and the final length of the fiber. The extent of viscous deformation is strongly related to the

rheology of the particle loaded polymer, and hence to the concentration and nature of the inorganic particles. This will be discussed in more detail in the Results and Discussion section.

Step III involves the removal of the polymer and the consolidation of the structure. To maintain structural integrity it is preferential that the polymer de-binding occurs gradually. The polymer should also not persist to too high temperatures, in order to avoid negative effects on sintering or a too high carbon content in the final fiber. The de-binding process can be influenced by the selection of the polymer and the atmosphere in which the de-binding occurs (oxidative, inert, reducing).

Step IV concerns the final consolidation of the structure by sintering. This step affects in particular the porosity, pore size, and mechanical properties of the final membrane. Sintering at too high temperatures can result in almost dense materials while sintering at a too low temperature influences the strength of the hollow fibers negatively.

In this study we demonstrate that our strategy is not limited to stainless steel particles, but in principle allows a generic cost effective fabrication method of other thin inorganic hollow fiber membranes. In particular, the effect of the nature of the inorganic particles on the viscous deformation particle loaded polymer hollow fiber is investigated.

6.2. Experimental

6.2.1 Materials

Nickel (Ni, particle size of 9 μm) and stainless steel powder (316L, particle size of 4.1 μm) were purchased from Epson Atmix Corporation (Japan). AKP 30 α-Al_2O_3 (Al_2O_3, particle size of 0.3 μm) was purchased from Sumitomo Chemicals Co LTD (Japan), silicon carbide (SiC, particle size between 0.5-0.7 μm) from Hongwu Nanometer (China), and an yttria (0.3 mol%) stabilized zirconia (YSZ, particle size of 0.02 μm) powder from Tosoh Corporation (Japan). The manufacturers reported the above-mentioned particle sizes. Polyethersulfone (PES, Ultrason, 6020P, BASF, Germany) was used as polymer and N-methylpyrrolidone (NMP, 99,5wt%, Aldrich, The Netherlands) as solvent. De-ionized water was used as non-

solvent and polyvinylpyrrolidone (PVP K95, Aldrich, The Netherlands) as viscosity enhancer. PES, nickel, α-Al_2O_3, YSZ, and stainless steel powder were dried before use; all other chemicals were used without further pre-treatment. A two-component epoxy resin (Araldite , Viba, The Netherlands) was used for potting the fibers in a module.

6.2.2 Spinning process

Green fibers were prepared via dry-wet spinning process based on the principle of phase separation of a particle loaded polymer solution; this process was described in detail in the previous chapter. Details of the spinning conditions are mentioned in Table 6.1.

Condition	Value
Composition spinning mixture	see Table 6.2
Bore liquid	H_2O
External coagulant	H_2O
Mixture extrusion pressure (bar)	2
Air gap (cm)	3
Bore liquid flow rate (ml/min)	7
Spinneret diameter (mm)	OD/ID=1.1/0.5
Temperature (°C)	21
Relative humidity (%)	40

Table 6.1: Spinning conditions

Spinning mixtures were prepared by adding the inorganic powder (see Table 6.2) to NMP, followed by stirring for 30 min. To decrease the amount of agglomerates, ultrasonic treatment was applied for the preparation of YSZ and Al_2O_3 fibers for 15 min and 45 min, respectively. PES was added in three steps, each separated by 2 h, and the mixture was then stirred for 16 h. The spinning mixtures were degassed by applying vacuum for 30 min and left under dry air for 16 h. The ratio NMP/PES was kept constant (3/1) while the concentration of inorganic powder was varied between 11- 62 vol.% (with respect to inorganic powder + PES, not including the solvent or PVP; this definition of the vol.% inorganic powder relates to the composition of the green fiber and is used throughout the remainder of this work).

Experiment	Material	Concentration particles in HF (vol%)	Particle size (μm)	Spinning mixture NMP (wt%)	PES (wt%)	Particl (wt%)	PVP (wt%)	Viscosity (Pa s^{-1})
1	Al_2O_3	58	0.3	37.5	12.5	50.0	-	38.3
2	Al_2O_3	47	0.3	45.5	15.2	39.3	0.3	44.9
3	Al_2O_3	41	0.3	49.6	16.5	33.4	0.5	43.2
4	Al_2O_3	23	0.3	60.6	20.2	17.6	1.7	44.7
5	Al_2O_3	11	0.3	68.4	22.1	8.0	1.5	27.9
6	Ni	60	9.2	21.8	7.3	70.0	-	38.2
7	Ni	41	9.2	34.8	11.6	52.6	1.0	66.9
8	Ni	23	9.2	50.0	16.7	32.3	1.0	35.2
9	SS	62	4.1	22.5	7.5	70.0	-	51.2
10	SS	41	4.1	74.9	12.4	49.8	0.5	46.2
11	SS	23	4.1	52.5	17.5	30.0	1.0	41.9
12	YSZ	48	0.05	37.5	12.5	50	-	35.8
13	YSZ	23	0.05	56.53	18.83	24.63	1.7	109.0
14	SiC	23	0.5-0.7	63.2	21.1	14.7	1	41.2

Table 6.2: Composition of spinning mixtures of the performed experiment

6.2.3 Drying and thermal treatment

Directly after spinning the hollow fibers were kept in a water bath for 24 hours for completion of the phase separation process, followed by drying and stretching (0.005 m m^{-1}) for 24 hours to straighten the fiber. The fibers (15 cm length) were placed into the channels (4 mm) of a multichannel ceramic, subsequently placed horizontally in a furnace with a controlled atmosphere. Different types of fibers require other thermal treatments, a detailed program of the thermal treatment can be found in Table 3. For the Ni fiber the gas atmosphere was changed to N_2 with 4% H_2 after 120 min at 450 °C.

6.2.4 Characterization

SEM images were taken of the cross sections of the fibers (JEOL JSM 5600LV, at 5 and 15 kV). Before fracturing, the fibers were immersed in liquid nitrogen to obtain a well-defined cross-section.

The rheology was measured using two techniques: room temperature (20 ± 1 °C) experiments were carried out with a Brookfield viscometer (DV-II$^+$ Pro, LV4-64), experiments above the T_g of the polymer, in the range 250 – 300 °C, were carried out with a plate-plate rheometer (Anton Paar Physica MCR 501). For the measurements with the plate-plate rheometer, flat samples were prepared by casting a particle loaded PES-NMP mixture on a glass plate, followed by coagulation in a water bath. Samples were dried (24 h, at 21 °C followed by 12 h at 60 °C) and uni-axially compressed at 100 kN for 1 min to obtain flat samples. Samples of 25 mm were cut out using a stamping press.

Single gas permeation experiments were carried out with a pressure controlled dead-end gas permeation set-up using nitrogen as gas. The feed was introduced on the inside and the permeate was removed from the outside of the fiber. Measurements were performed at room temperature. Fibers were potted in a module and closed on one side with Araldite®.

The pore size distribution was measured with capillary flow porometry, based on the principle of the liquid extrusion porometry technique (Porolux 1000, IB-FT GmbH.)

HF	Shrinkage		De-binding polymer		Sintering		Atmosphere
SS	300 °C (5 °C min^{-1})	60 min	550 °C (1° C min^{-1})	1 min	1100 °C (5 °C min^{-1})	30 min	N_2
Al_2O_3	300 °C (5 °C min^{-1})	60 min	1000 °C (2° C min^{-1})	1 min	1500 °C (5 °C min^{-1})	300 min	Air
Ni	300 °C (5 °C min^{-1})	60 min	450 °C (3° C min^{-1})	2 h	800 °C (5 °C min^{-1})	600 min	Air, > 450 °C N_2

Table 3: Sintering conditions

Light microsope images were made on a Leica M125 stereomicroscope (Germany).

The carbon content was measured with an Elemental Analyzer (Flash 2000 CHNS, Thermo Fischer Science Inc).

6.3 Results and discussion

Figure 6.2 depicts sintered porous hollow fibers consisting of stainless steel, Al_2O_3, Ni, YSZ, and SiC. On the right side a commercial Al_2O_3 capillary (M20, Hyflux®) is displayed for comparison. All fibers have been prepared using the same polymer, solvent, non-solvent, and spinneret with fixed dimensions. The main differences are the concentration and type of inorganic particles added to the spinning solution.

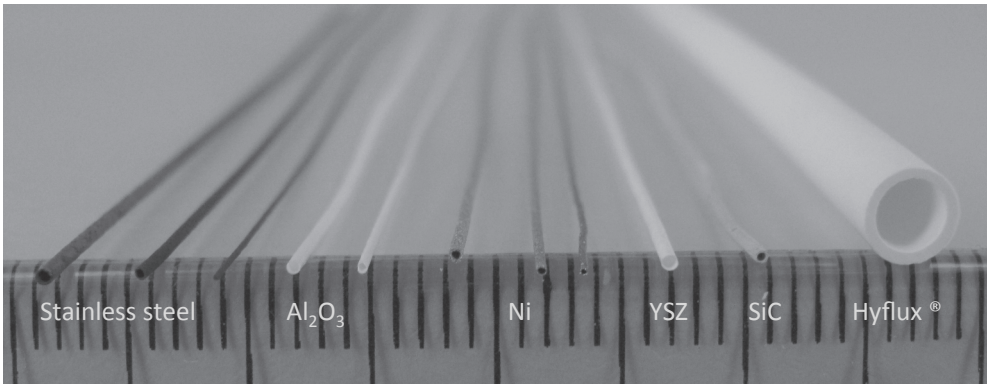

Figure 6.2: From left to right three stainless steel, two Al_2O_3, three Ni hollow fibers, a YSZ, a SiC hollow fiber, and an Al_2O_3 capillary (M 20, Hyflux)

The three porous stainless steel hollow fibers in Figure 6.2 have a diameter between 280 and 750 μm. As described in our previous chapter, the exceptionally small achievable radial dimensions of these fibers (compared to others [1-13],)result from extensive surface energy driven viscous polymer flow at temperatures exceeding the glass transition temperature of the polymer (T_g = 225 °C). This viscous phenomenon results in removal of macrovoids and consequent shrinkage, it is most pronounced for low particle loadings. The Al_2O_3 and Ni fibers depicted in Figure 6.2 display a similar broad range of radial dimensions, indicating that surface energy

driven viscous deformation is not limited to stainless steel particle loaded polymers, but can also be observed for ceramic particles. However, for YSZ comparable extensive shrinkage has not been observed at comparable particle loadings, indicating that the nature of the particles has an effect on the viscous deformation.

A series of representative SEM images of Al_2O_3, Ni, SiC, YSZ, and stainless steel hollow fibers (23 vol.%) is selected to illustrate the changes in the morphology before and after incubation for 10 hours at 300 °C, i.e., above the T_g of the polymer (see Figure 6.3). All images on the left depict green fibers, displaying a distinct morphology containing macrovoids. The green fibers have comparable dimensions and macrovoid volume (~25%). The fibers on the right hand side of Figure 6.3 are obtained after incubation. Except for YSZ, the images reveal significant changes in morphology of the fibers upon incubation; the macrovoids have disappeared and a substantial reduction in outer diameter is observed. This indicates that for fibers, with a particle concentration of 23 vol.%, the loading is sufficiently low to allow the viscous deformation. In contrast, the macrovoids in the YSZ fibers are not completely removed after incubation of 10 h, indicating that even at low particle concentration viscous deformation is sensitive for differences in type and sizes of the particles. The influence of the nature of the particles becomes more pronounced at higher loadings.

Figure 6.4 depicts the length of incubated fibers normalized with respect to the original length of the green fiber (l/l_0), as function of the particle loading. The fiber length is practically more readily accessible than the radial dimensions. The change length represents a direct measure for the extent of shrinkage in a single dimension; it less pronounced as compared to a change in radius that corresponds to shrinkage in two dimensions. At low particle loading (23 vol.%) the reduction in fiber length is comparable for the three different materials; around 26%. When the particle concentration is 41 vol% the reduction in length of the fiber containing Al_2O_3 is less pronounced, as compared to the other fibers.

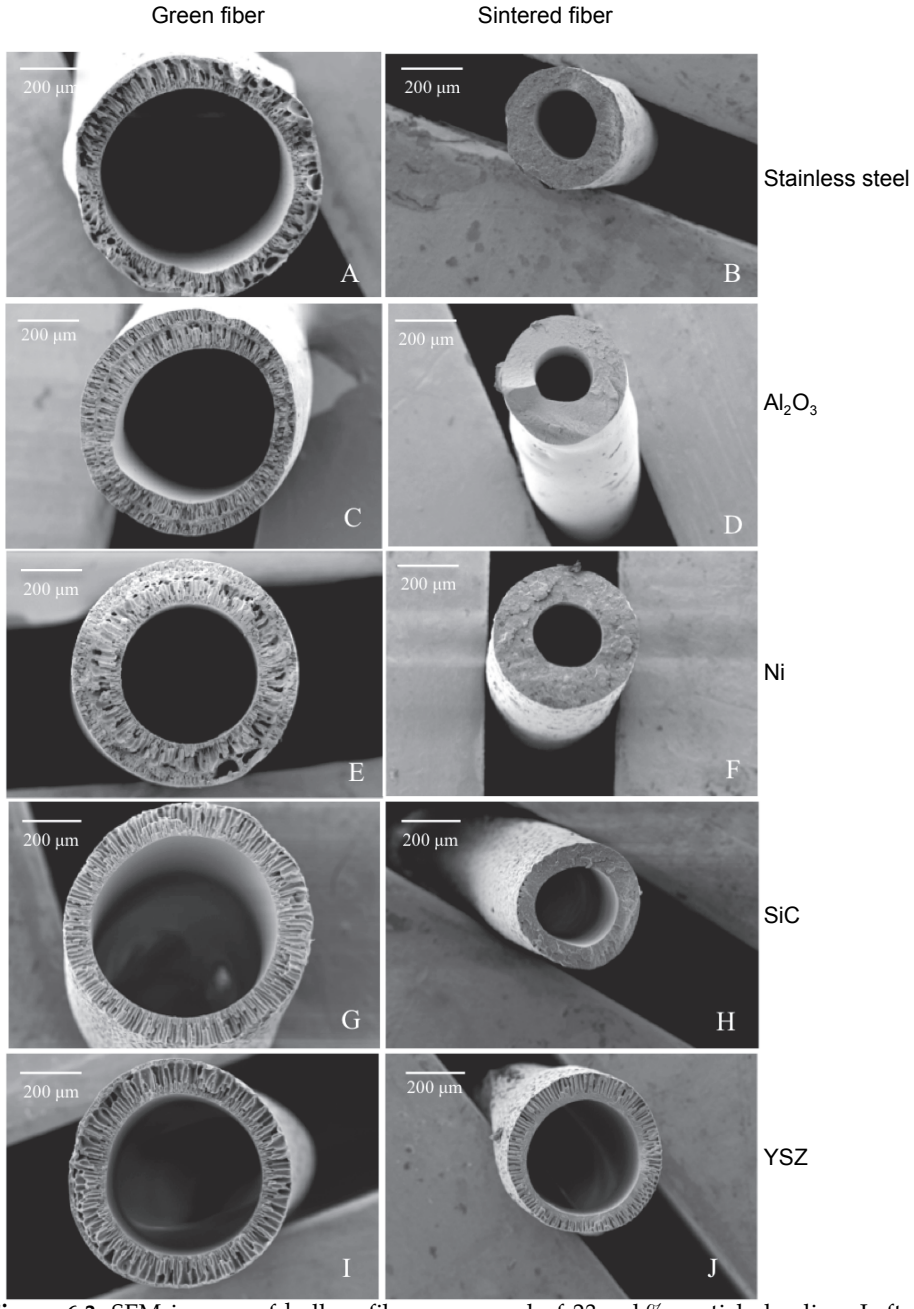

Figure 6.3: SEM images of hollow fibers prepared of 23 vol.% particle loading. Left green compacts: (A) stainless steel, (C) Al_2O_3, (E) Ni, (G) SiC, and (I) YSZ. Right incubated at 300 °C for 10 h, except Ni, only 1 h: (B) stainless steel, (D) Al_2O_3, (F) Ni, (H) SiC, and (J) YSZ

SEM micrograph of an incubated Al_2O_3 fiber (Figure 6.4, top) reveals that after incubation macrovoids are still present in the Al_2O_3 fiber, whereas these have disappeared for the other materials, e.g., stainless steel (Figure 6.4, bottom).

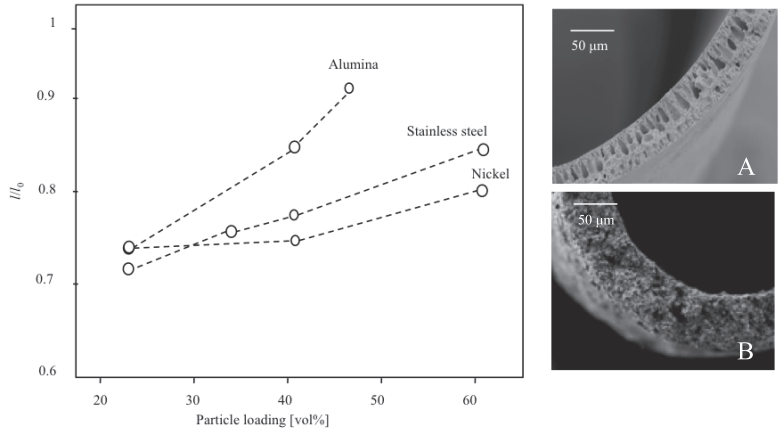

Figure 6.4: Normalized fiber length (l/l_o) after incubation at 300 °C for 10 h as function of the particle concentration. SEM images of incubated hollow fibers: (A) 58 vol.% Al_2O_3 and (B) 58 vol.% SS

At a particle loading of 60% the length of the two metal containing fibers reduces by approximately 20% upon incubation, and almost no reduction in length is observed for the Al_2O_3 fiber.

The shrinkage due to viscous deformation is driven by a reduction in the surface free energy associated with the macrovoids. It is to be expected that the rate of the macrovoid decay will be influenced by the size and shape of the macrovoids. The differences in dimensional changes in Figure 6.4 can be qualitatively rationalized by considering the characteristic time for viscous sintering at constant temperature [14]:

$$t_c = \lambda\eta/\sigma \qquad (6.1)$$

where σ is the surface tension, η is the viscosity, and λ is the characteristic length. The characteristic length is associated with the size and shape of the macrovoids.

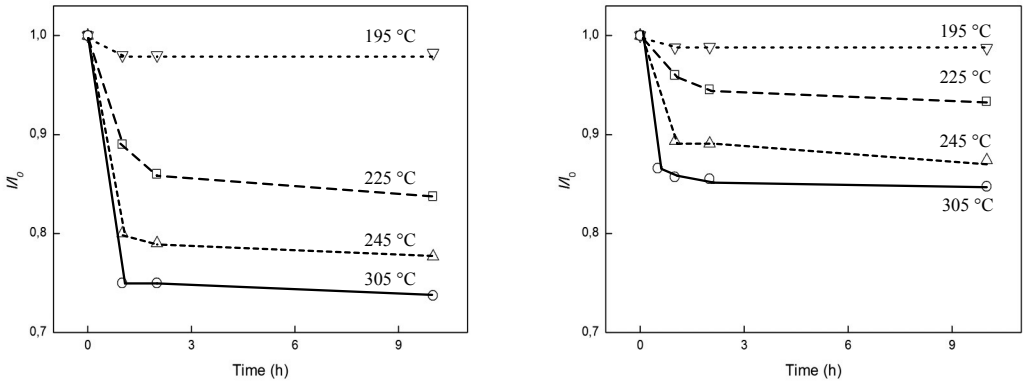

Figure 6.5: Normalized fiber length (l/l_0) as function of time at different temperatures, for 33 vol% Al_2O_3 (left) and 41 vol% Al_2O_3 (right)

The significance of λ is illustrated in Figure 6.5, where the normalized length of Al_2O_3 containing fibers (Figure 6.5 left: 23 vol.%, Figure 6.5 right: 41 vol.%.) is plotted as function of the time during incubation at a specific temperature. For all temperatures, the reduction in length for both fibers occurs in the first hours and the extent of shrinkage reaches an asymptotic value after a few hours. This asymptotic value corresponds to the maximum size of macrovoids that can be removed; the characteristic time for larger macrovoids is too long and these larger macrovoids will persist. At higher temperatures the viscosity of the particle-loaded polymer reduces and the asymptotic value of the normalized fiber length l/l_0 is lower, indicating that the size of the macrovoids that can disappear via viscous deformation is larger. Comparing the different concentrations of Al_2O_3 shows that at the same temperature a higher particle concentration corresponds to a higher viscosity, and hence a lower extent of macrovoid removal.

In Figure 6.6 the relation between the dynamic viscosity and particle loading is depicted for stainless steel and Al_2O_3 loaded polymers at 270 °C. Below a particle concentration of ~20 vol% the viscosity increases moderately with particle loading and no pronounced effect of the nature of the particles can be distinguished. Above 20 vol% the viscosity of the polymer containing stainless steel increases with an increasing slope.

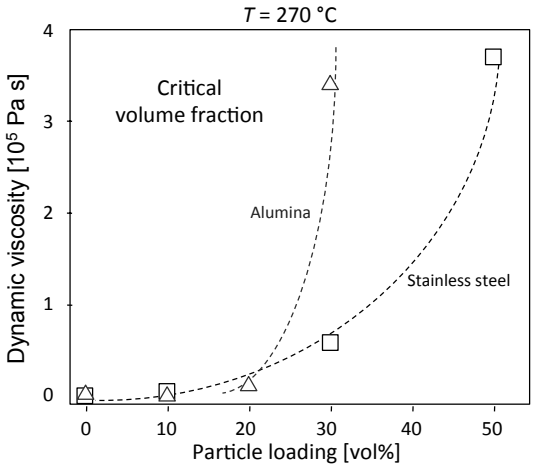

Figure 6.6: Dynamic viscosity (T = 270 °C) as function of the Al_2O_3 and stainless steel particle loading

A very strong variation in viscosity with particle concentration is observed when the particle concentration exceeds ~50 vol%. For the polymer containing Al_2O_3 particles the viscosity changes far more abruptly; a very sharp increase in viscosity is observed directly in the concentration range 20 - 30 vol%. The sharp increase can be associated with a critical particle concentration ϕ_c, above which the viscosity changes rapidly to a very high value that does now allow viscous deformation.

The value of ϕ_c is dependent on the size, shape, and type of the particles and can be obtained from independent rheology studies of the particle-loaded polymer[15], above the glass transition temperature of the polymer. It is a direct indication of the maximum particle loading below which extensive fiber shrinkage can be expected. For the stainless steel and nickel powders ϕ_c is relatively high. In contrast, for the Al_2O_3 powder ϕ_c is relatively low and viscous deformation will only occur at concentrations below ~30 vol%. The SEM micrographs in Figure 6.3 indicate that 23 vol% of YSZ particles already exceeds the ϕ_c of this powder.

In Figure 6.7 the permeability (multiplied with R and T) of a selection of Al_2O_3 and stainless steel fibers is presented as a function of the average pressure, $0.5\times(p_{feed}+p_{permeate})$. The fibers can withstand the maximum trans-membrane pressure difference allowed by the experimental set-up (2 MPa), indicating that their mechanical properties are sufficient for a variety of membrane applications. A more detailed comparison of the mechanical properties is complicated by, amongst others, differences in Weibull modulus and ductility between the ceramics and metals fibers, and is considered beyond the scope of this study.

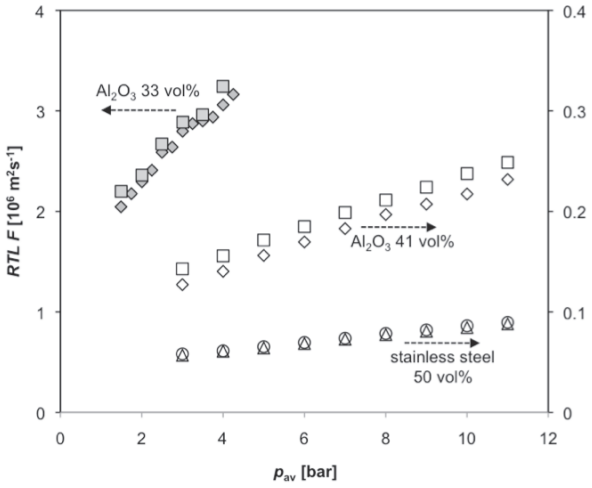

Figure 6.7: Single-gas dead-end nitrogen permeability multiplied with R and T ($RTLF$), at 20 °C, as a function of average pressure, for Al_2O_3 (33 vol%), Al_2O_3 (41 vol%), and stainless steel (50 vol%), in duplo

For all fibers a linear relation between permeability and average pressure is observed, representative of mass transport by combined viscous flow and Knudsen diffusion. The slope of the linear relation is associated with the viscous transport mechanism, and the intercept with the y-axis corresponds to the Knudsen diffusion coefficient. For the fibers derived from Al_2O_3 (41 vol%) and stainless steel, comparison between the two contributions signifies that at highest pressures applied in this study the contributions of both transport mechanisms to the total permeability are of the same order of magnitude. For the Al_2O_3 (33 vol%) the viscous transport is dominant. Adopting the rudimentary assumption of cylindrical pores with a single

pore diameter, the intercept and slope of the lines in Figure 6.7 allow to calculate the pore diameter d_p and ratio of porosity and tortuosity ε/τ of the corresponding fiber, using [16]:

$$RTLF = \frac{\varepsilon}{\tau}\frac{d_p^2}{32\eta}p_{av} + \frac{\varepsilon}{\tau}\frac{d_p}{3}\sqrt{\frac{8RT}{\pi M}} \qquad (6.2)$$

In this equation R is the gas constant [J mol^{-1} K^{-1}], T the temperature [K], L is the wall thickness of the fiber wall multiplied with a geometrical factor G to account for curvature of the fiber wall, F the permeance [mol m^{-2}s^{-1}Pa^{-1}], η the viscosity of the gas [Pa s], and p_{av} the average pressure [Pa]. The geometrical factor is $G = a/\ln(1+a)$, where $a = \delta/r$ is the ratio of δ and the inner fiber radius r [17].

For the stainless steel fiber the linear trend between permeability and average pressure yields d_p = 89 nm and ε/τ = 0.002 (F = 6.1 10^{-8} and 6.1 10^{-8} mol m^{-2} s^{-1} Pa^{-1}, at p_{av} = 4 bar, T = 293 K and L = 0.07 mm for two membranes). The ratio of porosity and tortuousity is unrealistically small, suggesting that the assumption of cylindrical pores is not justified for this fiber. Considering only the viscous flow contribution, an estimate of the porosity can be obtained from the Blake-Kozeny equation [18]:

$$RTLF = -\frac{\varepsilon^3}{(1-\varepsilon)^2}\frac{D_p^2}{72\eta}p_{av} \qquad (6.3)$$

in which D_P is the diameter of the particles. This crude approach yields a value of ε = 0.40, which is in reasonable agreement with mercury intrusion measurements (ε = 0.37). Elemental analysis of the stainless steel fibers indicates that after sintering a large amount of carbon residue (13 wt% of the initial polymer) still persists in the fibers, possibly leading to a reduced pore diameter. In addition to a reduced pore size, the presence of too much carbon also has negative implications on the corrosion resistance of the fibers. During heat treatment the presence of carbon results in the transformation of chromium oxide into chromium carbide, hampering the formation of a passive film of chromium oxide for corrosion protection [19]. Appropriate strategies should be devised to achieve fibers with less carbon, sensible approaches will involve selection of a different polymer, the optimization of the polymer burn–out, and sintering strategies involving

sequential combinations of oxidative and inert gaseous environments.

For Ni fibers sintered at 800 °C no apparent relation between permeability and average pressure has been observed and the repeatability of the experiments is very poor; the standard deviation for 5 fibers is larger than the average value (data not shown). The SEM micrographs of the Ni fibers in Figure 6.8 reveal a densified structure. Further optimization of sintering strategies could be devised to prepare Ni fibers with an appropriate morphology. As the aim of this study is to demonstrate the generic nature of our approach to attain small radial dimensions of fibers, optimization of the sintering strategies is considered a topic of future study.

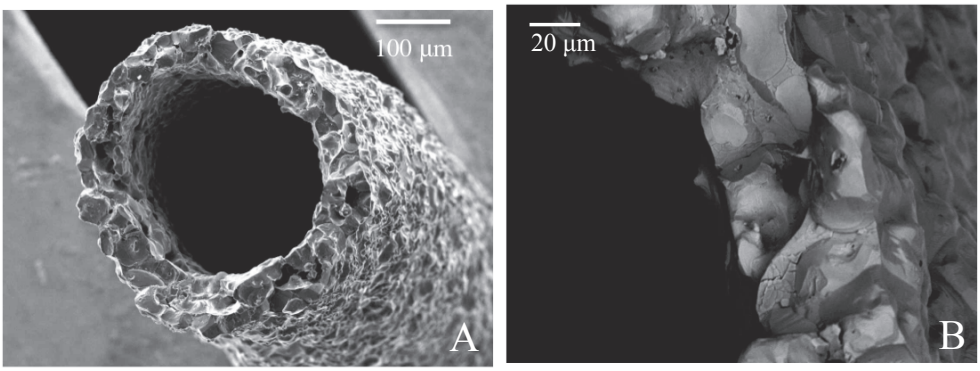

Figure 6.8: SEM image of a Ni fiber sintered at 800°C, cross section at different magnifications

For the Al_2O_3 (41 vol%) applying equation 6.2 to the permeation data in Figure 6.7 results in d_p = 140 nm and ε/τ = 0.006 (F = 1.9 10^{-7} and 1.7 10^{-7} mol m^{-2} s^{-1} Pa^{-1}, at p_{av} = 4 bar, T = 293 K, and L = 0.053 mm for two membranes). The value of d_p is in agreement with the value of the average pore diameter obtained from capillary flow porometry experiments, d_p = 120 nm. Similar permeation experiments for porous flat Al_2O_3 disks with a very well defined structure, made by colloid filtration using the same Al_2O_3 powder [20], yield a lower value of d_p = ~90 nm and higher value of ε/τ = ~0.1. These results indicate that the morphology of the Al_2O_3 (41 vol%) fiber is less regular than the flat disks obtained from colloidal filtration. Compared to the 41 vol% Al_2O_3 fiber, the 33 vol% fiber has a much higher permeability (note that the values are plotted on different y-axes). The large pore size (d_p = 260 nm) and small value of porosity (ε/τ = 0.04) are indicative of pinholes or other defects, through which viscous transport occurs (F = 3.0 10^{-6} and

3.1 10^{-6} mol m^{-2} s^{-1} Pa^{-1}, at p_{av} = 4 bar and T = 293 K, and L = 0.05 mm for two membranes). This is also apparent from a light microscope image of the fiber (Figure 9 A and B). The presence of significant defects is due to the low particle concentration in the green fiber. It even becomes difficult to obtain a sintered fiber with arbitrary length; during thermal treatment the fibers break up into pieces of <1 cm. (Figure 6.9 C-D). Despite the unfavorable presence of defects, the Al_2O_3 (33 vol%) fibers are mechanically sufficiently strong to maintain structural integrity up to 20 bars trans membrane pressure difference.

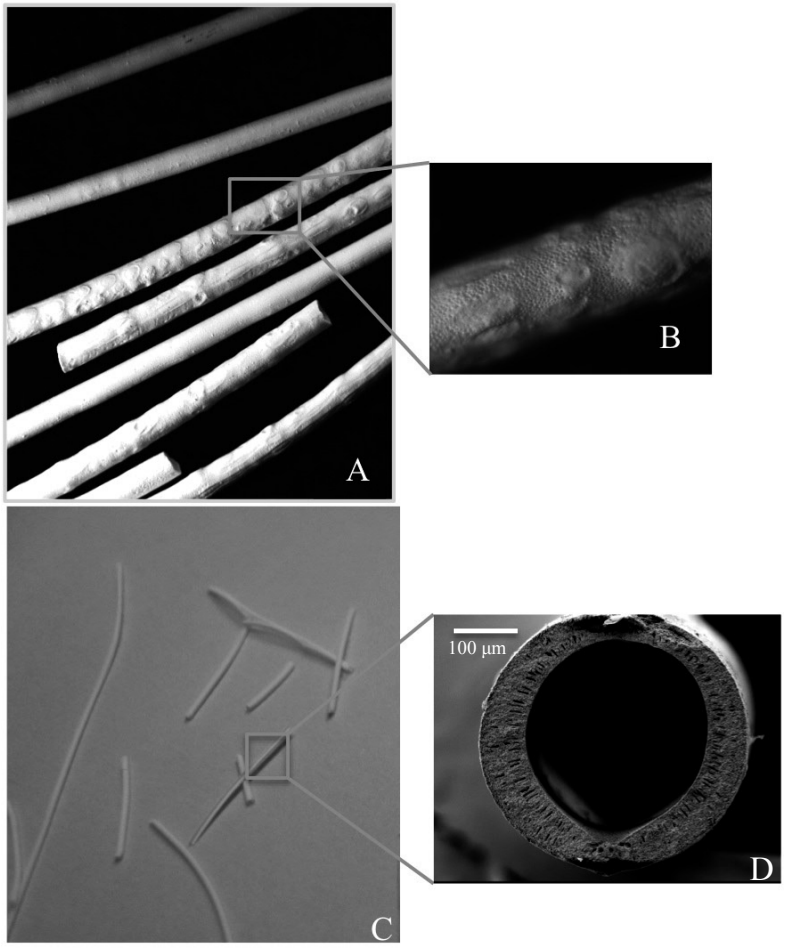

Figure 6.9: Images of Al_2O_3 fiber with 33 vol%

For thin SiC and YSZ fibers no conclusive permeance data could be obtained. For SiC the required sintering temperature could not be reached, in our experimental set-up, to obtain a strong fiber. For 23 vol% YSZ fibers thermal treatment yields fibers that are broken into pieces of ~ 1 cm. For the YSZ powder the particle loading of 23 vol% is too low to allow adequate particle adherence during the imposed thermal treatment.

The minimum amount of particles required for sufficient particle adherence, combined with the value of $\phi_{c,}$ provide boundaries to the concentration range, allowing fabrication of hollow fibers with very small diameter. A schematic representation is given in Figure 6.10 for stainless steel, Ni, and Al_2O_3, and YSZ.

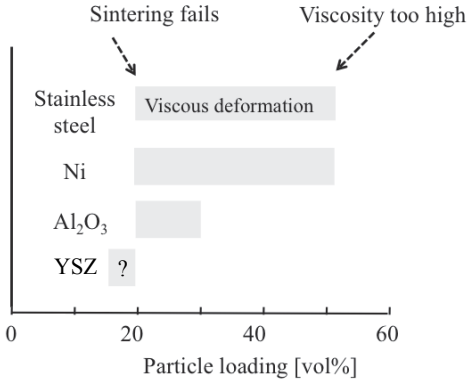

Figure 6.10: Schematic qualitative representation of the loading range allowing viscous deformation, for different inorganic powders

For the large metal powders the concentration range allowing viscous deformation is relatively large. For the small ceramic powders the range is only small. For synthesis of high quality thin YSZ fibers, this range will require broadening to obtain fibers with adequate strength. The minimum required loading can possibly be reduced by, for instance, adding sintering agents or adding particles with a broader size distribution and other particle shape. The value of ϕ_c may be increased by, for instance, selecting a different polymer.

From Figure 6.10 it can be rationalized why extensive viscous shrinkage of inorganic hollow fibers during thermal treatment has not been reported

earlier. In most studies involving inorganic hollow fibers, small inorganic particles are selected. For such powders the concentration range allowing viscous deformation will be narrow and occurs at low concentrations. Consequently, particle concentrations far exceeding the value of ϕ_c have been used, and surface energy driven viscous removal of marcrovoids will not be significant.

4 Conclusions

Stainless steel, Ni, Al_2O_3, SiC, and YSZ porous hollow fibers with regulated small radial dimensions have been prepared, by combining the well-established dry-wet spinning method for the fabrication of polymeric hollow fibers with a thermal treatment program. For sufficiently low inorganic particle concentrations, surface energy driven viscous deformation allows removal of macrovoids, resulting in fibers with exceptionally small radial dimensions. The viscous deformation process is only observed for a limited range of particle loadings. The upper limit of this range is associated with a too high viscosity of the green fiber, and can be related to a critical particle concentration, ϕ_c, obtained from rheology measurements. The lower limit is associated with an insufficient amount of particles to allow consolidation and subsequent sintering of the particles. For large metal particles, i.e., stainless steel and nickel, the viscous deformation occurs over a broad concentration range. In contrast, for small ceramic particles this concentration range is narrow and obtaining thin fibers without defects is far more challenging.

Reference

[1] S. Liu, K. Li, Preparation TiO_2/Al_2O_3 composite hollow fibre membranes, Journal of Membrane Science, 218 (2003) 269-277.

[2] L.-F. Han, Z.-l. Xu, Y. Cao, Y.-M. Wei, H.-T. Xu, Preparation, characterisation and permeation property of Al_2O_3, Al_2O_3-SiO_2 and Al_2O_3-kaloin hollow fiber membranes, Journal of Membranes Science, 372 (2011) 154-164.

[3] S. Liu, K. Li, R. Hughes, Preparation of porous aluminium oxide (Al_2O_3) hollow fibre membranes by a combined phase-inversion and sintering method, Ceramics International, 29 (2003) 875-881.

[4] X. Tan, S. Liu, K. Li, Preparation and characterization of inorganic hollow fiber membranes, Journal of Membrane Science, 188 (2001) 87-95.

[5] B. Kingsbury, K. Li, A morphological study of ceramic hollow fibre membranes, Journal of Membrane Science, 328 (2009) 134-140.

[6] N. Yang, X. Tan, Z. Ma, A phase inversion/sintering process to fabricate nickel/yttria-stabilized zirconia hollow fibers as the anode support for micro-tubular solid oxide fuel cells, Journal of Power Sources, 183 (2008) 14-19.

[7] C. Buysse, A. Kovalevsky, F. Snijkers, A. Beukenhoudt, S. Mullens, J. Luyten, J. Kretzschmar, S. Lenaerts, Development, performance and stability of sulfur-free, macrovoid-free BSCF capillaries for high temperature oxygen separation from air, Journal of Membrane Science, 372 (2011) 239-248.

[8] N. Liu, X. Tan, B. Meng, S. Liu, Honeycomb-structured perovskite hollow fiber membranes with ultra-thin densified layer for oxygen separation, Separation and Purification Technology, 80 (2011) 396-401.

[9] Z. Wang, H. Liu, X. Tan, Y. Jin, S. Liu, Improvement of the oxygen permeation through perovskite hollow fibre membranes by surface acid-modification, Journal of Membrane Science, 345 (2009) 65-73.

[10] S.-M. Lee, I.-H. Choi, S.-W. Myung, J.-y. Park, I.-C. Kim, W.-N. Kim, K.-H. Lee, Preparation and characterization of nickel hollow fiber membrane, Desalination, 233 (2008) 32-39.

[11] B. Meng, X. Tan, X. Meng, S. Qiao, S. Liu, Porous and dense Ni hollow fibre membranes, Journal of Alloys and Compounds, 470 (2009) 461-464.

[12] F. Dal Grande, A. Thursfield, K. Kanawka, N. Droushiotis, U. Doraswami, Microstructure and performance of novel Ni anode for hollow fibre solid oxide fuel cells, Solid State Ionics, 180 (2009) 800-804.

[13] X. Tan, K. Li, Inorganic hollow fibre membranes in catalytic processing, Current Opinion in Chemical Engineering, 1 (2011) 69–76.

[14] H.K. Kuiken, Viscous sintering : the surface-tension-driven flow of a liquid form under the influence of curvature gradients at its surface Journal of Fluid Mechanics, 214 (1990) 503-515.

[15] T. Hanemann, Influence of particle properties on the viscosity of polymer-alumina composites, Ceramics International, 34 (2008) 2099-2105.

[16] A.J. Burggraaf, L. Cot, Fundamentals of inorganic membrane science and technology, Elsevier Science BV, 1996.

[17] T. Zivkovic, Thin supported silica membranes, Ph.D. thesis, University of Twente, Netherlands, 2007.

[18] R.B. Bird, W.E. Stewart, E.N. Lightfoot, Transport phenomena, first ed., John Wiley & Sons, Inc., Madison, 1960.

[19] C.T. Too, Sensitisation of austenitic stainless steels, Cambridge, 2002.

[20] N.E. Benes, Mass transport in thin supported silica membranes, Ph.D. thesis, University of Twente, Netherlands, 2000.

Chapter 7
Conclusions and perspectives

7.1 Conclusions

In this thesis a generic method is presented for preparation of porous inorganic hollow fibers, with diameter tunable down to ~ 250 μm. A selection of representative hollow fibers is depicted in Figure 7.1. The variation in diameter of the fibers in Figure 7.1 (~250 – 750 μm) is achieved using a single spinneret with fixed dimensions. The only difference in the preparation of the fibers is the type and loading of the added inorganic particles.

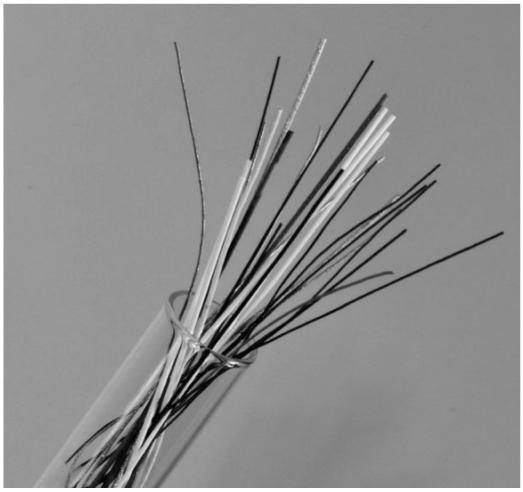

Figure 7.1: Test tube with a variety of stainless steel, alumina, nickel, yttrium stabilized zirconia, and silicon carbide hollow fibers

The generic strategy for fiber preparation is depicted in Figure 7.2 and is considered to consist of four different steps.

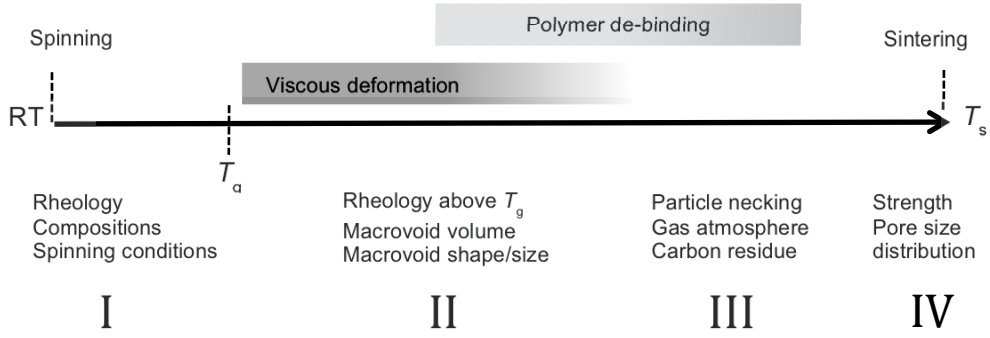

Figure 7.2: Schematic representation of the generic preparation of inorganic hollow fibers

Step I is the dry-wet spinning process in which a particle loaded polymer solution is pressed through a spinneret and coagulated in a non-solvent bath. The morphology of the obtained fiber, a sponge-like structure combined with macrovoids, depends largely on the composition and physicochemical properties of the spinning mixture, and the applied spinning conditions. In Chapter 4 we have demonstrated that the rheology of the spinning mixture is affected by the addition of inorganic particles; the viscosity of the mixture increases with increasing particle loading.

Addition of particles also affects thermodynamics; at higher particle loadings phase separation requires less non-solvent. The rheology and thermodynamics dictate the cross-sectional morphology of the fiber. This allows tuning the fibers morphology during spinning. For example, the fiber in Figure 7.3 has a sponge-like structure at the outside, and a high porosity (macrovoids) on the inner side. This morphology implies low resistance and low surface roughness, and is beneficial for subsequent coating of additional layers.

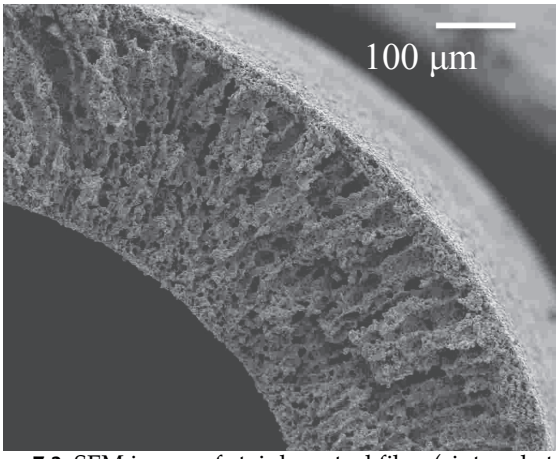

Figure 7.3: SEM image of stainless steel fiber (sintered at 1100°C)

Step II reveals a phenomenon that has not been observed previously in inorganic hollow fiber processing. Above its glass transition temperature (T_g) the polymer changes from a glassy to a rubbery material and the mechanical and physical properties change abruptly. The viscosity of the particle loaded polymer fiber can be sufficiently low for viscous removal of macro-voids, driven by reduction of macro-void surface area. This results in a substantial decrease in the final diameter. The smallest achievable fiber diameter is comparable to that of typical hemodialysis and hollow fiber gas separation membranes. The extent of the shrinkage depends on the type of particles added, and is more pronounced for lower particles loadings.

A particle specific maximum (critical) concentration can be identified, above which the time scale of viscous deformation is too long, and macro-voids persist during thermal treatment. This explains why pronounced viscous shrinkage was not observed previously, because the loading applied is generally above the critical particle concentration. Also the size of the macrovoids is crucial. Incubation of green fibers above the T_g proves that macrovoids with small sizes disappear at lower temperatures, whereas larger macrovoids persist up to higher temperatures. Maximum shrinkage thus requires low particle loading and a large volume of small macrovoids.

In **step III** the polymer de-binding occurs. Concurrently, connections are formed between the inorganic particles allowing sustained structural integrity. The removal of the polymer should not be completed before

sufficient connections have been formed between the inorganic particles. The polymer should also not persist at too high temperatures, in order to avoid negative effects on sintering or a too high carbon content in the final fiber.

For oxides removal of the polymer is relatively straightforward, because the thermal treatment is carried out in an oxidative environment (air). In the final sintered fibers of alumina, zirconia, and silicon carbide, no significant amount of carbon is detected. For the metal fibers (stainless steel and nickel) an oxidative environment can cause corrosion during thermal treatment. However, heat treatment in an inert environment (nitrogen) results in relatively high carbon concentrations in the final fiber. For nickel, this problem can be solved by heating in air, followed by exposure to a reducing (hydrogen in nitrogen) environment during sintering. An appropriate heating strategy is more challenging for stainless steel. This material consists of a mixture of metal elements, with chromium providing corrosion resistance. Polymer degradation products, in the form of residual carbon, can diffuse into the stainless steel and transform the chromium into chromium carbide. This is referred to as sensitization, and is detrimental for the corrosion resistance of the final fiber. Strategies for preventing sensitization include different polymer choices and intricate variation of the gaseous environment during thermal treatment, as will be discussed more elaborate in paragraph 7.2.

Step IV concerns the final consolidation of the structure by sintering. This step affects in particular the porosity, pore size, and mechanical properties of the final membrane. Sintering at too high temperatures can result in almost dense (impermeable) materials while sintering at a low temperature does not permit sufficient mechanical strength. Different mechanical properties (e.g., ductility, Weibull modulus) complicate quantitative comparison of the mechanical strength of fibers of different materials. From a membrane perspective, in chapter 6 fibers of alumina, nickel and stainless steel, have been shown sufficiently strong to withstand 20 bar trans membrane pressure difference (inside-out), which is sufficient for a large number of membrane applications.

In summary, a generic and versatile method was presented that allows for preparation of inorganic porous hollow fiber with different radial dimensions. First, stainless steel hollow fibers (outer diameter ~ 1.5 μm) were prepared with low resistance and low surface roughness resulting in a

mechanical strong fiber which is suitable for coating of a high quality (in)organic layer.

Secondly, inorganic hollow fibers with small radial dimensions were prepared of stainless steel, alumina, nickel, yttrium stabilized zirconia, and silicon carbide down to 250 μm. For the different materials a particle specific range can be identified in which viscous deformation is observed. A schematic representation is given in Figure 6.8. For large metal particles, i.e., stainless steel (~ 4 μm) and nickel (~9 μm), the viscous deformation occurs over a wide concentration range. However, for small ceramic particles (0.3-1.0 μm) this concentration range is far more limited. Options for expanding the range where viscous deformation occurs are addressed in the next paragraph.

7.2 Future perspectives

In the proposed generic route for fabrication of inorganic hollow fibers with small radial dimensions, four different steps are identified. In this thesis much emphasis has been placed on the second step, i.e., the surface energy-driven viscous reduction in macro-void volume to achieve extensive shrinkage. To obtain inorganic fibers with optimized properties (mechanical strength, pore-size distribution, morphology, and chemical composition) combined optimization of all four steps is required. Here, we discuss particular points of attention for the different fabrication steps, and identify recommendations for future research.

Step I: dry-wet spinning of green fibers

The morphology and geometry of a green fiber is primarily influenced by the spinning mixture *composition* and the spinning *conditions*. For organic hollow fiber membranes abundant knowledge is available for optimization. This knowledge can be used for the preparation of inorganic fibers, but here the aims are distinct. The geometry of the green fiber is merely a precursor for the final fiber geometry, and, more importantly, the organic constituent is to be entirely removed from the final fiber. This has a pronounced impact on sensible choices of spinning mixture composition. In particular, the aspired elimination of organic constituents allows for a less restricted choice in polymer and solvent. This opens possibilities for more environmentally benign systems, without inherently limiting the freedom

to tailor the geometry, morphology, and composition of the final fibers. Restrictions with respect to mixture choice are now related to steps II-IV in the fiber preparation. In step II particle loaded polymer rheology affects the range where viscous deformation can occur. In step III polymer burn-out should be in harmony with particle adherence to permit structural integrity, and for metals should not induce sensitization due to the presence of elemental carbon. The effects of insufficient removal of organic components during polymer burn-out can extent to step IV, where the sintering process and final fiber composition may be affected. Based on these considerations, potentially sensible choice for polymer and solvent will be addressed.

In our work polyethersulphone (PES) has been selected as polymer. This choice was principally inspired by the extensive existing experience with dry-wet spinning of PES hollow fibers, and the forgiving nature of this polymer in the spinning process [1-8]. As the deformation process allows the use of a wider range of polymers that generally result in green fibers with less well-defined morphology, the choice for PES is, in view of the above considerations, far from optimal. PES has a relatively high thermal stability and contains sulphur. In particular for metal hollow fibers this will result in persistence of carbon and sulfur in the final fibers, for instance negatively influencing the corrosion resistance. PES is also not a sensible choice with respect to environmental considerations. When burn-out of the polymer is successful sulphur is released to the atmosphere, and the use of PES requires a solvent such as N-methylpyrolidone (NMP). The European Commission has identified NMP as a reproductive toxicant in 2003. Ideally, a more benign solvent should be selected. Alternatively, phase inversion can be induced thermally (TIPS), avoiding the use of a solvent/non-solvent system [9]. One of the main advantages of TIPS is that undesirable chemicals can be avoided, for instance for certain polymers oil, e.g. nujol, can be used as solvent.

A non-exhaustive list of alternative potential polymer-solvent systems is depicted in Table 7.1

Polymer		T_g [°C)]	$T_{D,0}$ [°C]	Solvent	References
Polyethersulphone	PES	225		NMP	
Cellulose acetate	CA	67	290	Acetone, THF, DMF Dioxane, DSMO	[10-12]
Cellulose nitrate		43	192	Acetone	[13]
Polyvinyl acetate	PVAc	30	210	Water diethylether, acetone	[14]
Polyvinyl alcohol	PVA	85	220	Water	[15, 16]
Polyvinyl chloride	PVC	80	170	DMF, DMAc	[17, 18]
Polyvinylideenfluoride	PVDF	-35	350	NMP	[19, 20]
Polypropylene	PP	0	320	p-xylene, ethylbenzene, cumene chlorobenzene	[21, 22]
Polyethylene	PE	-52	380	p-xylene, ethylbenzene, cumene chlorobenzene	[21, 22]
Polystyrene	PS	100	327	NMP	
Polyphenylene oxide	PPO			NMP	[23]
Poly(methyl methacrylate)	PMMA	105	280	NMP, Chloroform/ethanol, Acetone	[23, 24]
Polyacrylonitrile	PAN	120	290	NMP	[25]
P84 polyimide ®		315	375	Acetone, NMP	[26, 27]
Matrimid 5218 polyimide ®		305		NMP, THF, Ethanol	8]
Ultem 1000 Polyetherimide	PEI	215		NMP, DMAc, DMF	[29, 30]
Bisfenol A Polycarbonate		150	380	NMP, 1,4-dioxane/DMAc	[31-34]
Poly (L-lactic)acid	PLLA	50	235	1,4-dioxane, NMP, water, ethylenechloride	[34, 35]
Poly(lactic-co-glycolic acid)	PGLA	38	250	NMP, 1,4-dioxane	[36]
Chitosan		140	220	Acetic acid (2%)	[37]

Table 7.1: List of polymers as potential alternative for PES, data for T_g and $T_{D,0}$ from [38] or from MSDS data sheets

The table contains information on the glass transition temperature and decomposition temperature of the respective polymer. This information is less relevant for preparation of organic hollow fibers, but will have important implications for step II-IV in the preparation of inorganic hollow fibers.

Step II: Viscous deformation of the green fiber.

We have demonstrated that the range of particle loading where viscous deformation can occur is limited. For large metal particles, i.e., stainless steel and nickel, the viscous deformation occurs over a broad concentration

range. For small ceramic particles this concentration range is narrow and obtaining thin fibers without defects is far more challenging. Here, broadening the concentration range where viscous deformation can occur would be beneficial. The upper limit of this range is associated with a too high viscosity of the green fiber. Using a polymer or additives resulting in a lower viscosity (above the T_g) could move the upper limit to a higher particle concentration. The lower limit is associated with an insufficient amount of particles to allow consolidation and subsequent sintering of the particles. Using another particle size distribution and/or sintering aid could also broaden the range where viscous deformation can occur.

Step III: Polymer de-binding.

In this step the polymer is to be removed from the fiber. In this step two challenges are identified, as is depicted in Figure 7.5.

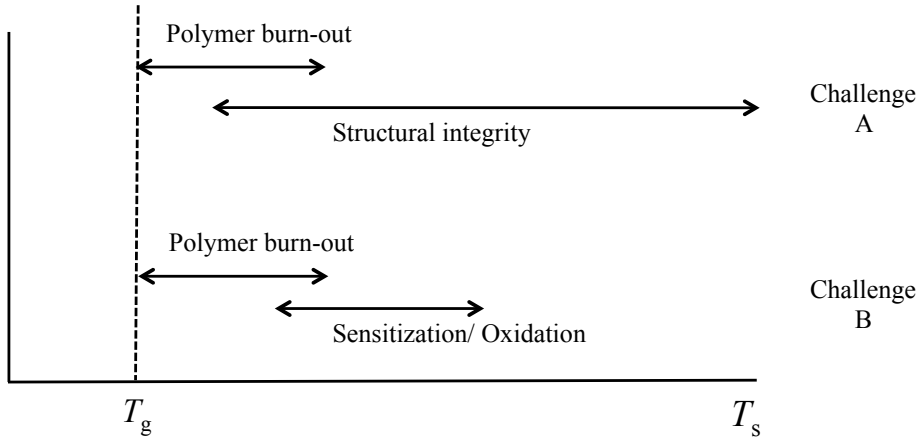

Figure 7.5: schematic drawing of challanges in step III and IV

The first challenge (A) is to maintain the structural integrity of the fiber during the de-binding. In particular for low loading of inorganic particles, burn-out of the polymer can be accompanied by insufficient adherence between the particles. This results in fibers that have fallen into pieces (Figure 7.6a), fibers with irregular structure (Figure 7.6b), or no apparent fibers at all.

A too low viscosity of the fiber, above the T_g of the polymer, can result in extensive deformation, an examples of this is depicted later on in this chapter.

To avoid this, the loading of particles can be increased. Alternatively, the rheology of the selected polymer can perhaps be altered via additives, or by mixing with another polymers.

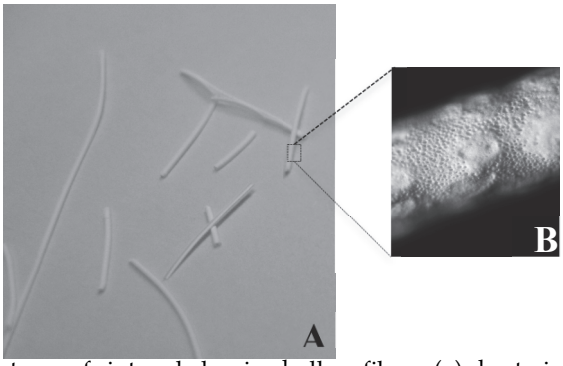

Figure 7.6: Pictures of sintered alumina hollow fibers. (a) short pieces, (b) irregular structure

The second challenge (B) is removal of binder before it can react with the inorganic particles. This is of particular importance for stainless steel fibers. To avoid oxidation of these fibers polymer burn-out can be conducted in inert or reducing atmosphere. This hampers the removal of organic material, which above a certain temperature can react with elements present in the steel. In particular the reaction between chromium and carbon to form chromium carbide will have a detrimental effect on the corrosion resistance of the final steel fibers. Stainless steel (316L) belongs to the group of austenitic stainless steel in which the corrosion resistance is enhanced by the addition of chromium; a compact, continuous, insulating and regenerative protective chromium oxide film is created on the steel surface. Formation of chromium carbide during thermal treatment, resulting precipitation of chromium-rich carbides ($M_{23}C_6$ or M_7C_3, e.g.) along the grain boundaries, reduces corrosion resistance [39].

Figure 7.7 shows that decomposition of PES and sensitization occurs in the same temperature range. One way to counteract or avoid sensitization is reducing the carbon content. This can be achieved by selecting a polymer that decomposes at a temperature below 550°C.

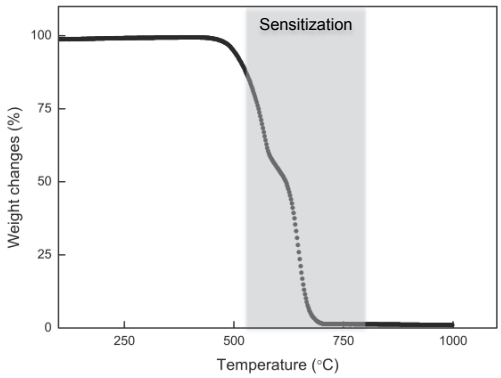

Figure 7.7: TGA graph of poly(ether)sulphone

Potential polymers can be selected from Table 7.1. A more detailed thermal evolution of different polymers is depicted in Figure 7.8. Some polymers de-bind at a discrete temperature (PMMA, PS, and PEI). A too abrupt decomposition of the polymer can have a negative effect on the morphology. Other polymers decompose in the broader temperature range (PAN, Chitosan and CA), potentially allowing for a more uniform structure.

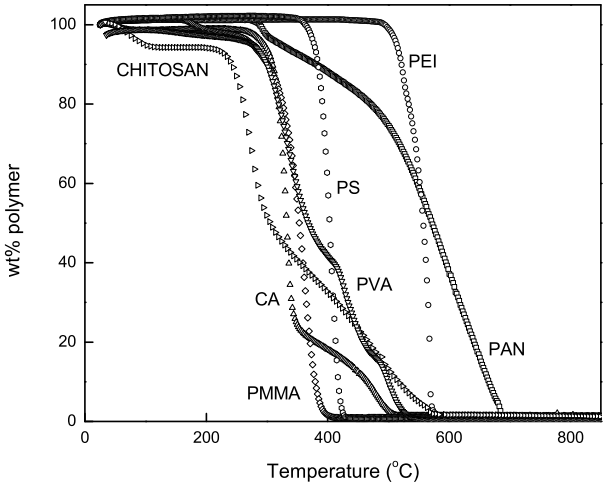

Figure 7.8:TGA graph of various polymers in air (5 K min^{-1})

For the development of high quality stainless steel hollow fibers a polymer is required that de-binds at temperatures below 550°C to avoid sensitization. Figure 7.8 shows that two polymers are appealing candidates for replacing PES: PS and PMMA. To prevent oxidation, at higher temperatures thermal treatment is performed preferably in an inert environment. Figure 7.9 displays the thermal evolution of PS and PMMA in nitrogen. The data in the figure indicate that PS can be removed completely in the inert environment. In contrast, for PMMA a significant amount of organic residue persists, even at high temperatures. For PMMA thermal treatment would require an oxidative environment, subsequently followed by a reductive environment (for instance hydrogen in nitrogen).

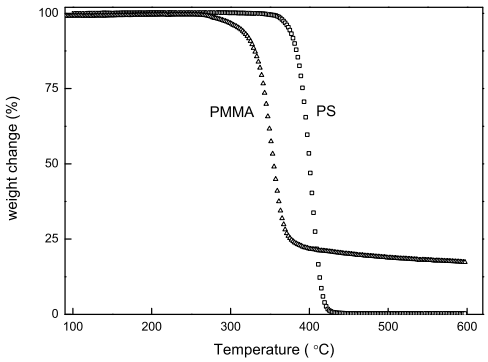

Figure 7.9: TGA graph of PS and PMMA in nitrogen (5 K min^{-1})

Preliminary experiments on fiber preparation have been conducted, using PS or PMMA as alternative to PES. In Figure 7.10 an SEM image reveals the results for PS 50 vol% derived fibers. After thermal treatment the fiber collapsed, indicating insufficient structural integrity during steps II-III.

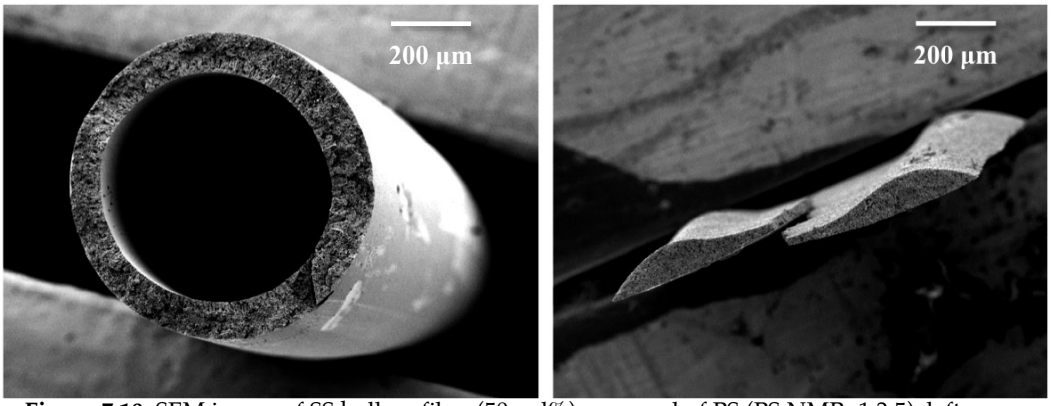

Figure 7.10: SEM image of SS hollow fiber (50 vol%) prepared of PS (PS:NMP=1:2.5); left green fiber and right sintered fiber (1100 °C)

Thin green hollow fibers, consisting of stainless steel and PMMA, were difficult to prepare (step I). In all experiments the spinneret was readily blocked. To prevent this, a small amount of PS was added to the mixture (PMMA:PS =7:1). The resulting fibers are depicted in Figure 7.10. A green fiber is displayed on the left and a sintered fiber (1100 °C) on the right. The SEM images indicate that further optimization is required to obtain round fibers after sintering.

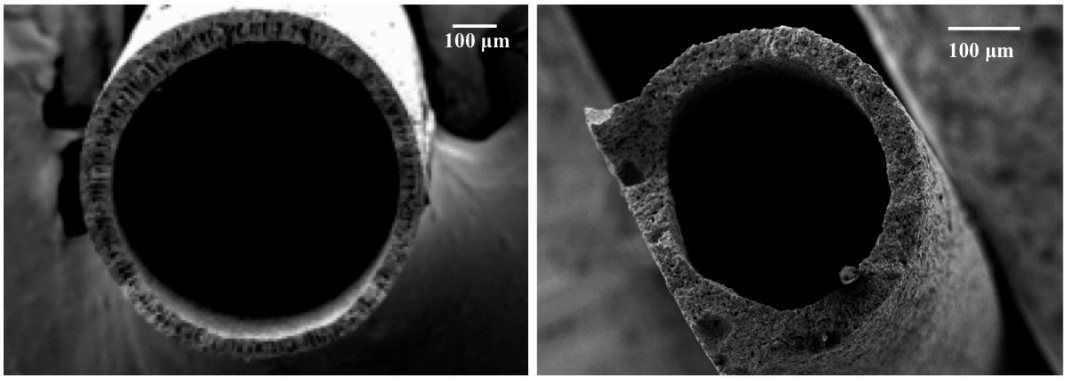

Figure 7.11: SEM image of SS hollow fiber (33 vol%) prepared of PMMA and PS, ratio 7 to 1 (PS/PMMA:NMP=1:3.7); left green fiber and right sintered fiber (1100 °C)

For the fibers prepared with PS or/and PMMA the carbon content after heat treatment is lower than the detection limit of our Elemental Analysis

set up (< 0.5 wt %). In contrast, the carbon content of fibers prepared with PES as polymer was around 14 wt%, after sintering at 1100 °C. This clearly demonstrates the potential of a suitable polymer selection for improving the corrosion resistance of stainless steel fibers.

Step IV: Sintering.

Step IV concerns the final consolidation of the structure by sintering. This step affects in particular the porosity, pore size, and mechanical properties of the final membrane. Especially for metal fibers optimization of the sintering strategy is required to improve the final structure. In Chapter 6 a SEM micrograph revealed that the current sintering strategy resulted in a densified structure of the nickel fiber. The sintering strategy can be improved via the sintering temperature, sintering time, heating- and cooling rate, and atmosphere.

7.3 Epilogue

In this thesis a strategy is presented for preparation of hollow fibers that can consist of a variety of inorganic materials, and have adjustable small radial dimensions. The distinct properties of these fibers allow for a broad application landscape. A few examples do illustrate this. The superior stability of these fibers enables their use for molecular separation in harsh environments, such as organic solvents, high temperature, or high pressure. The small dimensions of these fibers correspond to the characteristic dimensions of microfluidic devices. The facile nature of the fiber preparation method allows fabrication of highly parallelized micro-fluidic devices. Examples include micro-reactors that combine catalysis and molecular separation [40]. The porosity of the fibers corresponds to a relatively high surface area, which can benefit their use as electrode material.

In each of the above examples the demands on fiber properties are different, and specific optimization strategies are required. Although not a complete set, hopefully the tools developed in this thesis can assist such sensible optimizations.

References

[1] J. De Jong, N. Benes, G. Koops, M. Wessling, Towards single step production of multi-layer inorganic hollow fibers, Journal of Membrane Science, 239 (2004) 265-269.

[2] S. Liu, K. Li, R. Hughes, Preparation of porous aluminium oxide (Al_2O_3) hollow fibre membranes by a combined phase-inversion and sintering method, Ceramics International, 29 (2003) 875-881.

[3] N. Yang, X. Tan, Z. Ma, A phase inversion/sintering process to fabricate nickel/yttria-stabilized zirconia hollow fibers as the anode support for micro-tubular solid oxide fuel cells, Journal of Power Sources, 183 (2008) 14-19.

[4] X. tan, S. liu, K. Li, Preparation and characterisation of inorganic hollow fiber membranes, Journal of Membrane Science, 188 (2001) 7.

[5] E. Gbenedio, Z. Wu, I. Hatim, B. Kingsbury, K. Li, A multifunctional Pd/alumina hollow fibre membrane reactor for propane dehydrogenation, Catalysis Today, 156 (2010) 93-98.

[6] Z. Wang, H. Liu, X. Tan, Y. Jin, S. Liu, Improvement of the oxygen permeation through perovskite hollow fibre membranes by surface acid-modification, Journal of Membrane Science, 345 (2009) 65-73.

[7] S.-M. Lee, I.-H. Choi, S.-W. Myung, J.-y. Park, I.-C. Kim, W.-N. Kim, K.-H. Lee, Preparation and characterization of nickel hollow fiber membrane, Desalination, 233 (2008) 32-39.

[8] B. Meng, X. Tan, X. Meng, S. Qiao, S. Liu, Porous and dense Ni hollow fibre membranes, Journal of Alloys and Compounds, 470 (2009) 461-464.

[9] M. Mulder, Basic Principles of Membrane Technology, first ed., Kluwer Academic Publishers, Dordrecht, 2000.

[10] M.R. Pekny, A.R. Greenberg, V. Khare, J. Zartman, W.B. Krantz, P. Todd, Macrovoid pore formation in dry-cast cellulose acetate membranes: Buoyancy studies, Journal of Membrane Science, 205 (2002) 11-21.

[11] R.M. Boom, I.M. Wienk, T. Van Den Boomgaard, C.A. Smolders, Microstructures in phase inversion membranes. Part 2. The role of a polymeric additive, Journal of Membrane Science, 73 (1992) 277-292.

[12] C.A. Smolders, A.J. Reuvers, R.M. Boom, I.M. Wienk, Microstructures in phase-inversion membranes. Part 1. Formation of macrovoids, Journal of Membrane Science, 73 (1992) 259-275.

[13] H. Sun, S. Liu, B. Ge, L. Xing, H. Chen, Cellulose nitrate membrane formation via phase separation induced by penetration of nonsolvent from vapor phase, Journal of Membrane Science, 295 (2007) 2-10.

[14] G. Wang, Z. Tan, X. Liu, S. Chawda, J.S. Koo, V. Samuilov, M. Dudley, Conducting MWNT/poly(vinyl acetate) composite nanofibres by electrospinning, Nanotechnology, 17 (2006) 5829-5835.

[15] W.Y. Chuang, T.H. Young, W.Y. Chiu, C.Y. Lin, The effect of polymeric additives on the structure and permeability of poly(vinyl alcohol) asymmetric membranes, Polymer, 41 (2000) 5633-5641.

[16] A. Łabudzińska, A. Ziabicki, Effect of composition and gelation conditions on structural changes accompanying the gelation of PAN, PVA and gelatin solutions, Kolloid-Zeitschrift & Zeitschrift für Polymere, 243 (1971) 21-27.

[17] Q. Alsalhy, S. Algebory, G.M. Alwan, S. Simone, A. Figoli, E. Drioli, Hollow fiber ultrafiltration membranes from poly(vinyl chloride): Preparation, morphologies, and properties, Separation Science and Technology, 46 (2011) 2199-2210.

[18] M. Khayet, M.C. García-Payo, F.A. Qusay, M.A. Zubaidy, Structural and performance studies of poly(vinyl chloride) hollow fiber membranes prepared at different air gap lengths, Journal of Membrane Science, 330 (2009) 30-39.

[19] P. Sukitpaneenit, T.S. Chung, Molecular elucidation of morphology and mechanical properties of PVDF hollow fiber membranes from aspects of phase inversion, crystallization and rheology, Journal of Membrane Science, 340 (2009) 192-205.

[20] P. Sukitpaneenit, T.S. Chung, PVDF hollow fiber membrane formation: Fundamental study on the roles of phase inversion, crystallization and rheology on morphology and mechanical properties, in, 2009.

[21] K.F. Drain, W.R. Murphy, M.S. Otterburn, Solvents for polypropylene: Their selection for a recycling process, Conservation and Recycling, 6 (1983) 107-122.

[22] D.A. Blackadder, G.J. Le Poidevin, Dissolution of polypropylene in organic solvents: 4. Nature of the solvent, Polymer, 19 (1978) 483-488.

[23] J.-Y. Lai, F.-C. Lin, T.-T. Wu, D.-M. Wang, On the formation of macrovoids in PMMA membranes, Journal of Membrane Science, 155 (1999) 31-43.

[24] R. Stropnik, V. Kaiser, Polymeric membranes preparation by wet phase separation: Mechanisms and elementary processes, Desalination, 145 (2002) 1-10.

[25] I.-C. Kim, H.-G. Yun, K.-H. Lee, Preparation of asymmetric polyacrylonitrile membrane with small pore size by phase inversion and post-treatment process, Journal of Membrane Science, 199 (2002) 75-84.

[26] J. Ren, Z. Li, R. Wang, Effects of the thermodynamics and rheology of BTDA-TDI/MDI co-polyimide (P84) dope solutions on the performance and morphology of hollow fiber UF membranes, Journal of Membrane Science, 309 (2008) 196-208.

[27] S.-H. Choi, J.C. Jansen, F. Tasselli, G. Barbieri, E. Drioli, In-line formation of chemically cross-linked P84® co-polyimide hollow fibre membranes for H2/CO2 separation, Separation and Purification Technology, 76 (2010) 132-139.

[28] D.T. Clausi, W.J. Koros, Formation of defect-free polyimide hollow fiber membranes for gas separations, Journal of Membrane Science, 167 (2000) 79-89.

[29] D. Wang, K. Li, W.K. Teo, Phase Separation in Polyetherimide/Solvent/Nonsolvent Systems and Membrane Formation, Journal of Applied Polymer Science, 71 (1999) 1789-1796.

[30] K. Kneifel, K.V. Peinemann, Preparation of hollow fiber membranes from polyetherimide for gas separation, Journal of Membrane Science, 65 (1992) 295-307.

[31] M. Bodzek, J. Bohdziewicz, Porous polycarbonate phase-inversion membranes, Journal of Membrane Science, 60 (1991) 25-40.

[32] M. Di Luccio, R. Nobrega, C.P. Borges, Microporous anisotropic phase inversion membranes from bisphenol-A polycarbonate: study of a ternary system, Polymer, 41 (2000) 4309-4315.

[33] M. Di Luccio, R. Nobrega, C.P. Borges, Microporous anisotropic phase inversion membranes from bisphenol a polycarbonate: Effect of additives to the polymer solution, Journal of Applied Polymer Science, 86 (2002) 3085-3096.

[34] T. Tanaka, M. Ueno, Y. Watanabe, T. Kouya, M. Taniguchi, D.R. Lloyd, Poly(L-lactic acid) microfiltration membrane formation via

thermally induced phase separation with drying, Journal of Chemical Engineering of Japan, 44 (2011) 467-475.
[35] H.C. Liu, I.C. Lee, J.H. Wang, S.H. Yang, T.H. Young, Preparation of PLLA membranes with different morphologies for culture of MG-63 Cells, Biomaterials, 25 (2004) 4047-4056.
[36] M.J. Ellis, J.B. Chaudhuri, Poly(lactic-co-glycolic acid) hollow fibre membranes for use as a tissue engineering scaffold, Biotechnology and Bioengineering, 96 (2007) 177-187.
[37] Z. Modrzejewska, W. Eckstein, Chitosan Hollow Fiber Membranes, Biopolymers, 73 (2004) 61-68.
[38] K.t.N. D.W. van Krevelen, Properties of polymers, 4th ed., Elsevier, 2009.
[39] C.T. Too, Sensitisation of austenitic stainless steels, Cambridge, 2002.
[40] H.C. Aran, S. Pacheco, M. Luiten-Olieman, S. Er, M. Wessling, L. Lefferts, N.E. Benes, R.G.H. Lammertink, Carbon nanofibers in catalitic membrane microreactores, Journal of Membrane Science, 381 (2011) 7.

Summary

The objectives of this thesis are twofold. The first aim is to develop of robust coating procedures for thin supported films onto porous ceramic supports. The second aim is the development of a preparation methodology for high quality porous inorganic membranes, with large membrane surface area.

Chapter 1 gives a general introduction to these topics. Particular focus is on the preparation of inorganic hollow fibers, via the well-established dry-wet spinning preparation method for polymer hollow fiber membranes.

In **Chapter 2** a robust method is presented for applying a high quality micro-porous silica top layer on a commercial tubular support. The coating method is straightforward and allows for a reproducible coating of large surface area high performance silica membranes. The performance of these membranes is reproducible and is comparable to that of the low surface area flat plate membranes and short tubular membranes. No significant changes in permeance or permselectivity have been seen over a period of more than 2100 h at temperatures below 400 °C.

In **Chapter 3** a high quality solvent resistant nanofiltration membrane is developed by dipcoating a thin polydimethylsiloxane (PDMS) top layer on an alumina capillary support. The stability of the inorganic support is combined with the excellent separation properties of the PDMS toplayer. The membranes display a toluene permeance of 1.6 L $m^{-2}h^{-1}bar^{-1}$ combined with a MWCO of 500 Da and show a stable performance for at least 40 h in toluene.

To improve the surface-to-volume ratio and enhance the mechanical stability, in **Chapter 4** hollow fibers of stainless steel have been developed via a dry wet-spinning process. The morphology of the fibers is predominantly determined during the dry-wet spinning process and can be tuned by changing the spinning conditions and the composition of the spinning mixture. In analogy to their ceramic counterpart the morphology is preserved upon sintering, apart from shrinkage due to densification. The fibers combine a high strength, with a large nitrogen permeance.

In **Chapter 5 t**he surface-to-volume ratio is further increased by the development of hollow fibers with exceptionally small radial dimensions. Viscous deformation of the green fibers allows for regulated reduction of

the macro void volume resulting in a substantial reduction of the outer diameter. Depending on the particle loading different outer diameters (250 – 750 μm) can be achieved, using only a single spinneret with fixed dimensions.

In **Chapter 6** fibers of other materials were prepared, demonstrating that the method presented in chapter 5 is generic and versatile. It allows for the preparation of a variety of inorganic membranes with small radial dimensions. At low particle concentration, extensive shrinkage of hollow fibers can be achieved above the T_g of the polymer, irrespective of the type and nature of the particles added. Increasing the particle loading results in differences in shrinkage behavior for different powders. A particle specific concentration range can be identified in which extensive shrinkage is observed and fibers with adequate structural integrity are obtained.

The last chapter, **Chapter 7**, conclusions and outlook, summarizes the results obtained in the previous chapters and provides ideas for future research.

Samenvatting

De doelstelling van dit proefschrift is tweeledig. Als eerste de ontwikkeling van een coating procedure voor dunne films op poreuze keramische dragers. De tweede doelstelling is de ontwikkeling van een bereidingsmethodologie voor hoge kwaliteit poreuze anorganische membranen met grote oppervlakten.

Hoofdstuk 1 geeft een algemene inleiding in deze onderwerpen. Speciale aandacht is gegeven aan de beschrijving van de bereiding van anorganische holle vezels, via de gevestigde dry-wet spinning methode voor polymere holle vezel membranen.

In **Hoofdstuk 2** wordt een robuuste methode gepresenteerd voor het aanbrengen van een hoge kwaliteit micro-poreuze silica toplaag op een commerciële buisvormige drager. De coating methode is eenvoudig en geeft reproduceerbare coatings op grote oppervlakten wat resulteert in silica membranen met hoge selectiviteit voor verschillende gassen. De prestaties van deze membranen zijn reproduceerbaar en vergelijkbaar met die van vlakke, plaatvormige, membranen (kleine oppervlakten) en korte buisvormige membranen. Geen significante veranderingen in flux of permselectiviteit zijn waargenomen gedurende een periode van meer dan 2100 uur bij temperaturen tot 400 ° C.

In **Hoofdstuk 3** is de ontwikkeling beschreven van een nanofiltratie membraan, bestaande uit een alumina drager met een polydimethylsiloxaan (PDMS) toplaag, welke bestand is tegen verschillende organische oplosmiddelen. De dunne PDMS toplaag wordt door middel van dipcoating aangebracht op een capillaire alumina drager. De stabiliteit van de anorganische drager is gecombineerd met de uitstekende scheidende eigenschappen van de PDMS toplaag. De membranen vertonen een tolueen flux van 1,6 L m^{-2} h^{-1} bar^{-1} in combinatie met een “Molecular Weight Cut-Off” (MWCO) van 500 Da. Voor ten minste 40 uur is een stabiele tolueen flux gemeten door het membraan.

Een roestvast stalen (RVS) holle vezel membraan is ontwikkeld via de dry-wet spinproces om op deze manier een membraan systeem te verkrijgen met een verbeterde oppervlakte-volume verhouding en goede mechanische stabiliteit. Dit staat beschreven in **Hoofdstuk 4**. De morfologie van de vezels wordt voornamelijk bepaald tijdens het dry-wet spinproces

en kan worden afgestemd door het veranderen van de omstandigheden tijdens het spinproces en/of een andere keuze te maken van de samenstelling van het spinmengsel. Net als bij keramische vezels blijft de structuur behouden tijdens sinteren, met uitzondering van krimp als gevolg van verdichting van het materiaal. De RVS vezels combineren een hoge sterkte met een grote stikstof flux.

In **Hoofdstuk 5** wordt de oppervlakte-volume verhouding verder vergroot door de ontwikkeling van metallische holle vezels met uitzonderlijk kleine radiale afmetingen. Gecontroleerde afname van het volume van grote macrovoids (ruimtes), die zich in de wand van de vezel bevinden, resulteert in een substantiële verkleining van de buitendiameter. Deze afname in volume van de macrovoids wordt veroorzaakt door veranderingen in de viscositeit. Met één opstelling kunnen vezels gemaakt worden met verschillende buitendiameters (250 tot 750 micrometer). Deze buitendiameter is direct gerelateerd aan de hoeveelheid deeltjes dat is toegevoegd aan het spin mengsel.

Hoofdstuk 6 beschrijft de bereiding van vezels van andere materialen. Dit laat zien dat de in hoofdstuk 5 gepresenteerde methode generiek en veelzijdig is. De bereiding van een verscheidenheid aan anorganische holle vezel membranen met kleine radiale afmetingen wordt hierdoor mogelijk.

Bij een lage concentratie aan deeltjes vindt boven de glas overgangstemperatuur (T_g), van het polymeer, een sterke krimp plaats, ongeacht het soort en de aard van de deeltjes die worden toegevoegd. Het verhogen van de concentratie aan deeltjes, resulteert in een ander krimpgedrag van de vezels. Een te lage hoeveelheid deeltjes resulteert in beperkte sterkte van de vezels. Voor elk materiaal kan bepaald worden in welk concentratie gebied de extra krimp plaatsvindt en waarin de vezels voldoende sterk zijn

In het laatste hoofdstuk, **Hoofdstuk 7**, worden de belangrijkste conclusies van dit proefschrift samengevat en worden ideeën beschreven voor toekomstig onderzoek.

Acknowledgements

I want to thank anyone who contributed to the realization of this thesis, by giving input, comments, and support. It is highly appreciated!!

Some people I want to mention by name. First of all, I want to thank my professor Arian Nijmeijer, he encouraged me to start this PhD research. He was also part of the STW project in which we both worked to develop membranes. Another special thanks I want to give to my supervisor Nieck Benes for his support, encouragement and for teaching me how to plan and construct papers and presentations.

For more than ten years I have worked as a research assistant in the University of Twente. In this period, I worked under the guidance of three professors; besides Arian Nijmeijer, I want thank Dave Blank for the opportunities he gave me to improve my skills and Matthias Wessling for his support and enthusiasm for the preparation of inorganic hollow fibers.

Performing research is a great teamwork and I would like to thank Szymon Dutczak for the interesting conversations about polymers, and the enthusiastic students Michiel Raaijmakers, Nadia Vleugels, and Ferdi Jansen for their part in this research. A very special thanks to my STW project partners, Petrus Cuperus (Solsep), Marcel den Exter (ECN), Gerrald Bargeman (AkzoNobel), Kees de Ruijter (Wyatt Tech), Erik Hoving (DSM), Monique Wiegel (STW), Arian Nijmeijer (Shell), Louis Winnubst (UT), and Dimitrios Stamatialis (UT) for the pleasant cooperation.

I would like to thank Henk Kruidhof for sharing his membrane expertise and for giving me the opportunity to give an oral presentation at an international conference, ICIM, as a research assistant in 2005. There I became aware that performing research is a challenging and fantastic job to do.

Also I want to thank my colleagues Cindy and Frank for the practical support and daily update of the football competition, and ex-colleagues Natasha, Wika, Herman, Attila, and Gerrit for the good time we had in the lab (I'll never forget the pancakes). Also thanks to the members of IM- and the MTG-group, the mix between organic and inorganic made my working life much more diverse and interesting!

Last but not least, I want to thank my husband, Henk-Jaap, for his continuous support and encouragement. Without you, my dearest, I never could have done this. In the eighteen years we know each other, your love and confidence in me has given me the power to change from a wallflower to who I am now. Thanks for everything you gave to me!